REPORT DOCUMENTATION PAGE

2

Form Approved OMB NO. 0704-0188

1. REPORT DATE (DD-MM-YYYY)	2. REPORT TYPE	3. DATES COVERED (From - To)
29-08-2014	Ph.D. Dissertation	-

4. TITLE AND SUBTITLE
High order numerical simulationof waves using regular gridsand non-conforming interfaces

5a. CONTRACT NUMBER
W911NF-11-1-0384

5b. GRANT NUMBER

5c. PROGRAM ELEMENT NUMBER
611102

6. AUTHORS
Michael Medvinsky

5d. PROJECT NUMBER

5e. TASK NUMBER

5f. WORK UNIT NUMBER

7. PERFORMING ORGANIZATION NAMES AND ADDRESSES
North Carolina State University
2701 Sullivan Drive
Suite 240, Campus Bx 7514
Raleigh, NC 27695 -7003

8. PERFORMING ORGANIZATION REPORT NUMBER

9. SPONSORING/MONITORING AGENCY NAME(S) AND ADDRESS (ES)
U.S. Army Research Office
P.O. Box 12211
Research Triangle Park, NC 27709-2211

10. SPONSOR/MONITOR'S ACRONYM(S)
ARO

11. SPONSOR/MONITOR'S REPORT NUMBER(S)
59637-MA.19

12. DISTRIBUTION AVAILIBILITY STATEMENT
Approved for public release; distribution is unlimited.

13. SUPPLEMENTARY NOTES
The views, opinions and/or findings contained in this report are those of the author(s) and should not contrued as an official Department of the Army position, policy or decision, unless so designated by other documentation.

14. ABSTRACT
We study the propagation of waves over large regions of space with smooth, but not necessarily constant, material characteristics, separated into sub-domains by interfaces of arbitrary shape. We consider a divide and conquer approach based on wave splitting into incoming and outgoing waves. We assemble the overall solution from the set of individual solutions to an auxiliary problem (AP). The AP is defined independently for each sub-domain. The choice of the AP is relatively flexible; it can be formulated to enable an easy and economical numerical solution. Our new method uses only simple structured grids, e.g., Cartesian or polar, regardless of the shape of the

15. SUBJECT TERMS
Difference potentials, boundary projections, Calderon's operators, regular grids, curvilinear boundaries, variable coefficients, compact differencing, high order accuracy.

16. SECURITY CLASSIFICATION OF:			17. LIMITATION OF ABSTRACT	15. NUMBER OF PAGES	19a. NAME OF RESPONSIBLE PERSON
a. REPORT	b. ABSTRACT	c. THIS PAGE			Semyon Tsynkov
UU	UU	UU	UU		19b. TELEPHONE NUMBER 919-515-1877

Report Title

High order numerical simulationof waves using regular gridsand non-conforming interfaces

ABSTRACT

We study the propagation of waves over large regions of space with smooth, but not necessarily constant, material characteristics, separated into sub-domains by interfaces of arbitrary shape. We consider a divide and conquer approach based on wave splitting into incoming and outgoing waves. We assemble the overall solution from the set of individual solutions to an auxiliary problem (AP). The AP is defined independently for each sub-domain. The choice of the AP is relatively flexible; it can be formulated to enable an easy and economical numerical solution. Our new method uses only simple structured grids, e.g., Cartesian or polar, regardless of the shape of the boundaries or interfaces. In the regions of smoothness, it employs high
order accurate finite difference schemes on compact stencils. They do not require any additional boundary conditions besides those needed for the underlying differential equation itself. Interfaces not aligned with the grid handled by Calderon's operators and the method of difference potentials.

The method of difference potentials offers a number of important benegits for computation. It easily handles curvilinear boundaries, variable coe♬ffcients and general boundary conditions while the complexity remains close to that of a finite difference scheme on a regular structured grid. The main advantage is that this
methodology provides high order accuracy and overcomes the di♬culties inherent in more traditional approaches.

Tel Aviv University

The Raymond and Beverly Sackler Faculty of Exact Sciences

School of Mathematical Sciences

Department of Applied Mathematics

High order numerical simulation of waves using regular grids and non-conforming interfaces

Thesis submitted for the degree "Doctor Of Philosophy"

by

Michael Medvinsky

Submitted to the Senate of Tel Aviv University

October 6, 2013

This work was carried out under supervision of

Professor Eli Turkel, Tel-Aviv University

and

Professor Semyon Tsynkov, North-Carolina State University

To My Kids

I would like to express my gratitude and deepest appreciation to Professor Eli Turkel for his patience, constant involvement and great support during this work and during last seven years of acquaintance and cooperation.

I am also thankful to Professor Semyon Tsynkov for his guidance, counseling and for his friendship, and especially for the unforgettable internship in NCSU. Without his help and encouragement this work would never have been done.

Of course, I am grateful to my family for their patience and *love*. To my supporting parents, thoughtful wife and lovely kids. Without them this work would never have come into existence (literally).

I would like to express my gratitude to many family members and friends who were "there" during the long period of this work but wasn't named above.

This work was supported in part by the US-Israel Binational Science Foundation (BSF) under grant # 2008094. When in residence at NCSU, the work of the author was also supported by the US NSF under grant # DMS-0810963, US AFOSR under grant # FA9550-10-1-0092, and US ARO under grant # W911NF-11-1-0384.

Abstract

We study the propagation of waves over large regions of space with smooth, but not necessarily constant, material characteristics, separated into sub-domains by interfaces of arbitrary shape. We consider a divide and conquer approach based on wave splitting into incoming and outgoing waves. We assemble the overall solution from the set of individual solutions to an auxiliary problem (AP). The AP is defined independently for each sub-domain. The choice of the AP is relatively flexible; it can be formulated to enable an easy and economical numerical solution. Our new method uses only simple structured grids, e.g., Cartesian or polar, regardless of the shape of the boundaries or interfaces. In the regions of smoothness, it employs high order accurate finite difference schemes on compact stencils. They do not require any additional boundary conditions besides those needed for the underlying differential equation itself. Interfaces not aligned with the grid handled by Calderon's operators and a method of difference potentials [52].

The operator of Calderon and the method of difference potentials have a number of important advantages; it easily handles curvilinear boundaries, variable coefficients and general boundary conditions while the complexity is that of a finite-difference scheme on a regular structured grid. A main advantage is that this methodology provides high order accuracy and overcomes the difficulties inherent in more traditional approaches.

Contents

List of Algorithms

List of Figures

List of Tables

Chapter 1

Introduction

We consider problems that involve the propagation of acoustic or electromagnetic waves over large regions of space with smooth, but not necessarily constant, material characteristics, separated by interfaces of arbitrary shape. The external boundaries can also be arbitrarily shaped. These problems play a central role in imaging (medical and other types), nondestructive evaluation, land mine detection, active control of sound, etc. We describe the system governed by the Maxwell equations coupled with appropriate initial and boundary conditions. The acoustic case results in a similar situation. The Maxwell equations are given by:

$$\frac{\partial \overrightarrow{B}}{\partial t} + \nabla \times \overrightarrow{E} = 0 \quad (Faraday's\ Law),$$

$$\frac{\partial \overrightarrow{D}}{\partial t} - \nabla \times \overrightarrow{H} = -\overrightarrow{J} \quad (Ampere's\ Law),$$

coupled with Gauss's law $\nabla \cdot \overrightarrow{B} = 0$, $\nabla \cdot \overrightarrow{D} = \rho$, where $\overrightarrow{J} = \sigma \overrightarrow{E}$ is electric current density, σ is electrical conductivity, and ρ is electric charge density. For linear materials we relate the magnetic flux density vector $\overrightarrow{B}$ to the magnetic field vector $\overrightarrow{H}$ and the electric flux density vector $\overrightarrow{D}$ to the electric field vector $\overrightarrow{E}$ using $\overrightarrow{B} = \mu\overrightarrow{H}, \overrightarrow{D} = \varepsilon\overrightarrow{E}$, where ε is the dielectric permittivity that describes the particular media and μ is the magnetic permeability. We consider discontinuities in the media, i.e. in ε.

In two dimensions the set of 6 equations decouples into two independent sets of 3 equations denoted as TM_z and TE_z (transverse magnetic and electric fields).

Consider the two dimensional TM_z mode Maxwell equations in a lossless material, i.e. $\sigma = 0$:

$$\begin{cases} \frac{\partial H_x}{\partial t} &= -\frac{1}{\mu}\frac{\partial E_z}{\partial y}, \\ \frac{\partial H_y}{\partial t} &= \frac{1}{\mu}\frac{\partial E_z}{\partial x}, \\ \frac{\partial E_z}{\partial t} &= \frac{1}{\varepsilon}\left(\frac{\partial H_y}{\partial x} - \frac{\partial H_x}{\partial y}\right). \end{cases}$$

Differentiating the first equation in y, the second in x and the last in t, assuming ε, μ are time independent, one gets

$$\begin{cases} \frac{\partial^2 H_x}{\partial t \partial y} &= -\frac{\partial}{\partial y}\left(\frac{1}{\mu}\frac{\partial E_z}{\partial y}\right), \\ \frac{\partial^2 H_y}{\partial t \partial x} &= \frac{\partial}{\partial x}\left(\frac{1}{\mu}\frac{\partial E_z}{\partial x}\right), \\ \frac{\partial^2 E_z}{\partial t^2} &= \frac{1}{\varepsilon}\left(\frac{\partial^2 H_y}{\partial x \partial t} - \frac{\partial^2 H_x}{\partial y \partial t}\right). \end{cases}$$

Substituting the first two equations into the third one, we get the wave equation

for E_z:

$$\frac{\partial^2 E_z}{\partial t^2} = \frac{1}{\varepsilon}\left(\frac{\partial}{\partial x}\left(\frac{1}{\mu}\frac{\partial E_z}{\partial x}\right) + \frac{\partial}{\partial y}\left(\frac{1}{\mu}\frac{\partial E_z}{\partial y}\right)\right).$$

Since for most materials μ is constant while ε is not, we rewrite the last equation as

$$\frac{\partial^2 E_z}{\partial t^2} = c^2(x,y)\left(\frac{\partial^2 E_z}{\partial x^2} + \frac{\partial^2 E_z}{\partial y^2}\right),$$

where $c^2(x,y) = \frac{1}{\varepsilon(x,y)\mu_0}$. When we apply the Fourier transform in time the wave equation becomes the Helmholtz equation $\Delta u + k^2 u = 0$ where $k^2 = \frac{\omega^2}{c^2}$ is the wavenumber, $k = k(x,y)$.

In physical applications, the quantity $c(x,y)$ may be discontinuous and therefore the wavenumber may be only a piecewise continuous function. The propagation of waves across media with material discontinuities is encountered in a wide variety of settings. For example, classical problems of electromagnetic scattering/transmission often involve sharp variations of material properties. These problems appear in applications that range from radar imaging to telecommunication devices.

Our discussion here concerns the numerical solution of the Helmholtz equation for domains where the boundaries and interfaces do not necessarily conform to the discretization mesh. The material properties are assumed smooth between the interfaces, whereas at the interfaces they may undergo jumps. In Section 1.1 we describe the general problem and introduce the Helmholtz equation in different coordinate systems. In Section 1.2 we review existing numerical methods while in Chapter 2 we explain our approach in solving problems with discontinuities. In Chapter 3 we present details of our implementation with representative results followed by our conclusions in Chapter 4.

1.1 Helmholtz equation

The Helmholtz equation, named for Hermann von Helmholtz, is the elliptic partial differential equation

$$\Delta u + k^2 u = F, \tag{1.1}$$

where $\Delta = \nabla^2$ is the Laplacian, $u = u(\boldsymbol{x})$ is the scalar unknown field, e.g., acoustic pressure or linearly polarized electric field ($\boldsymbol{x} \in \mathbb{R}^n$), and $F = F(\boldsymbol{x})$ is the source term, which, if present, will always be compactly supported in $\mathbb{R}^n$. The quantity $k = k(\boldsymbol{x})$ in (1.1) is the wavenumber, $k^2 = k_0^2 \nu^2$ and $k_0^2 = \frac{\omega_0^2}{c_0^2}$, where ω_0 is the fixed carrier frequency. c is the propagation speed in the unobstructed medium (also fixed, as the speed of sound in ambient fluid at a constant temperature or the speed of light in vacuum), and $\nu = \nu(\boldsymbol{x})$ is the refraction index. The physical interpretation of $\nu(\boldsymbol{x})$ is the ratio of the reference speed c to the actual propagation speed at a given $\boldsymbol{x}$. The function $\nu(\boldsymbol{x})$, and hence $k(\boldsymbol{x})$, can be only piecewise continuous. The Helmholtz equation is used to model a variety of important physical processes and phenomena in acoustics and electromagnetism. In this thesis we consider two dimensional problems with material discontinuities and boundaries that are not aligned to the numerical grid.

Consider an incident wave, $u^{(\text{inc})}$, impinging on an arbitrary body Ω_1, see Figure 1.1. It generates a transmitted wave, $u^{(\text{trans})}$, and partially gets reflected, $u^{(\text{scat})}$. It could be an ultrasound wave scanning a kidney, an embryo, a carrier wave of a cellular phone, a Wi-Fi radio signal passing through a wall or the head of a human. In the frequency domain, such a scenario is described using the Helmholtz operator

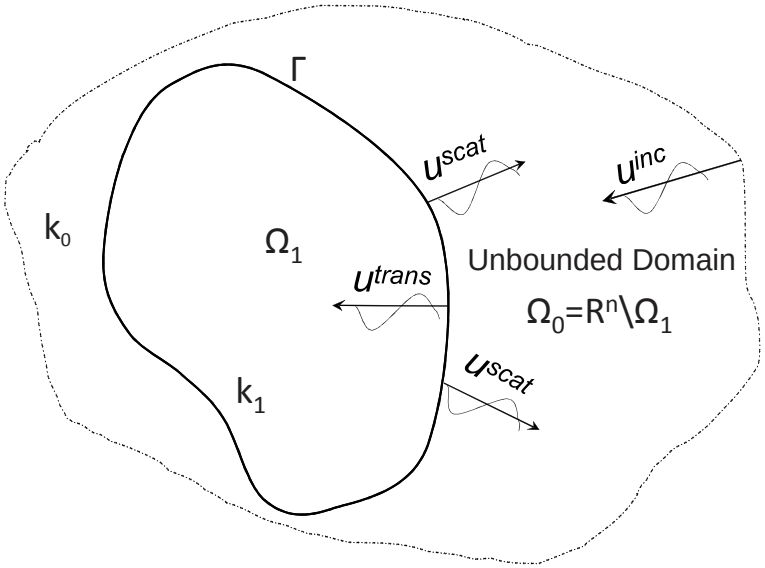

Figure 1.1: Schematic Problem

$\boldsymbol{L}_q = \Delta + k_q^2$ in the domain Ω_q where $q \in 0, 1$ as follows

$$\begin{cases} \boldsymbol{L}_0 u = 0 & \boldsymbol{x} \in \Omega_0, \quad (1.2a) \\ \boldsymbol{L}_1 u = F(\boldsymbol{x}) & \boldsymbol{x} \in \Omega_1, \quad (1.2b) \end{cases}$$

$F(\boldsymbol{x})$ is the source term, $u(\boldsymbol{x}) = u^{(\text{inc})}(\boldsymbol{x}) + u^{(\text{scat})}(\boldsymbol{x})$ for each $\boldsymbol{x} \in \Omega_0$. $u^{(\text{inc})} = e^{-ik(x\cos\theta + y\sin\theta)}$ is a given plane wave impinging from an incident angle θ. Thus, problem (1.2) is driven by incident wave $u^{(\text{inc})}$ and the source term $F(\boldsymbol{x})$. Across the interface Γ between the two subdomains, Ω_1 and Ω_0, one typically requires that the function and it's first normal derivative be continuous. Such problems may have multiple solutions. To ensure uniqueness one additionally requires that the scattered field $u^{(\text{scat})}$ has no incoming components. This is guaranteed by the (n-dimentional)

Sommerfeld radiation condition:

$$\frac{\partial u^{(\mathrm{scat})}(\boldsymbol{x})}{\partial |\boldsymbol{x}|} + ik_0 u^{(\mathrm{scat})}(\boldsymbol{x}) = \mathrm{o}\left(|\boldsymbol{x}|^{\frac{1-n}{2}}\right), \quad \text{as} \quad |\boldsymbol{x}| \to \infty. \tag{1.3}$$

Problem (1.2) can be generalized for several bodies $\{\Omega_q\}_{q=1}^n \subset \Omega_0$ which are either mutually disjoint or share an interface. The problem is then defined as following:

$$\begin{cases} \boldsymbol{L}_0 u = 0 & \boldsymbol{x} \in \Omega_0, \\ \boldsymbol{L}_1 u = F_1(\boldsymbol{x}) & \boldsymbol{x} \in \Omega_1, \\ \vdots & \\ \boldsymbol{L}_n u = F_n(\boldsymbol{x}) & \boldsymbol{x} \in \Omega_n, \end{cases} \tag{1.4}$$

driven by $u^{(\mathrm{inc})}$ and a set $F_i,\ i = 1, 2, \ldots, n$. Across every interface one may require that the function and it's first normal derivative are continuous. One can also define other interface conditions, those still can be handled by the method described below, see equation (2.18). At infinity the Sommerfeld condition is required for uniqueness.

On the other hand, when one solves only an exterior (Ω_0) or an interior (Ω_1) problem then only one boundary condition should be provided. For an exterior problem, in addition to the Sommerfeld condition, one often requires that $u^{(\mathrm{scat})} = -u^{(\mathrm{inc})}$ or $u_n^{(\mathrm{scat})} = -u_n^{(\mathrm{inc})}$ on Γ which is the Dirichlet $u|_\Gamma = 0$ and Neumann $u_n|_\Gamma = 0$ scattering problem, respectively. u_n, $u_n^{(\mathrm{scat})}$ and $u_n^{(\mathrm{inc})}$ are the first normal derivatives of u, $u^{(\mathrm{scat})}$, and $u^{(\mathrm{inc})}$ respectively.

Mathematical problems are often described better in some specific coordinate system while in another system of coordinates the problem may have a less conve-

nient representation. In boundary value problems one may change the coordinate system to match the shape of the boundary, e.g. use polar coordinates for circular domains or elliptical coordinates domains shaped as ellipses. However, when the shape becomes more complicated the change of coordinates may become a major difficulty. Furthermore, choosing a complicated coordinate system may lead to an poor quality grid or singular points, thus ruining the advantage of changing coordinates. Hence, there is a tradeoff between the complexity of the grid and complexity of the problem.

For a generally shaped body, constructing a body fitted coordinate system needs to be done numerically. Achieving this with high accuracy may be difficult. For a complicated body, especially in 3D, it may be impossible to construct a simple body fitted coordinate system. A partial remedy may be to use the multi-block overlapping grids, also known as chimera grids, see, e.g., [30]. Those grids, however, do not completely remove the difficulty associated with fitting the grid to a curvilinear boundary. They rather partially alleviate it, because the grid no longer has to be fitted to the entire boundary. Instead, different blocks serve different fragments of the boundary, and instead of point matching, the grids are allowed to overlap on some common regions, which simplifies their generation. Yet another alternative is to use the finite element method based on an unstructured grid, see Section 1.2.

In this work we use a finite difference scheme with a regular grid regardless of the shape of the body, and still obtain high order accuracy of the numerical solution.

1.1.1 Helmholtz equation in different coordinate systems

We next recast the Helmholtz equation two non-Cartesian coordinate systems. The main difficulty is the Laplacian, which is defined as divergence of the vector gradient, i.e. $\Delta u = \operatorname{div}(\operatorname{grad} u)$; one denotes $\operatorname{div} = \nabla\cdot$ and $\operatorname{grad} = \nabla$ to get $\Delta = \nabla \cdot \nabla = \nabla^2$. In the Cartesian coordinates one gets

$$\Delta = \nabla \cdot \left(\frac{\partial}{\partial x_1}, \dots, \frac{\partial}{\partial x_n} \right) = \sum_{j=1}^{n} \frac{\partial^2}{\partial x_j^2}.$$

Things are more complicated in polar coordinates, which are given as

$$\begin{cases} x = r\cos\theta, \\ y = r\sin\theta, \end{cases}$$

where $r \geq 0$ is a radius and $0 \leq \theta \leq 2\pi$ is the angular coordinate. Using the chain rule one gets

$$\begin{aligned} \frac{\partial^2}{\partial x^2} &= \frac{\partial}{\partial x}\left(\frac{\partial r}{\partial x}\frac{\partial}{\partial r} + \frac{\partial \theta}{\partial x}\frac{\partial}{\partial \theta} \right) = \frac{\partial}{\partial x}\left(\cos\theta \frac{\partial}{\partial r} - \frac{\sin\theta}{r}\frac{\partial}{\partial \theta} \right) \\ &= \cos\theta \frac{\partial}{\partial r}\left(\cos\theta \frac{\partial}{\partial r} - \frac{\sin\theta}{r}\frac{\partial}{\partial \theta} \right) - \frac{\sin\theta}{r}\frac{\partial}{\partial \theta}\left(\cos\theta \frac{\partial}{\partial r} - \frac{\sin\theta}{r}\frac{\partial}{\partial \theta} \right) \\ &= \cos\theta \left(\cos\theta \frac{\partial^2}{\partial r^2} - \left(\frac{\sin\theta}{r}\frac{\partial^2}{\partial r \partial \theta} - \frac{\sin\theta}{r^2}\frac{\partial}{\partial \theta} \right) \right) \\ &- \frac{\sin\theta}{r}\left(\cos\theta \frac{\partial^2}{\partial \theta \partial r} - \sin\theta \frac{\partial}{\partial r} - \left(\frac{\sin\theta}{r}\frac{\partial^2}{\partial \theta^2} + \frac{\cos\theta}{r}\frac{\partial}{\partial \theta} \right) \right) \end{aligned}$$

and consequently

$$\begin{aligned}\frac{\partial^2}{\partial y^2} &= \frac{\partial}{\partial y}\left(\frac{\partial r}{\partial y}\frac{\partial}{\partial r}+\frac{\partial \theta}{\partial y}\frac{\partial}{\partial \theta}\right)=\frac{\partial}{\partial y}\left(\sin\theta\frac{\partial}{\partial r}+\frac{\cos\theta}{r}\frac{\partial}{\partial \theta}\right)\\ &= \sin\theta\frac{\partial}{\partial r}\left(\sin\theta\frac{\partial}{\partial r}+\frac{\cos\theta}{r}\frac{\partial}{\partial \theta}\right)+\frac{\cos\theta}{r}\frac{\partial}{\partial \theta}\left(\sin\theta\frac{\partial}{\partial r}+\frac{\cos\theta}{r}\frac{\partial}{\partial \theta}\right)\\ &= \sin\theta\left(\sin\theta\frac{\partial^2}{\partial r^2}+\frac{\cos\theta}{r}\left(\frac{\partial^2}{\partial\theta\partial r}-\frac{1}{r}\frac{\partial}{\partial\theta}\right)\right)\\ &+ \frac{\cos\theta}{r}\left(\cos\theta\left(\frac{\partial}{\partial r}+\frac{1}{r}\frac{\partial^2}{\partial\theta^2}\right)+\sin\left(\frac{\partial^2}{\partial r\partial\theta}-\frac{1}{r}\frac{\partial}{\partial\theta}\right)\right)\end{aligned}$$

to arrive at the well known formulation

$$\Delta=\frac{\partial^2}{\partial x^2}+\frac{\partial^2}{\partial y^2}=\frac{\partial^2}{\partial r^2}+\frac{1}{r}\frac{\partial}{\partial r}+\frac{1}{r^2}\frac{\partial^2}{\partial\theta^2}.$$

Such a complicated derivation is usually not convenient. Fortunately, better methods exist. Consider an orthogonal curvilinear coordinate system $\boldsymbol{y} = y(\boldsymbol{x}), \boldsymbol{x} \in \mathbb{R}^n$. Define scale factors (also called metrics or Lame coefficients) as $h_j^2 = \sum_{m=1}^n \left(\frac{\partial y_m}{\partial x_j}\right)^2$. Then the vector gradient becomes $\nabla = \left(\frac{1}{h_1}\frac{\partial}{\partial x_1}, \ldots, \frac{1}{h_n}\frac{\partial}{\partial x_n}\right)$ and the Laplacian becomes

$$\Delta = \frac{1}{\prod_{j=1}^n h_j}\sum_{m=1}^n \frac{\partial}{\partial x_m}\left(\frac{\prod_{p\neq m} h_p}{h_m}\frac{\partial}{\partial x_m}\right).$$

Returning to polar coordinates one gets

$$\begin{aligned}h_r &= \sqrt{\left(\frac{\partial x}{\partial r}\right)^2+\left(\frac{\partial y}{\partial r}\right)^2}=\sqrt{\cos^2\theta+\sin^2\theta}=1,\\ h_\theta &= \sqrt{\left(\frac{\partial x}{\partial \theta}\right)^2+\left(\frac{\partial y}{\partial \theta}\right)^2}=\sqrt{r^2\sin^2\theta+r^2\cos^2\theta}=r,\end{aligned}$$

and the Laplacian is:

$$\Delta = \frac{1}{h_r h_\theta}\left[\frac{\partial}{\partial r}\left(\frac{h_\theta}{h_r}\frac{\partial}{\partial r}\right) + \frac{\partial}{\partial \theta}\left(\frac{h_r}{h_\theta}\frac{\partial}{\partial \theta}\right)\right] = \frac{1}{r}\left[\frac{\partial}{\partial r}\left(r\frac{\partial}{\partial r}\right) + \frac{\partial}{\partial \theta}\left(\frac{1}{r}\frac{\partial}{\partial \theta}\right)\right]$$
$$= \frac{1}{r}\left[\frac{\partial}{\partial r} + r\frac{\partial^2}{\partial r^2} + \frac{1}{r}\frac{\partial^2}{\partial \theta^2}\right] = \frac{\partial^2}{\partial r^2} + \frac{1}{r}\frac{\partial}{\partial r} + \frac{1}{r^2}\frac{\partial^2}{\partial \theta^2}.$$

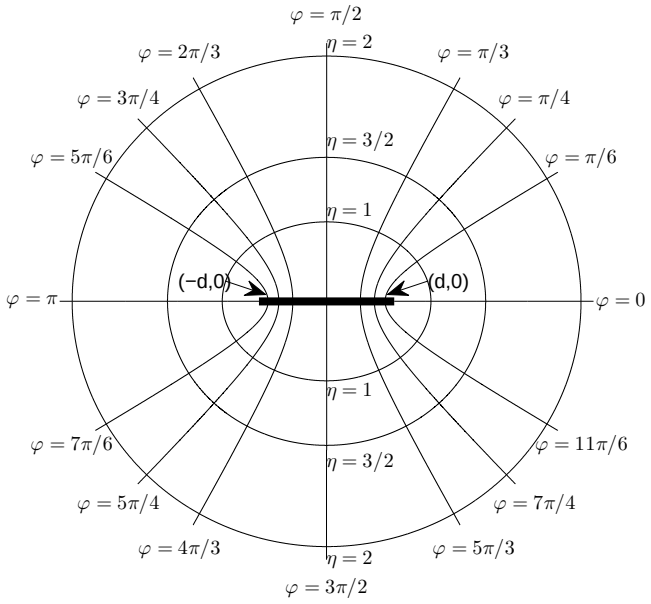

Figure 1.2: Elliptical Coordinates

Elliptical coordinates are given by $x + iy = d\cosh(\eta + i\varphi)$ or, equivalently,

$$\begin{cases} x = d\cosh\eta\cos\varphi \\ y = d\sinh\eta\sin\varphi \end{cases} = \begin{cases} x = a\cos\varphi \\ y = b\sin\varphi \end{cases} \tag{1.5}$$

where d is semi-focal distance, η is an elliptical radius, so that each value of η defines an unique ellipse with $d = \sqrt{a^2 - b^2}$, $a = d\cosh\eta$, and $b = d\sinh\eta$ are the major and minor semi-axes, respectively, and $\frac{x^2}{a^2} + \frac{y^2}{b^2} = \cos^2\varphi + \sin^2\varphi = 1$.

In this case we have

$$\begin{aligned} h_\eta &= h_\varphi = d\sqrt{\sinh^2\eta\cos^2\varphi + \cosh^2\eta\sin^2\varphi} \\ &= d\sqrt{\sinh^2\eta\cos^2\varphi + \cosh^2\eta(1-\cos^2\varphi)} \\ &= d\sqrt{-(\cosh^2\eta - \sinh^2\eta)\cos^2\varphi + \cosh^2\eta} \\ &= d\sqrt{\cosh^2\eta - \cos^2\varphi} = d\sqrt{\sinh^2\eta + \sin^2\varphi} \end{aligned}$$

and consequently,

$$\Delta = \frac{1}{h_\eta^2}\left(\frac{\partial^2}{\partial\eta^2} + \frac{\partial^2}{\partial\varphi^2}\right).$$

1.2 Numerical approximation of differential equations

Finite difference (FD) methods were historically the first methodology for the numerical solution of differential equations [54, 49]. They still remain a very powerful tool, and for smooth solutions on regular grids lead to inexpensive and efficient algorithms. Their primary disadvantage is in dealing with more complicated geometries and solutions with low regularity. In particular, when the boundary is not aligned with the grid staircase meshing doesn't provide the required accuracy. For example, consider a circular body Ω_1 in Cartesian coordinates, see Figure 1.3. Denote the circular boundary shape $\Gamma = \partial\Omega_1$ and let $(x, y) \in \Gamma$. Let $v_{i,j}$ be the approximate value of the solution v at nodes $x_i = x + \delta x$ and $y_j = y + \delta y$, i.e. $v_{i,j} \approx v(x_i, y_j)$. Let $b(x, y)$ be the boundary value given on curve Γ and assume $(x_i, y_j) \notin \Gamma$. The

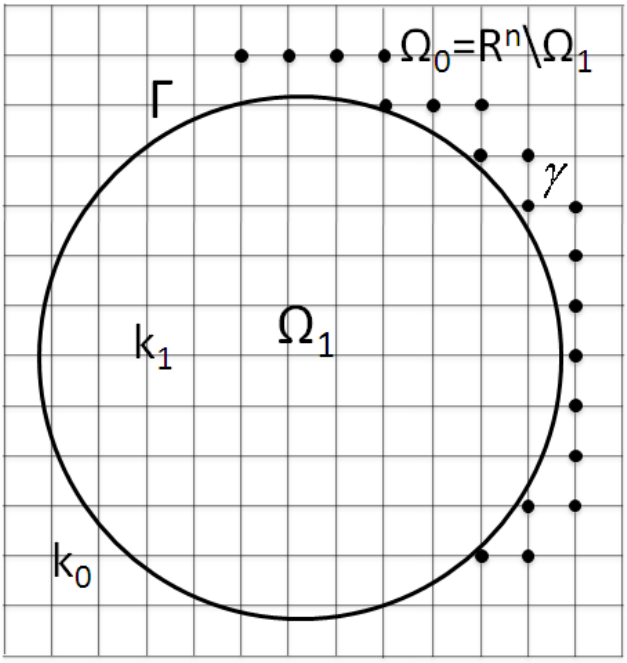

Figure 1.3: Circular body in Cartesian coordinates, staircase-mesh γ.

staircase approach states $v_{i,j} = b(x, y)$. However, since

$$v(x_i, y_j) = b(x, y) + \nabla v(x, y) \cdot (\delta x, \delta y) + O(\delta x^2 + \delta y^2),$$

and ∇v is not available, the boundary data is approximated by a first order method. For additional discussion about staircase meshing and it's disadvantages see [34]. The immersed boundary method (IBM) of Peskin [45] requires a modification of the governing equations to treat the geometric irregularities, and a smoothed approximation of the δ function to treat the discontinuity at the interface, to achieve first order accuracy. It has been improved upon with the immersed interface method (IIM) of LeVeque and Li [37] (also see their book [38]). They enforce the jump at the interface directly in the finite difference scheme. The implementation suffers from

increased complexity, but second order accuracy can be achieved. Later Zhang and LeVeque [71] used fictitious points to modify the discrete linear system to account for the correct position of the interface and the proper physical interface conditions. Recently Xu [68] developed efficient and stable boundary condition capturing immersed interface method for simulating a flow around an object. The method have almost a second order accuracy for the velocity and above first order for the pressure. Johansen and Colella [36] used Embeded boundary to solve Poison equation with variable coefficients and Dirichlet boundary condition on irregular domain using Cartesian grid with second order accuracy. They extended the solution into a fictitious domain and the resultant linear system is non-symmetric. However it is compatible with a multigrid and adaptive mesh techniques which should improve the complexity. These techniques though aren't immediately extendable for the Helmholtz equation. Recently, Crockett, Colella and Graves [16] used this method for Poison and heat equations with discontinuous coefficients and reached second order. To the best of our knowledge, there are no reported uses in the literature of those methods for anything but simple Dirichlet, Neumann, or interface conditions (continuity of the solution and its normal flux), changing the boundary condition requires major changes to the algorithm [16], and extension to higher than second order accuracy is not straightforward. The ghost-cell immersed boundary method (GCIBM) [62] employes extrapolation to impose the boundary condition implicitly; and the immersed boundary projection method (IBPM) [60] treats the no-slip boundary conditions along with the immersed boundary as a Lagrange multiplier. All these methods are difficult to generalize to high order accuracy.

A high order method (up to sixteenth-order accuracy) for elliptic equations, for

a matched interface and boundary method (MIB), was introduced by Zhou et al. [74, 73]. The high-order interface conditions are implemented by repeatedly matching the interface conditions across the given interface using low-order numerical integration rules. A special procedure is proposed to determine the accurate fictitious values required for the high-order scheme. This method is meant to treat interface curves that are not aligned to the grid, jumps in coefficients, and singular sources. However, all the examples presented in [74, 73] reduce to a problem with only singular sources. Six new versions of IIM of fourth order accuracy were provided by Zhong [72]. He used two different polynomials on both sides of the interface and enforced that the two polynomials satisfy two interface conditions. Zhong used a wide stencil that requires additional purely numerical boundary conditions. The only examples provided were the Poisson equation with a singular source or equivalent.

An interesting solver was presented by Abarbanel and Ditkowski [1]. They considered a diffusion equation in one and two dimensions on a domain with a body whose boundary points do not coincide with the nodes of a rectangular mesh. In order to reach the fourth order accuracy, energy methods were used in conjunction with simultaneous approximation terms (SAT). However, the resulting linear system should be negative definite, which is not the case for the Helmholtz equation.

The finite element method (FEM) [58, 13, 7] and its extensions (GFEM, XFEM, discontinuous enrichment [22, 23]), as well as discontinuous Galerkin methods [31], are also well established and powerful. Their strength is in dealing with complex geometries and low regularity of the solutions.

In practical problems of wave propagation though, especially in 3D, both FD

and FEM have serious limitations because of their relatively high "points-per-wavelength" requirement, as well as numerical dispersion and, more generally, numerical pollution [35, Section 4.6.1], [5, 2]. The numerical phase velocity of the wave in these methods depends on the wavenumber k, so a propagating packet of waves with different frequencies gets distorted in the simulation. Furthermore, the numerical error depends strongly on the wavenumber k, see [35], and this kind of error is inherent in FEM/FD. The error behaves like $h^p k^{p+1}$ where p is the order of accuracy of the scheme. So the number of points per wavelength needed for a given accuracy grows like $k^{1/p}$. Hence, for higher order accurate schemes the pollution effect is reduced.

A high order approximation can be built for arbitrary boundaries using FEM, but only in fairly sophisticated and costlier algorithms with isoparametric elements [58]. In discontinuous enrichment / discontinuous Galerkin methods and GFEM, high order accuracy also requires additional degrees of freedom, which entails an additional computational cost. These additional degrees of freedom lead to expanded approximating spaces which are capable of approximating a very broad class of functions that may, in principle, have irregularities anywhere in the computational domain. This is a significant advantage in problems of great geometrical and physical complexity. However, for simpler problems with smooth solutions much more targeted and economical approximations, in narrower functional spaces, are available using FD methods.

A FD approach, on the other hand, does not introduce additional unknowns per grid node and thus remains inexpensive. It, however, requires a higher regularity of the solution to guarantee consistency, and may also need a wider stencil, which

complicates the boundary conditions (more precisely, requires additional "purely numerical" boundary conditions).

Schemes known as Collatz "Mehrstellen" [14], equation-based and related compact schemes [55, 66, 69, 33, 3, 4, 8, 9], as well as Trefftz-FLAME [63], don't expand the stencil and therefore don't require additional nonphysical boundary conditions. Furthermore, as opposed to classical FEM which expands the approximating space, these methods reduce it to the class of solutions rather than the much broader class of generic sufficiently smooth functions. This does not imply any loss of generality, because according to the Lax theorem, for convergence one does not need to have consistency for any functions except the solutions.

1.2.1 Compact Equation–Based Schemes

We next present the compact scheme used hereafter in our simulations. Consider $u_{i,j} = u(x_i, y_j)$, then the second order accurate approximation to the second derivative in x yields

$$D_{xx}u_{i,j} = \frac{u_{i+1,j} - 2u_{i,j} + u_{i-1,j}}{h_x^2}. \tag{1.6}$$

Using Taylor series one can show that

$$D_{xx}u_{i,j} = u_{xx} + \frac{h_x^2}{12}u_{xxxx} + O\left(h^4\right).$$

To obtain a 4th order approximation one eliminates u_{xxxx} using the two dimensional Helmholtz equation $-u_{xx} = u_{yy} + k^2 u - F$. Differentiating this equation we obtain

$$-u_{xxxx} = u_{yyxx} + \left(k^2 u\right)_{xx} - F_{xx} = D_{yy} D_{xx} u + D_{xx}\left(k^2 u - F\right) + O(h^2)$$

where $D_{yy} u_{i,j} = \frac{u_{i,j+1} - 2u_{i,j} + u_{i,j-1}}{h_y^2}$. Thus, the fourth order compact scheme is given by

$$\begin{aligned} \tilde{D}_{xx} u_{i,j} &= D_{xx} u_{i,j} - \frac{h_x^2}{12}\left(D_{yy} D_{xx} u + D_{xx}\left(k^2 u - F\right)\right) \\ &= u_{xx} + O\left(h^4\right). \end{aligned} \tag{1.7}$$

Using a similar approach for the derivative in y, one gets the scheme of Singer and Turkel [55]

$$\begin{aligned} &\left(D_{xx} + D_{yy} + k^2 + \frac{1}{12}\left(h_x^2 + h_y^2\right) D_{xx} D_{yy}\right) u + \frac{1}{12}\left(h_x^2 D_{xx} + h_y^2 D_{yy}\right)\left(k^2 u\right) \\ &= \left(1 + \frac{1}{12}\left(h_x^2 D_{xx} + h_y^2 D_{yy}\right)\right) F. \end{aligned} \tag{1.8}$$

Compact fourth order accurate schemes for the more general Helmholtz -type equations with variable coefficients have been obtained in [8, 9]. A sixth order scheme for constant coefficients is constructed in [56]. A similar compact sixth order scheme for the case of a variable wavenumber $k = k(\boldsymbol{x})$ is presented in [65].

A distinctive feature of the compact equation-based schemes is that they exploit two stencils. The first one applies to the left-hand side of the equation, i.e., it operates on the unknown solution. The second one applies to the right-hand side of

the equation, i.e. , it operates on the given data (source terms). The equation-based and similar high order schemes reduce pollution while keeping the treatment of the boundary conditions simple. Since the order of the resulting difference equation is equal to the order of the differential equation, no nonphysical boundary conditions are required.

1.2.2 Reduction to integral equations

In traditional boundary element methods (BEM), linear boundary value problems are transformed into integral equations with respect to equivalent boundary sources, which are subsequently discretized. Practical applications of such methods date back to the 1960s. They impose no limitations on the shape of the boundary and automatically account for the correct far field behavior. There are, however, several major disadvantages:

- *Full matrices* — in contrast with the sparse FD and FEM matrices. (Cases of quasi-sparse integral equations, due to the rapid decay of Green's functions in space, are exceptional, [46]).
- A *relatively narrow treatment of the boundary conditions.* Care must be exercised, on a case-by-case basis, in the choice of the equivalent boundary sources, so that the resulting Fredholm equation is of the second kind (well-posed) rather than first. Moreover, mixed (Dirichlet/Neumann, etc.) or less standard (Robin, etc.) conditions require a special development.
- *Singular integral kernels* (*the most serious disadvantage in practice*). Imme-

diately at the boundary points, the kernel singularity can usually be handled analytically, and the fields remain bounded as long as the surfaces are smooth. However, for points *in the vicinity* of a surface, the evaluation of the integral is problematic, as analytical expressions are usually unavailable and numerical quadratures require extreme care.

- *Limitation to constant coefficients,* i.e., to homogeneous media, — these methods require explicit knowledge of the fundamental solution of the corresponding differential operator.

Significant progress in Fast Multipole Methods (FMM) [25, 12, 40, 70, 24] has helped alleviate the first disadvantage of boundary methods. FMM accelerates the computation of fields due to distributed sources — or equivalently, matrix-vector multiplications for the dense system matrices. But the second and especially the third disadvantages are more difficult to overcome, whereas the fourth one can only be addressed by switching to much less efficient volume integral methods or finding the fundamental solution by numerical means, which is both expensive and leads to additional errors.

Chapter 2

Problems with non-aligned interfaces

In this chapter we describe our main methodological approach for solving problem (1.2). We consider a divide and conquer approach based on wave splitting into incoming and outgoing waves. We assemble the overall solution from the set of individual solutions to the auxiliary problem (AP). The AP is defined independently for each sub-domain Ω_q, see (1.2). The choice of the AP is relatively flexible; it can be formulated so as to enable an easy and economical numerical solution. Our new method uses only simple structured grids, e.g., Cartesian or polar, regardless of the shape of the boundaries or interfaces. In the regions of smoothness, it employs high order accurate finite difference schemes on compact stencils, see Section 1.2.1. They do not require any additional boundary conditions besides those needed for the underlying differential equation itself.

We first illustrate the key components of the numerical methodology that we propose with a one dimensional example and then generalize this simple one dimensional model of wave splitting into a multidimensional one using Calderon's projections, see [39].

Consider the following one-dimensional problem

$$\begin{cases} u_{xx} + k_0^2 u = 0 & x < 0, \\ u_{xx} + k_1^2 u = 0 & x > 0, \end{cases} \tag{2.1}$$

driven by an incoming wave $u^{(\text{inc})} = Ae^{ik_0 x}$, which propagates through the domain. It generates the transmitted wave $u_1 = Te^{ik_1 x}$ for $x > 0$ and partially gets reflected and produces $u_0 = Re^{-ik_0 x}$ for $x < 0$, see Figure 2.1.

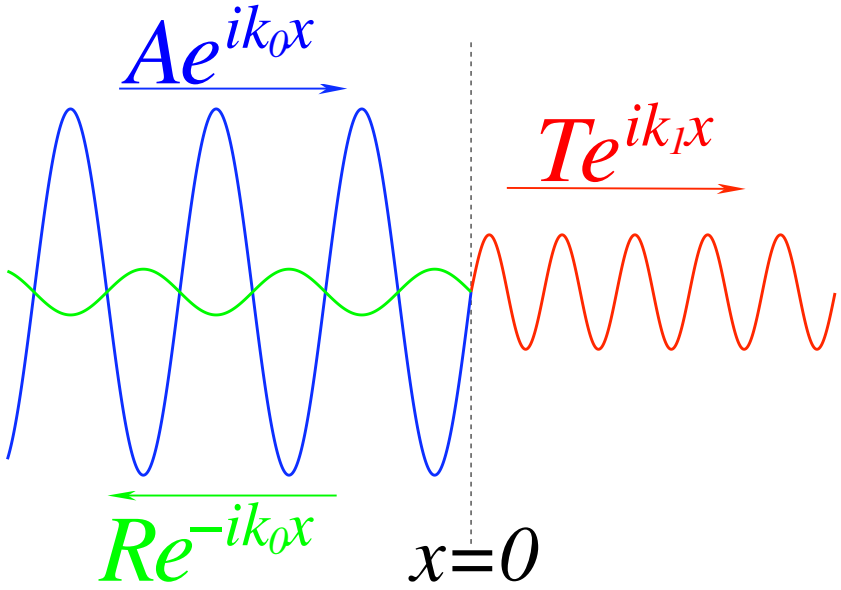

Figure 2.1: 1D transmission problem.

To find the amplitudes T and R one requires that $u(x)$ and $u'(x)$ be continuous at $x = 0$. This yields two linear algebraic equations: $A + R = T$ and $k_0 A - k_0 R = k_1 T$, which provide the Fresnel reflection and transmission coefficients:

$$T = A\frac{2k_0}{k_0 + k_1}, \qquad R = A\frac{k_0 - k_1}{k_0 + k_1}. \tag{2.2}$$

However, one can solve this problem without introducing unknown amplitudes and instead employ the relation that describes the entire family of waves: right traveling $u' - ik_1 u = 0$ and the left traveling $u' + ik_0 u = 0$. In particular, the transmitted wave u_1 satisfies the right traveling equation. Likewise $u_0 + u^{(\text{inc})}$ satisfies the inhomogeneous left traveling equation on $x < 0$. So we can rewrite (2.1) as the following system of equations

$$\begin{cases} u' - ik_1 u = 0 & x > 0, \\ u' + ik_0 u = 2ik_0 A e^{ik_0 x} & x < 0, \end{cases} \tag{2.3}$$

together with the requirement that $u(x), u'(x)$ be continuous, which yields:

$$u(0) = A\frac{2k_0}{k_0 + k_1}, \qquad u'(0) = A\frac{2ik_1 k_0}{k_0 + k_1}. \tag{2.4}$$

Since $T = A + R = u(0)$, we arrive at the same answer (2.2).

The system of equations (2.3) shows that if the impinging wave changes (new amplitude A), then the problem does not have to be solved all over again, because only the right-hand side of inhomogeneous part changes. In one dimension the difference is negligible. However, in multiple space dimensions a methodology built

around the same idea proves very useful. For example, in inverse problems one may cheaply use multiple impinging waves or different incident angles to get additional information to improve the accuracy.

In Section 2.1 we present the theoretical part for *Calderon's boundary equations with projections* which replaces the system of equations (2.3). We conclude chapter Chapter 2 describing the discrete counterparts of the boundary equations with projections developed by V.S. Ryaben'kii, see [50], in Section 2.3. The pseudocode of the main algorithm for solving (1.2) is described in Section 2.3.1, followed by examples and additional explanation in Sections 2.3.2 – 2.3.7.

2.1 Calderon's Potentials

In this section we present the Calderon potentials, which yield the wave splitting described above, see [39]. All the incoming and outgoing waves for a given Ω_q (analogues of the right and left traveling waves in 1D example, see Figure 2.1) belong to the image (range) and kernel (null space), respectively, of the corresponding projection operator. We consider time-harmonic wave propagation with a piecewise continuous index of refraction.

Let $\boldsymbol{L}_q$ denote the Helmholtz operator of equation (1.1) with $k = k_q$, where $q \in \{0, 1\}$, and the geometry as depicted in Figure 1.1, i.e. we consider problem (1.2). Let $G_q(\boldsymbol{x})$ be the fundamental solution of $\boldsymbol{L}_q$. Let the functions $\xi^I(\boldsymbol{x})$ and $\xi^{II}(\boldsymbol{x})$ belong to C^2, C^1 respectively for $\boldsymbol{x} \in \Gamma$. We introduce the vector $\boldsymbol{\xi}_\Gamma = (\xi^I, \xi^{II})$ which we call the vector density. A generalized potential of Calderon type with the

vector density $\boldsymbol{\xi}_\Gamma$ is defined by

$$\boldsymbol{P}_{\Omega_q}\boldsymbol{\xi}_\Gamma(\boldsymbol{x}) = \sigma_q \int_\Gamma \left(\xi^I(y) \frac{\partial G_q}{\partial \boldsymbol{n}}(x-y) - \xi^{II}(y) G_q(x-y) \right) ds_{\boldsymbol{y}}, \quad \boldsymbol{x} \in \Omega_q, \tag{2.5}$$

where $\frac{\partial}{\partial \boldsymbol{n}}$ denotes the normal derivative and $\sigma_q = (-1)^{q+1}$ changes the sign so that we always consider a normal pointing in the same direction regardless of the domain Ω_q. Given the solution $u(\boldsymbol{x})$ to the problem (1.2) one defines a vector density $u_\Gamma = \left(u, \frac{\partial u}{\partial \boldsymbol{n}}\right)\big|_\Gamma$, and rewrites Green's solution to the problem (1.2) as:

$$u(\boldsymbol{x}) = \begin{cases} \boldsymbol{P}_{\Omega_1} u_\Gamma + \int_{\Omega_1} G_1(\boldsymbol{x}-\boldsymbol{y}) F(\boldsymbol{y}) d\boldsymbol{y} & \boldsymbol{x} \in \Omega_1, \\ \boldsymbol{P}_{\Omega_0} u_\Gamma & \boldsymbol{x} \in \Omega_0. \end{cases} \tag{2.6}$$

Let $\boldsymbol{\xi}_\Gamma = (\xi^I, \xi^{II})$ belong to the space $\boldsymbol{S}$. Inspired by the one dimensional example we wish to split $\boldsymbol{S}$ into incoming $\boldsymbol{S}^q_+$ and outgoing $\boldsymbol{S}^q_-$ waves for a given Ω_q such that their direct sum is $\boldsymbol{S}$, i.e.

$$\boldsymbol{S} = \boldsymbol{S}^q_+ \oplus \boldsymbol{S}^q_-. \tag{2.7}$$

So for each $\boldsymbol{\xi}_\Gamma \in S$ we looking for $\boldsymbol{\xi}^+_\Gamma \in S^q_+$ and $\boldsymbol{\xi}^-_\Gamma \in S^q_-$ such that $\boldsymbol{\xi}_\Gamma = \boldsymbol{\xi}^+_\Gamma + \boldsymbol{\xi}^-_\Gamma$. Furthermore, we require that such a representation be unique. One implements it by a projection operator whose image is S^q_+ and it's kernel is S^q_-. We stress that while the space S doesn't change, the representation (2.7) changes for the exterior or interior problem, e.g. $S^1_+ \neq S^0_-$ in general. In addition, the choice of the projection operator affects the representation of (2.7), which can be considered as changing the projection angle onto the same subspace [39].

One defines such a projection operator using Calderon's potential (2.5). This projection is known as the Calderon's boundary projection. We will show that this projection implies a wave split, see discussion in Section 2.1.1. We first define the vector trace operator $\boldsymbol{Tr}\, v = \left(v, \frac{\partial v}{\partial \boldsymbol{n}}\right)\big|_\Gamma$. Thus, Calderon's boundary projection is defined as

$$\boldsymbol{P}^q_\Gamma \boldsymbol{\xi}_\Gamma = \boldsymbol{Tr}\, \boldsymbol{P}_{\Omega_q} \boldsymbol{\xi}_\Gamma. \tag{2.8}$$

Note, that any $\boldsymbol{\xi}_\Gamma$ satisfies $\boldsymbol{L}_q \boldsymbol{P}_{\Omega_q} \boldsymbol{\xi}_\Gamma = 0,\ \boldsymbol{x} \in \Omega_q$, and therefore Green's formula provides $\boldsymbol{P}_{\Omega_q} \boldsymbol{\xi}_\Gamma = \boldsymbol{P}_{\Omega_q} \boldsymbol{Tr}\, \boldsymbol{P}_{\Omega_q} \boldsymbol{\xi}_\Gamma$ which immediately implies that $\boldsymbol{P}^q_\Gamma$ is a projection since $(\boldsymbol{P}^q_\Gamma)^2 = \boldsymbol{P}^q_\Gamma$.

The operator $\boldsymbol{P}^q_\Gamma$ has an important property. If $\boldsymbol{\xi}_\Gamma$ defines $u(x) = \boldsymbol{P}_{\Omega_q} \boldsymbol{\xi}_\Gamma$ for which $\boldsymbol{Tr}\, u(x) = \boldsymbol{\xi}_\Gamma$, then the following equation holds

$$\boldsymbol{P}^q_\Gamma \boldsymbol{\xi}_\Gamma = \boldsymbol{\xi}_\Gamma. \tag{2.9}$$

If equation (2.9) holds, then $u(x) = \boldsymbol{P}_{\Omega_q} \boldsymbol{\xi}_\Gamma$ satisfies $\boldsymbol{L}_q u = 0$, and $\boldsymbol{Tr}\, u = \boldsymbol{\xi}_\Gamma$. Finally, we have proved that $\boldsymbol{\xi}_\Gamma$ satisfies the BEP if and only if $\boldsymbol{\xi}_\Gamma = \boldsymbol{Tr}\, u$ for which $\boldsymbol{L}_q\, u = 0$ [51, 53, 39]. We call equation (2.9) the boundary equation with projection (BEP).

2.1.1 Wave Split

The solutions to the homogeneous equation $\boldsymbol{L}_q u = 0$ can be interpreted as incoming waves for the domain Ω_q, because they have no (radiating) sources on Ω_q. In order to describe how Calderon's projection splits the waves [39], we first recast equation

(2.5) as:

$$\boldsymbol{P}_{\Omega_q}\boldsymbol{\xi}_\Gamma(\boldsymbol{x}) = \begin{cases} \sigma_q \int_\Gamma \left(\xi^I(\boldsymbol{y})\frac{\partial G_q}{\partial \boldsymbol{n}}(\boldsymbol{x}-\boldsymbol{y}) - \xi^{II}(\boldsymbol{y})G_q(\boldsymbol{x}-\boldsymbol{y})\right) ds_{\boldsymbol{y}}, & \boldsymbol{x}\in\Omega_q, \\ 0 & \boldsymbol{x}\in\mathbb{R}^n\setminus\Omega_q. \end{cases} \tag{2.10}$$

Next we define Green's operator on $\boldsymbol{L}_q$ as

$$\boldsymbol{G}_q F(\boldsymbol{x}) = \begin{cases} \int_{\Omega_q} G_q(\boldsymbol{x}-\boldsymbol{y})F(\boldsymbol{y})d\boldsymbol{y}, & \boldsymbol{x}\in\Omega_q, \\ 0 & \boldsymbol{x}\in\mathbb{R}^n\setminus\Omega_q. \end{cases} \tag{2.11}$$

Thus, one expresses the exterior solution as $u^0(\boldsymbol{x}) = \boldsymbol{P}_{\Omega_0}u^0_\Gamma(\boldsymbol{x})$ where

$$u^0_\Gamma = \boldsymbol{Tr}\, u^0 = \left(u^0, \frac{\partial u^0}{\partial \boldsymbol{n}}\right)\Big|_\Gamma,$$

and the interior solution as the $u^1(\boldsymbol{x}) + \boldsymbol{G}_1\, F(\boldsymbol{x}) = \boldsymbol{P}_{\Omega_1}u^1_\Gamma(\boldsymbol{x}) + \boldsymbol{G}_1\, F(\boldsymbol{x})$ where

$$u^1_\Gamma = \boldsymbol{Tr}\, u^1 = \left(u^1, \frac{\partial u^1}{\partial \boldsymbol{n}}\right)\Big|_\Gamma.$$

Hence, the solution to the problem (1.2) is given by

$$u(\boldsymbol{x}) = u^0(\boldsymbol{x}) + u^1(\boldsymbol{x}) + \boldsymbol{G}_1\, F(\boldsymbol{x}), \qquad \boldsymbol{x}\in\mathbb{R}^n. \tag{2.12}$$

We next denote $u_\Gamma = u^1_\Gamma + u^0_\Gamma$. Note, that in general u_Γ does not satisfy the BEP unless $u_\Gamma = u^q_\Gamma$. This means that the operator $\boldsymbol{P}^q_\Gamma\boldsymbol{\xi}_\Gamma$ eliminates that part of $\boldsymbol{\xi}_\Gamma$ which is not the trace of the solution of $\boldsymbol{L}_q u = 0$. In other words incoming waves to Ω_q, denoted as $\boldsymbol{\xi}^+_\Gamma$, belong to the image of the projection $\boldsymbol{P}^q_\Gamma$, i.e. $\boldsymbol{\xi}^+_\Gamma \in \mathrm{Im}\boldsymbol{P}^q_\Gamma$ while

outgoing waves to Ω_q satisfy $\boldsymbol{\xi}_\Gamma^- \in \mathrm{Ker}\boldsymbol{P}_\Gamma^q$. Therefore, the aforementioned space S satisfies $S = \mathrm{Im}\boldsymbol{P}_\Gamma^q \oplus \mathrm{Ker}\boldsymbol{P}_\Gamma^q$, since $S_+^j = \mathrm{Im}\boldsymbol{P}_\Gamma^q$ and $S_-^j = \mathrm{Ker}\boldsymbol{P}_\Gamma^q$.

The operators P_Γ^q are defined in such a way so that if there is no discontinuity, i.e. $k_0 = k_1$ then $\mathrm{Im}\boldsymbol{P}_\Gamma^1 = \mathrm{Ker}\boldsymbol{P}_\Gamma^0$ and $\mathrm{Ker}\boldsymbol{P}_\Gamma^1 = \mathrm{Im}\boldsymbol{P}_\Gamma^0$, and so there are no reflections at Γ. However, in general $\mathrm{Im}\boldsymbol{P}_\Gamma^1 \neq \mathrm{Ker}\boldsymbol{P}_\Gamma^0$ and $\mathrm{Ker}\boldsymbol{P}_\Gamma^1 \neq \mathrm{Im}\boldsymbol{P}_\Gamma^0$, which means that there is both propagation through and reflection from the interface Γ, similar to the 1D case, see Figure 2.1.

2.1.2 Reduction of the problem to the boundary

For an exterior domain Ω_0 the solution is $u = \tilde{u} + u^{(\mathrm{inc})}$ where $\tilde{u}$ denotes the scattered field satisfying the Sommerfeld radiation condition (1.3). Therefore, due to the linearity of the trace operator, the density $\boldsymbol{\xi}_\Gamma$ for the exterior domain is given by

$$\boldsymbol{\xi}_\Gamma = \boldsymbol{Tr}u = \boldsymbol{Tr}\tilde{u} + \boldsymbol{Tr}u^{(\mathrm{inc})} = \tilde{\boldsymbol{\xi}}_\Gamma + \boldsymbol{\xi}_\Gamma^{(\mathrm{inc})}.$$

To satisfy (1.3) one formulates the BEP for the exterior problem for the scattered field:

$$\boldsymbol{P}_\Gamma^0 \tilde{\boldsymbol{\xi}}_\Gamma = \tilde{\boldsymbol{\xi}}_\Gamma.$$

However, in order to match it to the interior part one complements it, for the total field, by adding $\boldsymbol{P}_\Gamma^0 \boldsymbol{\xi}_\Gamma^{(\mathrm{inc})} + \boldsymbol{\xi}_\Gamma^{(\mathrm{inc})}$ to both sides of the equation. Hence, assuming that the solution and its first normal derivative are continuous across Γ, we can equivalently reformulate problem (1.2) as the following system of BEP [53] defined on $\boldsymbol{\xi}_\Gamma$:

$$\begin{cases} \boldsymbol{P}_\Gamma^1 \boldsymbol{\xi}_\Gamma + \boldsymbol{Tr}\boldsymbol{G}_1 F & = \boldsymbol{\xi}_\Gamma, \\ \boldsymbol{P}_\Gamma^0 \boldsymbol{\xi}_\Gamma + (\boldsymbol{I} - \boldsymbol{P}_\Gamma^0)\boldsymbol{\xi}_\Gamma^{(\mathrm{inc})} & = \boldsymbol{\xi}_\Gamma. \end{cases} \tag{2.13}$$

System (2.13) can be thought of as a multi-dimensional analogue of system (2.3). Once (2.13) has been solved for ξ_Γ, the solution $u(x)$ is given by

$$u(\boldsymbol{x}) = \begin{cases} \boldsymbol{P}_{\Omega_1}\boldsymbol{\xi}_\Gamma(\boldsymbol{x}) + \boldsymbol{G}_1 F(\boldsymbol{x}) & \boldsymbol{x} \in \Omega_1, \\ \boldsymbol{P}_{\Omega_0}[\boldsymbol{\xi}_\Gamma - \boldsymbol{\xi}_\Gamma^{(\mathrm{inc})}](\boldsymbol{x}) + u^{(\mathrm{inc})}(\boldsymbol{x}) & \boldsymbol{x} \in \Omega_0. \end{cases} \tag{2.14}$$

Note that the application of the trace operator $\boldsymbol{Tr}$ reduces system (2.14) back to (2.13).

2.1.3 Divide and Conquer

One of the important generalizations of the proposed method is that one can redefine (2.13) in such a way so that it is possible to solve it as two separate auxiliary problems (AP) one for the interior and one for the exterior domain. Such an approach has several advantages. For example, one can solve each of the auxiliary problems on a different grid. Another example is that one can change the Sommerfeld approximation without recalculating the auxiliary problem for the interior area. However, the main advantage is the relatively simple treatment of curvilinear interfaces Γ as will be explained in the next section.

Consider an arbitrary function $w(\boldsymbol{x})$, $\boldsymbol{x} \in \mathbb{R}^n$, that satisfies the Sommerfeld radiation condition (1.3) and such that $\boldsymbol{Tr}w = \boldsymbol{\xi}_\Gamma = (\xi^I, \xi^{II})$. Generally $\boldsymbol{L}_q w \neq 0$,

$\boldsymbol{x} \in \Omega_q$, and therefore Green's formula gives:

$$w(\boldsymbol{x}) = \boldsymbol{P}_{\Omega_q} w_\Gamma + \boldsymbol{G}_q \boldsymbol{L}_q w, \quad \boldsymbol{x} \in \Omega_q.$$

Using the fact that $\boldsymbol{P}_{\Omega_q} w_\Gamma = \boldsymbol{P}_{\Omega_q} \boldsymbol{\xi}_\Gamma(\boldsymbol{x})$, we get

$$\boldsymbol{P}_{\Omega_q} \boldsymbol{\xi}_\Gamma(\boldsymbol{x}) = w(\boldsymbol{x}) - \boldsymbol{G}_q \boldsymbol{L}_q w, \quad \boldsymbol{x} \in \Omega_q. \tag{2.15}$$

We next generalize (2.15) in the following way: let $\boldsymbol{L}_q$ be defined for $\boldsymbol{x} \in \mathbb{R}^n$ (instead of $\boldsymbol{x} \in \Omega_q$). We reformulate $\boldsymbol{P}_{\Omega_q}$ so that the equation (2.5) becomes

$$\boldsymbol{P}_{\Omega_q} \boldsymbol{\xi}_\Gamma(\boldsymbol{x}) = w(\boldsymbol{x}) - \boldsymbol{G}_q \left\{ (\boldsymbol{L}_q w)\big|_{\Omega_q} \right\}, \quad \boldsymbol{x} \in \Omega_q. \tag{2.16}$$

The potential (2.16) is obtained on $\mathbb{R}^n$ and then restricted to Ω_q. Furthermore, it is insensitive to the choice of w as long as the conditions $\boldsymbol{Tr} w = \boldsymbol{\xi}_\Gamma$ and (1.3) hold. The projection $\boldsymbol{P}_\Gamma^q$ defined through (2.16) is the same as one defined through (2.5). The importance of this new definition is that it does not contain surface integrals.

This further generalization is the key feature in the treatment of generally shaped bodies that are not aligned to the numerical grid, which is discussed in Section 2.3. Let $\widetilde{\Omega}_q$ be a regularly shaped expanded domain such that $\Omega_q \subset \widetilde{\Omega}_q$. Assume that $\boldsymbol{L}_q$ is also defined on $\widetilde{\Omega}_q$, and that $\boldsymbol{G}_q$ is the corresponding inverse so that the solution u to the equation $\boldsymbol{L}_q u = F$ on $\widetilde{\Omega}_q$ is given by $u = \boldsymbol{G}_q F$. Hereafter, we assume that this solution exists for any given F defined on $\widetilde{\Omega}_q$ and is unique as along as u is required to satisfy some specially chosen boundary conditions at $\partial\widetilde{\Omega}_q$. The combination of the differential equation $\boldsymbol{L}_q u = F$ and these boundary conditions will be referred to

as the auxiliary problem (AP). The AP can be constructed so that it is easy to solve. In particular, the evaluation of $\boldsymbol{G}_q F$ does not need to involve any singular integrals. Instead, the AP is discretized, and its solution computed using finite differences on a regular grid (see Section 2.3). Finally, problem (1.2) is solved as two different BEPs defined on $\boldsymbol{\xi}_\Gamma$:

$$\begin{cases} \boldsymbol{P}_\Gamma^1 \boldsymbol{\xi}_\Gamma^1 + \boldsymbol{Tr}\boldsymbol{G}_1 F & = \boldsymbol{\xi}_\Gamma^1, \\ \boldsymbol{P}_\Gamma^0 \boldsymbol{\xi}_\Gamma^0 + (I - \boldsymbol{P}_\Gamma^0)\boldsymbol{\xi}_\Gamma^{(\mathrm{inc})} & = \boldsymbol{\xi}_\Gamma^0, \end{cases} \tag{2.17}$$

subject to the condition

$$\boldsymbol{A}\boldsymbol{\xi}_\Gamma^1 + \boldsymbol{B}\boldsymbol{\xi}_\Gamma^0 = \boldsymbol{0}, \tag{2.18}$$

which is an additional generalization to (2.13) where $\boldsymbol{A} = \boldsymbol{B} = 1$. This last generalization is the pathway for different interface conditions.

We denote $\boldsymbol{\xi}_\Gamma^q = (\xi_q^I, \xi_q^{II})$ where $q \in \{0, 1\}$ refers to the interior or exterior traces in (2.17). ξ_q^I, ξ_q^{II} are the solution and it's normal derivative on the interface Γ, and are therefore unknown. In order to solve system (2.17) one expands both $\boldsymbol{\xi}_\Gamma^1$, $\boldsymbol{\xi}_\Gamma^0$ in some basis, e.g. Fourier, so that the coefficients of the expansion become the unknowns of the problem. Once the coefficients are known and $\boldsymbol{\xi}_\Gamma^1$, $\boldsymbol{\xi}_\Gamma^0$ assembled, the solution is computed by (2.14). We describe this approach in more detail and provide examples in Section 2.3.

2.1.4 Boundary conditions

When one solves only the exterior or interior part of (2.17) the interface condition on Γ becomes a boundary condition $\boldsymbol{l}_\Gamma u = \phi$. One recasts it as

$$\boldsymbol{l}_\Gamma(\boldsymbol{P}_{\Omega_1}\boldsymbol{\xi}^1_\Gamma + \boldsymbol{G}_1 F) = \phi \tag{2.19}$$

for an interior problem. The system of equations (2.17), (2.19) is then solved with respect to $\boldsymbol{\xi}^1_\Gamma$.

For an exterior problem it becomes

$$\boldsymbol{l}_\Gamma(\boldsymbol{P}_{\Omega_0}\tilde{\boldsymbol{\xi}}^0_\Gamma + u^{(\mathrm{inc})}) = \phi \tag{2.20}$$

and the system of equations (2.17), (2.20) is to be solved with respect to $\tilde{\boldsymbol{\xi}}^0_\Gamma$.

The operator $\boldsymbol{l}_\Gamma$ that defines the boundary condition in the problem can be arbitrary, ranging from very simple (e.g., Dirichlet or Neumann) to very general (e.g., different type on different parts of Γ, nonlocal, etc.). Systems (2.17), (2.19) or (2.17), (2.20) are still equivalent to the relevant interior or exterior problem.

In practice, Calderon's potentials and projections are approximated by difference potentials and projections, respectively, see [53]. In doing so, the discrete counterparts of formula (2.16) are developed and used, so that one never needs to approximate singular surface integrals. Instead, one needs to solve a discrete auxiliary problem that can be chosen convenient for a numerical solution.

2.2 Well-posedness

We assume that the original problem (1.2) is well-posed, i.e., that its solution exists, is unique, and depends continuously on the data $F(\boldsymbol{x})$, ϕ, in the sense of appropriately chosen norms. Then, the equivalent problem on the interface (2.17), (2.18) or on the boundary (2.17), (2.19) or (2.17), (2.20) is also well-posed. This means that if the BEP is perturbed, then the solution of the boundary system will also get perturbed, and the perturbation of the solution will be bounded in the appropriate norm by the perturbation introduced into the BEP.

For instance, consider the interior homogeneous case:

$$\boldsymbol{L}u = 0 \text{ on } \Omega \quad \text{and} \quad \boldsymbol{l}_\Gamma u = \phi \text{ on } \Gamma,$$

for which the equivalent boundary formulation is

$$\boldsymbol{P}_\Gamma \boldsymbol{\xi}_\Gamma - \boldsymbol{\xi}_\Gamma = \boldsymbol{0} \quad \text{and} \quad \boldsymbol{l}_\Gamma(\boldsymbol{P}_\Omega \boldsymbol{\xi}_\Gamma) = \phi.$$

If the original problem is well-posed, then $\|u\| \leqslant c\|\phi\|$, and consequently,

$$\|\boldsymbol{\xi}_\Gamma\| \leqslant c_1\|\phi\|.$$

This result has nothing to do with Calderon's operators per se, it holds simply because $\boldsymbol{\xi}_\Gamma = \boldsymbol{T}\boldsymbol{r}u$. Let $\boldsymbol{\psi}_\Gamma$ be a perturbation, so that instead of the true unperturbed boundary problem we are solving

$$\boldsymbol{P}_\Gamma \boldsymbol{\xi}_\Gamma - \boldsymbol{\xi}_\Gamma = \boldsymbol{\psi}_\Gamma \quad \text{and} \quad \boldsymbol{l}_\Gamma(\boldsymbol{P}_\Omega \boldsymbol{\xi}_\Gamma) = \phi.$$

Then, we have

$$\|\boldsymbol{\xi}_\Gamma\| \leqslant C(\|\phi\| + \|\boldsymbol{\psi}_\Gamma\|),$$

where the constant C depends on $\|\boldsymbol{P}_\Omega\|$ and $\|\boldsymbol{P}_\Gamma\|$, but does not depend on either ϕ or $\boldsymbol{\psi}_\Gamma$. The proof can be found in [52, Part II, Chapter 1]. It is based on splitting the entire space of traces $\boldsymbol{\xi}_\Gamma$ on Γ into the direct sum: $\mathrm{Im}\boldsymbol{P}_\Gamma^j \oplus \mathrm{Ker}\boldsymbol{P}_\Gamma^j$ as discussed above.

2.3 Discrete Calderon's Potentials

We now develop the discrete counterpart of the theory introduced in the previous section. To make the presentation easier we first describe it in relatively simple algorithmic terms in Section 2.3.1 followed by several representative problems and their solution supported by BEP theory in mathematical and algorithmic terms in following sections. We stress, despite the fact that we only provide examples with simple regular shapes, the theory remains unchanged for a generally shaped body.

2.3.1 Algorithm

In this section we present a sequence of simple algorithmic steps that implements the solution of problem (1.2).

Thus, we provide pseudocode of the main procedures required to implement our method and give several algorithms for solving the problem in a domain not aligned to the grid including the transmission-reflection algorithm in heterogeneous media with a jump at the interface and an efficient algorithm for multiple impinging waves.

The main advantage of our method is that for each sub-domain Ω_q, see (1.2), we compute a relatively small set of individual solutions to a simple auxiliary problem on a regular domain formulated to be numerically effective. Individual solutions are used to assemble the solution of the original problem.

More precisely, we solve the system of BEPs (2.17), (2.18) as follows. For each BEP, exterior ($q = 0$) or interior ($q = 1$) we consider an expansion of $\boldsymbol{\xi}_\Gamma^q = (\xi_q^I, \xi_q^{II})$ in some basis on Γ, e.g. Fourier:

$$\xi_q^I(s) = \sum c_n^{I,q} b_n(s), \tag{2.21a}$$

and

$$\xi_q^{II}(s) = \sum c_n^{II,q} b_n(s), \tag{2.21b}$$

so that the problem is reduced to finding the coefficients $c_n^{I,q}$, $c_n^{II,q}$ that satisfy the condition

$$\boldsymbol{A}\left(\sum c_n^{I,0} b_n(s), \sum c_n^{II,0} b_n(s)\right) + \boldsymbol{B}\left(\sum c_n^{I,1} b_n(s), \sum c_n^{II,1} b_n(s)\right) = \boldsymbol{0} \tag{2.22}$$

obtained by substituting expressions (2.21) into formula (2.18). Each individual solution corresponds to a basis function chosen on Γ and extended to it's grid representation γ by means of the operator $\mathcal{T}$ to be defined in Section 2.3.1.2.

In the following sections we define γ, then describe the extension of basis function, and then describe and provide pseudocode of the discrete counterpart of Calderon's potentials theory followed by examples of solutions to several problems.

2.3.1.1 The grid representation of the boundary shape

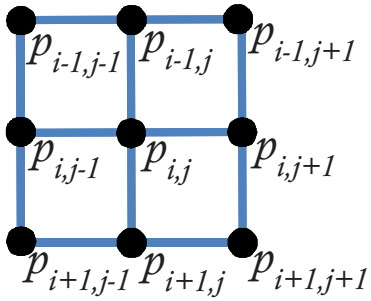

Figure 2.2: 9-point stencil centered at node $p_{i,j}$

We define now the grid representation of the curve Γ, which we denote γ, in a following way. Let Ω be a smooth body in the domain represented by regular grid $\mathbb{N}$, e.g. Cartesian. Since Ω_q is not necessary aligned to the grid, the intersections between $\mathbb{N}$ and Γ may be an empty set, therefore we define γ to be a set of grid points surrounding Γ. Formally, let $\mathbb{N}_{p_{i,j}}$ be the stencil centered at node $p_{i,j}$, e.g. the 9-point stencil on Figure 2.2 and let $\mathbb{N}^+, \mathbb{N}^-$ be non-empty sets defined as

$$\mathbb{N}^+ = \bigcup_{p_{i,j} \in \Omega_q} \mathbb{N}_{p_{i,j}}, \qquad \mathbb{N}^- = \bigcup_{p_{i,j} \in \mathbb{N} \setminus \Omega_q} \mathbb{N}_{p_{i,j}},$$

where $q \in \{0, 1\}$. Then the grid representation of the curve Γ, γ, is given as

$$\gamma = \mathbb{N}^+ \cap \mathbb{N}^-. \tag{2.23}$$

An example of γ for general body in Cartesian coordinates is shown in Figure 2.3. In Figure 2.4 we present γ for a similar general body in polar coordinates.

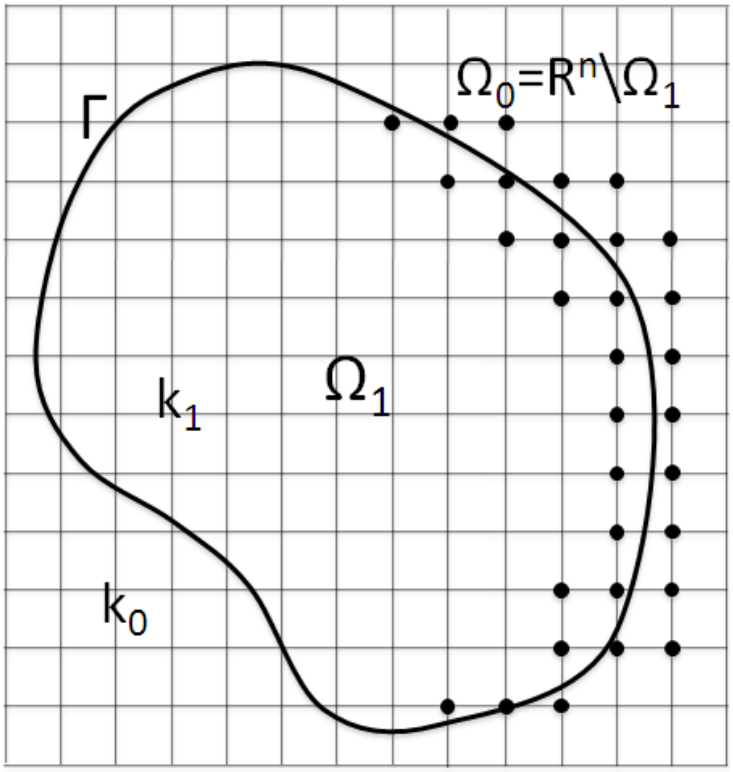

Figure 2.3: Example of γ: general body in Cartesian coordinates.

2.3.1.2 Extension of the basis function

We next define a new scalar function $\boldsymbol{\xi}_\gamma^q$ in the vicinity of Γ which represents the numerical counterpart of the trace of the solution $\boldsymbol{\xi}_\Gamma^q$. $\boldsymbol{\xi}_\gamma^q$ is obtained by extension of $\boldsymbol{\xi}_\Gamma^q$ from Γ to γ using Equation-Based extension. The idea behind Equation-Based extension is similar to the approach used to construct compact schemes (see Section 1.2.1). Given the function and the first normal derivative contained in $\boldsymbol{\xi}_\Gamma^q$, one differentiates the Helmholtz equation $\boldsymbol{L}_q\, u = F$ to obtain higher order normal derivatives and uses these to build a Taylor formula (2.24) that yields the value of

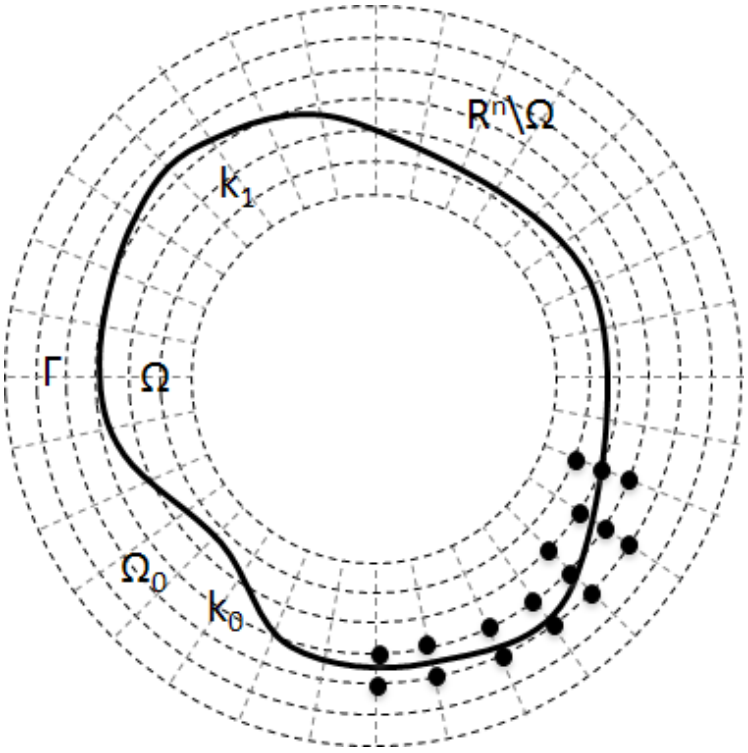

Figure 2.4: Example of γ: general body in polar coordinates.

$\boldsymbol{\xi}_\gamma^q$ at every node γ.

$$v(n+\delta n, s) = v(n,s) + \sum_{t=1}^{\mathfrak{N}} \frac{1}{t!} \frac{\partial^t v(n,s)}{\partial n^t} \delta n^t \tag{2.24}$$

We denote the Equation-Based Taylor extension as $\boldsymbol{\xi}_\gamma^q = \mathcal{T}(\xi_q^I, \xi_q^{II}, F|_\Gamma)$ where F is the source term of the equation. An example of Equation-Based Taylor extension in polar coordinates can be found in Section 2.3.2 and in Section 2.3.5 we show the extension in elliptic coordinates. The general case is analyzed in [42].

The extension $\mathcal{T}$ applies to any boundary vector function $\boldsymbol{\xi}_\Gamma = (\xi_q^I, \xi_q^{II})$, and

defines a new scalar function in the vicinity of Γ that we need to evaluate at the nodes γ. The operator $\mathcal{T}(\cdot,\cdot,0)$ is linear. If it happens that $\xi_q^I = u|_\Gamma$ and $\xi_q^{II} = \frac{\partial u}{\partial n}\big|_\Gamma$, where u is a solution to the Helmholtz equation $\boldsymbol{L}_q\, u = F$ on Ω_q, then $\mathcal{T}(\xi_q^I, \xi_q^{II}, F|_\Gamma)$ approximates u at the nodes γ with the accuracy determined by the order of the Taylor formula (2.24).

The number of terms in the Taylor formula (2.24) should be taken as the minimum that would guarantee the design rate of grid convergence of the overall algorithm, see page 62 and Section Section 3.1.1. Increasing the number of terms beyond that minimum will not speed up the convergence any further, as its rate is limited by the order of accuracy of the scheme. Therefore, in practice the order of the Taylor formula (2.24) is always kept fixed. In theory, however, this order can be allowed to increase. Then, by invoking a Cauchy-Kowalevski type argument, we can conclude that the series will converge at the points sufficiently close to the boundary as long as all the data are analytic. Among other classes of equations, this result holds for elliptic PDEs, which is our case.

Due to the linearity of the extension $\mathcal{T}$ one extends the basis functions $b_n(s)$ in expansion (2.21). For an interior subproblem we define $\xi_{\gamma,1}^I(n) = \mathcal{T}(b_n, 0, 0)$, $\xi_{\gamma,1}^{II}(n) = \mathcal{T}(0, b_n, 0)$, and $\xi_{\gamma,1}^F = \mathcal{T}(0, 0, F|_\Gamma)$, where the latter is used for computational efficiency, otherwise the contribution of the source term is unnecessarily calculated several times. Thus we get

$$\xi_{\gamma,1}^I = \sum c_n^{I,1} \xi_{\gamma,1}^I(n) \tag{2.25a}$$

and

$$\xi^{II}_{\gamma,1} = \sum c^{II,1}_n \xi^{II}_{\gamma,1}(n), \tag{2.25b}$$

and we define

$$\boldsymbol{\xi}^1_\gamma = \xi^I_{\gamma,1} + \xi^{II}_{\gamma,1} + \xi^F_{\gamma,1}. \tag{2.26}$$

For an exterior (homogeneous) subproblem we define $\xi^I_{\gamma,0}(n) = \mathcal{T}(b_n, 0, 0)$ and $\xi^{II}_{\gamma,0}(n) = \mathcal{T}(0, b_n, 0)$, thus

$$\xi^I_{\gamma,0} = \sum c^{I,0}_n \xi^I_{\gamma,0}(n) \tag{2.27a}$$

and

$$\xi^{II}_{\gamma,0} = \sum c^{II,0}_n \xi^{II}_{\gamma,0}(n), \tag{2.27b}$$

and we define

$$\boldsymbol{\xi}^0_\gamma = \xi^I_{\gamma,0} + \xi^{II}_{\gamma,0}. \tag{2.28}$$

Theoretically, to reach n^{th} order of accuracy for the overall solution to the problem one requires $\mathfrak{N} = n + 2$, see [47]. However the experimental results presented in Section 3.1.1 and in [42] show that it is sufficient to take $\mathfrak{N} = n$.

We should also mention that according to [28, 27, 59], for maintaining the overall given order of accuracy across the domain, it may be sufficient to approximate the boundary conditions with lower accuracy. In the future, it may be of interest to investigate whether this phenomenon is related to our finding that the order of the extension operator can be taken lower than theoretically predicted.

2.3.1.3 Difference Potentials

In section Section 2.1.3 we required an arbitrary function $w(\boldsymbol{x})$, $\boldsymbol{x} \in \mathbb{R}^n$, that satisfies the Sommerfeld radiation condition (1.3) and such that it's vector trace is equal $\boldsymbol{\xi}_\Gamma$, i.e. $\boldsymbol{Tr}w = (w, w_n) = (\xi^I, \xi^{II}) = \boldsymbol{\xi}_\Gamma$ where w_n is the normal derivative of w along Γ. We denote the discrete trace operator similarly as the continuous one, i.e. $\boldsymbol{Tr}$. In the discrete case the trace operator become the value of the function at the grid boundary γ, i.e. $\boldsymbol{Tr}w = w|_\gamma$. Thus, we require the discrete w to satisfy $\boldsymbol{Tr}w = \boldsymbol{\xi}_\gamma$, where $\boldsymbol{\xi}_\gamma$ defined in Section 2.3.1.2.

Numerically one creates $w(\boldsymbol{x})$ using the same structure and the same size as the solution to the problem. One fills $w(\boldsymbol{x})$ with values of ξ_γ at nodes corresponding to γ and zeroes elsewhere. We present such a procedure in Algorithm 1:

Algorithm 1 Create w from ξ_γ

```
function W(ξ_γ)
    w ← 0 on grid ℕ
    w|_γ ← ξ_γ
    return w
end function
```

Let $\mathcal{S}(\mathbb{N}, k, F, \tilde{g})$ be a solver of the equation (1.1) on some regular grid $\mathbb{N}$ subject to the numerical boundary condition $u|_{\partial\mathbb{N}} = \tilde{g}$, where $\partial\mathbb{N}$ is the informal notation for boundary nodes of $\mathbb{N}$. We seek to solve the same AP with different source terms. Therefore, we choose a fixed $\tilde{g}$ to provide uniqueness and redefine the solver as $\mathcal{S}(\mathbb{N}, k, F)$. Let n be the order of accuracy of $\mathcal{S}$. One can use the solver described in Section 1.2.1 or as described in more detail in [65, 42, 10, 55, 41]. We denote by S the solver for either the exterior or interior problem.

We next define, in Algorithm 2, the discrete counterpart of Calderon's potential

P_{Ω_q} which, unlike in continues case, will take as input $w(\boldsymbol{x})$ instead of ξ_γ (see Section 2.1.3) and assume that $\boldsymbol{Tr}w = \boldsymbol{\xi}_\gamma$ or similarly $w(\boldsymbol{x})|_\gamma = \xi_\gamma$, i.e. here we consider $w(\boldsymbol{x})$ is known:

Algorithm 2 Calderon Potential $P_{\Omega_q}\xi_\gamma$

function $P_{\Omega_q}(\mathbb{N},k,w)$ ▷ Assuming $\boldsymbol{Tr}w = \boldsymbol{\xi}_\gamma$
  $rhs \leftarrow 0$ on grid $\mathbb{N}$
  $rhs|_{\Omega_q} \leftarrow (\boldsymbol{L}_q\, w)|_{\Omega_q}$ ▷ set an artificial rhs
  $v \leftarrow S(\mathbb{N}, k, rhs)$
  return $w - v$ ▷ return potential, see sections 2.1,2.3
end function

$(\boldsymbol{L}_q\, w)|_{\Omega_q}$ is the result of the direct Helmholtz operator $\boldsymbol{L}_q$ on the entire grid $\mathbb{N}$ and truncated to the domain of interest Ω_q.

One defines Calderon Potential in the following way. Let $u(s) = h(s)$ and $\frac{\partial u}{\partial \boldsymbol{n}}(s) = g(s)$ therefore:

Algorithm 3 Another definition of Calderon Potential

function $\tilde{P}_{\Omega_q}(\mathbb{N},k,h,g,F)$
  $\xi_\gamma \leftarrow \mathcal{T}(h, g, F)$
  $w \leftarrow \mathcal{W}(\xi_\gamma)$
  return $P_{\Omega_q}(\mathbb{N}, k, w)$
end function

The difference between Algorithm 2 and Algorithm 3 is that the latter creates w from u and $\frac{\partial u}{\partial \boldsymbol{n}}$ using an extension $\mathcal{T}$ while the former gets w as an argument. Algorithm 2 can be used more effectively for multiple values of w, therefore Algorithm 3 is not used in further algorithms and presented here for didactic purpose only.

We now define the projection operator, which numerically become a truncation of the Calderon operator in Algorithm 4.

Algorithm 4 Projection operator

function $P^q_\gamma(\mathbb{N},k,\xi_\gamma)$
  $w \leftarrow \mathcal{W}(\xi_\gamma)$
  return $P_{\Omega_q}(\mathbb{N},k,w)|_\gamma$
end function

2.3.1.4 Examples of solutions to different problems

We next solve the homogeneous problem $\boldsymbol{L}_q u + k_q^2 u = 0$ in a domain Ω_q (either interior or exterior) and let the boundary condition *bc* of type *bc_type* be given on $\partial\Omega_q$. We assume that the solution has an expansion in some functional basis, e.g. Fourier, $u(s) = \sum_n c_n^1 b_n(s)$ and $\frac{\partial u}{\partial \boldsymbol{n}}(s) = \sum_n c_n^2 b_n(s)$ and get

Algorithm 5 The Solver for a homogeneous problem

function HOMOGENEOUS-SOLVER$_{\Omega_q}$($\mathbb{N}$,*k*,*bc_type*,*bc*)
  $(\xi_\gamma^I, Q_I, \xi_\gamma^{II}, Q_{II}) \leftarrow \text{BEP}_q(\mathbb{N},k)$ ▷ See Algorithm 6
  $(c^I, c^{II}) \leftarrow \text{Coefficients}(Q_I, Q_{II}, bc\_type, bc, 0)$ ▷ See Algorithm 7
  $u \leftarrow 0$ on grid $\mathbb{N}$
  $u|_{\Omega_q} \leftarrow (\mathcal{S}^q(\mathbb{N},k,\xi_\gamma^I c^I + \xi_\gamma^{II} c^{II}))|_{\Omega_q}$
  return u
end function

Algorithm 6 used in Algorithm 5 plays the discrete counterpart of (2.9) which one recasts as $\boldsymbol{P}^q_\gamma \boldsymbol{\xi}_\gamma = \boldsymbol{\xi}_\gamma$. The algorithm Algorithm 6 doesn't provide the solution to BEP, but the matrix with columns of $(P^q_\gamma - I)\xi_\gamma(n)$ where $\xi_\gamma(n)$ denotes nth basis function extended to the γ, see Section 2.3.1.2. This matrix is used to construct the linear system which is solved to find the coefficients of the expansion (2.21).

Algorithm 6 BEP

function BEP$_q$($\mathbb{N}$,k) ▷ Calculate operator $(P_\gamma^q - I)\xi_\gamma$
  foreach Basis Functions b_n
    $\xi_\gamma^I(n) \leftarrow \mathcal{T}(b_n, 0, 0)$ ▷ set ξ_γ's as columns of matrices $\xi_\gamma^I, \xi_\gamma^{II}$
    $\xi_\gamma^{II}(n) \leftarrow \mathcal{T}(0, b_n, 0)$
    $P_I(n) \leftarrow P_\gamma^q(\mathbb{N}, k, \xi_\gamma^I(n))$ ▷ solutions to AP's are columns of P_I, P_{II}
    $P_{II}(n) \leftarrow P_\gamma^q(\mathbb{N}, k, \xi_\gamma^{II}(n))$
  end foreach
  $Q_I \leftarrow P_I - \xi_\gamma^I$
  $Q_{II} \leftarrow P_{II} - \xi_\gamma^{II}$
  return $(\xi_\gamma^I, Q_I, \xi_\gamma^{II}, Q_{II})$
end function

The coefficients are actually found using Algorithm 7 in the least square sense using QR, since the linear system is redundant for sufficiently fine grid. It is solved by least squares via QR. See [42] and following examples.

Algorithm 7 Compute coefficients of an expansion on an interface

function COEFFICIENTS(Q_I,Q_{II},*bc_type*,*bc*,*InHomoPart*)
  $c \leftarrow$ CoeffsOf(*bc*) ▷ coefficients of $bc = \sum_n c_n b_n$
  switch *bc_type*
    case Dirichlet ▷ $u|_\gamma = bc$
      $\boldsymbol{c}^I \leftarrow c$
      $\boldsymbol{c}^{II} \leftarrow \mathbf{QR}(Q_{II},\ -Q_I\, c_I - InHomoPart)$
    case Neumann ▷ $u_n|_\gamma = bc$
      $\boldsymbol{c}^{II} \leftarrow c$
      $\boldsymbol{c}^I \leftarrow \mathbf{QR}(Q_I,\ -Q_{II}\, c_{II} - InHomoPart)$
    case Robin ▷ $(\alpha u + \beta u_n)|_\gamma = bc$
      $\boldsymbol{c}^I \leftarrow \mathbf{QR}(Q_I - \frac{\alpha}{\beta}\boldsymbol{Q}_{II},\ -\boldsymbol{Q}_{II}\, c - InHomoPart)$
      $\boldsymbol{c}^{II} \leftarrow \frac{1}{\beta}\hat{g} - \frac{\alpha}{\beta}\boldsymbol{c}^I$
  end switch
  return (c^I, c^{II})
end function

We next solve the inhomogeneous problem in Algorithm 8. A distinctive feature of compact schemes is that the right-hand side of the difference equation gets transformed, see (1.8), we denote this transformation as $\boldsymbol{B}(F)$. However the transforma-

tion of the source term requires F to be defined not only on Ω_q where it is originally defined in the analytical problem, but also on γ. Therefore, we continue F from Ω_q to $\Omega_q \cup \gamma$ using the Taylor extension $\mathcal{T}(F)$.

Algorithm 8 The Solver for an inhomogeneous problem

function INHOMOGENEOUS-SOLVER$_{\Omega_q}$($\mathbb{N}$,k,*bc_type*,*bc*)
  $(\xi_\gamma^I, Q_I, \xi_\gamma^{II}, Q_{II}) \leftarrow \mathrm{BEP}_q(\mathbb{N}, k)$
  $\xi_\gamma^F \leftarrow Ex(0, 0, F)$ ▷ calculate inhomogeneous part of Ex only once
  $P_F \leftarrow P_\gamma^q(\mathbb{N}, k, \xi_\gamma^F)$ ▷ which give another AP to solve
  $Q_F \leftarrow P_F - \xi_\gamma^F$
  $GF = S(\mathbb{N}, k, \boldsymbol{B}(\mathcal{T}(F)))$
  $(c^I, c^{II}) \leftarrow \mathrm{Coefficients}(Q_I, Q_{II}, bc\_type, bc, Q_F + GF|_\gamma)$
  $u \leftarrow 0$ on grid $\mathbb{N}$
  $u|_{\Omega_q} \leftarrow \mathcal{S}^q(\mathbb{N}, k, \xi_\gamma^I c^I + \xi_\gamma^{II} c^{II} + \xi_\gamma^F)|_{\Omega_q}$
  return $u + GF$
end function

We finally solve the transmission-reflection problem driven by the incident wave $u^{(\mathrm{inc})}$ in Algorithm 9. The media of the interior part can be heterogeneous. The exterior problem is considered in the far field and therefore the media is homogeneous. However, a jump is allowed at the interface between the interior and exterior problem. The solution to the exterior problem is considered as a sum of the scattered and incident field.

A clear advantage of our method is that scattering about a given shape but for multiple angles of incidence, and even for different boundary conditions, can be computed very efficiently. This is particularly important if the direct scattering problem needs to be solved many times while using an iterative method to solve an inverse scattering problem.

Algorithm 9 The Solver for Transmission-Reflection problem

function TRANSMISSION-REFLECTION-SOLVER($\mathbb{N}$,k_0,k_1,*bc_type*,$u^{(\text{inc})}$)
$(\xi_\gamma^{1,I}, Q_{1,I}, \xi_\gamma^{1,II}, Q_{1,II}) \leftarrow \text{BEP}_1(\mathbb{N}_1, k_1)$ ▷ Interior
$(\xi_\gamma^{0,I}, Q_{0,I}, \xi_\gamma^{0,II}, Q_{0,II}) \leftarrow \text{BEP}_0(\mathbb{N}_0, k_0)$ ▷ Exterior
$\xi_\gamma^1 \leftarrow \begin{pmatrix} \xi_\gamma^{1,I}, & \xi_\gamma^{1,II} \end{pmatrix}^T$
$\xi_\gamma^0 \leftarrow \begin{pmatrix} \xi_\gamma^{0,I}, & \xi_\gamma^{0,II} \end{pmatrix}^T$
$\xi_\gamma^{1,F} \leftarrow Ex(0,0,F)$
$Q_{1,F} \leftarrow P_\gamma^1(\mathbb{N}_1, k_1, \xi_\gamma^{1,F}) - \xi_\gamma^{1,F}$
$Q_{0,(\text{inc})} \leftarrow P_\gamma^0(\mathbb{N}_0, k_0, u^{(\text{inc})}|_\gamma) - u^{(\text{inc})}|_\gamma$
$GF_1 = S^1(\mathbb{N}_1, k_1, \boldsymbol{B}(\mathcal{T}(F)))$
$c = \mathbf{QR}\left(\begin{pmatrix} Q_{0,I}, & Q_{0,II} \\ Q_{1,I}, & Q_{1,II} \end{pmatrix}, \begin{pmatrix} -Q_{0,(\text{inc})} \\ -GF_1|_\gamma - Q_{1,F} \end{pmatrix}\right)$
$u \leftarrow 0$ on entire grid $\mathbb{N}_0 \cup \mathbb{N}_1$
$u|_{\Omega_0} \leftarrow \mathcal{S}^0(\mathbb{N}_0, k_0, \xi_\gamma^0 c)|_{\Omega_0} + u^{(\text{inc})}|_{\Omega_0}$
$u|_{\Omega_1} \leftarrow \mathcal{S}^1(\mathbb{N}_1, k_1, \xi_\gamma^1 c + \xi_\gamma^{1,F})|_{\Omega_1} + GF_1$
return u
end function

Consider a set of incident waves $u^{(\text{inc})}(\theta_m)$, The naive algorithm uses Algorithm 9 m times.

Algorithm 10 Inefficient Solver for Transmission-Reflection problem with multiple incident angles

function TRANSMISSION-REFLECTION-SOLVER-MA($\mathbb{N}$,k_0,k_1,*bc_type*,$u^{(\text{inc})}$,θ)
foreach Incident Angle θ_m
$U_m \leftarrow Transmission - Reflection - Solver(\mathbb{N}, k, bc\_type, u_m^{(\text{inc})})$
end foreach
return U
end function

However, it can be done much more efficiently, since the call to the most time expensive function BEP does not depend on the impinging wave and therefore can be called once per problem (Interior, Exterior) regardless of the number of incident angles used:

Algorithm 11 Efficient Solver for Transmission-Reflection problem with multiple incident angles

function TRANSMISSION-REFLECTION-SOLVER-MA($\mathbb{N}$,k_0,k_1,*bc_type*,$u^{(\text{inc})}$,θ)
  $(\xi_\gamma^{1,I}, Q_{1,I}, \xi_\gamma^{1,II}, Q_{1,II}) \leftarrow \text{BEP}_1(\mathbb{N}_1, k_1)$ ▷ Interior
  $(\xi_\gamma^{0,I}, Q_{0,I}, \xi_\gamma^{0,II}, Q_{0,II}) \leftarrow \text{BEP}_0(\mathbb{N}_0, k_0)$ ▷ Exterior
  $\xi_\gamma^1 \leftarrow \begin{pmatrix} \xi_\gamma^{1,I}, & \xi_\gamma^{1,II} \end{pmatrix}^T$
  $\xi_\gamma^0 \leftarrow \begin{pmatrix} \xi_\gamma^{0,I}, & \xi_\gamma^{0,II} \end{pmatrix}^T$
  $\xi_\gamma^{1,F} \leftarrow Ex(0,0,F)$
  $Q_{1,F} \leftarrow P_\gamma^1(\mathbb{N}_1, k_1, \xi_\gamma^{1,F}) - \xi_\gamma^{1,F}$
  $GF_1 = S^1(\mathbb{N}_1, k_1, \boldsymbol{B}(\mathcal{T}(F)))$
  foreach Incident Angle θ_m
    $Q_{0,(\text{inc})} \leftarrow P_\gamma^0(\mathbb{N}_0, k_0, u_m^{(\text{inc})}|_\gamma) - u_m^{(\text{inc})}|_\gamma$
    $c = \mathbf{QR}\left(\begin{pmatrix} Q_{0,I}, & Q_{0,II} \\ Q_{1,I}, & Q_{1,II} \end{pmatrix}, \begin{pmatrix} -Q_{0,(\text{inc})} \\ -GF_1|_\gamma - Q_{1,F} \end{pmatrix}\right)$
    $u \leftarrow 0$ on entire grid $\mathbb{N}_0 \cup \mathbb{N}_1$
    $u|_{\Omega_0} \leftarrow \mathcal{S}^0(\mathbb{N}_0, k_0, \xi_\gamma^0 c)|_{\Omega_0} + u_m^{(\text{inc})}|_{\Omega_0}$
    $u|_{\Omega_1} \leftarrow \mathcal{S}^1(\mathbb{N}_1, k_1, \xi_\gamma^1 c + \xi_\gamma^{1,F})|_{\Omega_1} + GF_1$
    $U_m \leftarrow u$
  end foreach
  return U
end function

2.3.2 Cartesian Coordinates: Homogeneous Dirichlet Problem in a Circle

Consider the Dirichlet problem (2.29) in a circular domain $\Omega_1 = \{(x,y)|\sqrt{x^2+y^2} < R\}$ solved on a Cartesian grid, where the boundary is not aligned to the grid.

$$\begin{cases} \Delta u + k^2 u = 0 & x^2 + y^2 < R^2, \\ u(x,y) = g(x,y) & x^2 + y^2 = R^2. \end{cases} \tag{2.29}$$

We introduce a finite-difference approximation to this problem. Let $\mathbb{N}$ be the Cartesian grid on the $(-x_t, x_t)\times(-y_t, y_t)$, where $x_t = y_t > R$ and let $p_{i,j} = (x_i, y_j) \in$

$\mathbb{N}$ be the nodes of the grid with $|p_{i,j}| = \sqrt{x_i^2 + y_j^2}$. Denote $\mathbb{M} = \{p_{i,j} : |p_{i,j}| < R\}$.

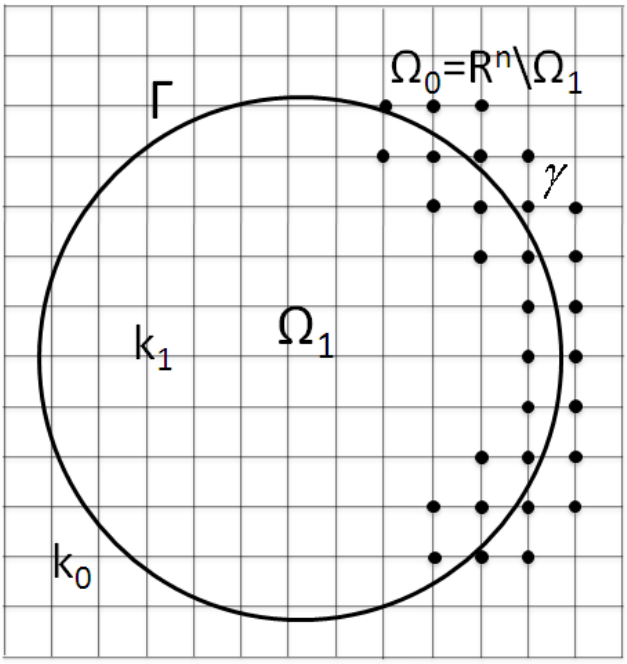

Figure 2.5: Circular body in Cartesian coordinates with γ defined in (2.23).

To solve problem (2.29) with higher order accuracy we first define the grid counterpart of original boundary shape Γ whose fragment and approximation are shown in Figure 2.5 as

$$\gamma = \mathbb{N}^+ \cap \mathbb{N}^-, \tag{2.30}$$

where $\mathbb{N}_{p_{i,j}}$ is the 9-point stencil centered at node $p_{i,j}$, see Figure 2.2. $\mathbb{N}^+, \mathbb{N}^-$ are non-empty sets defined as

$$\mathbb{N}^+ = \bigcup_{p_{i,j} \in \mathbb{M}} \mathbb{N}_{p_{i,j}}, \qquad \mathbb{N}^- = \bigcup_{p_{i,j} \in \mathbb{N} \setminus \mathbb{M}} \mathbb{N}_{p_{i,j}}.$$

2.3.2.1 Equation Based Extension

The set γ introduced by formula (2.23) will be used to define the density $\boldsymbol{\xi}_\gamma$ of a difference potential. In turn, $\boldsymbol{\xi}_\gamma$ will be obtained from $\boldsymbol{\xi}_\Gamma$ by means of the Equation-Based Taylor extension as explained in Section 2.3.1.2. We present an example of a 5^{th} order Equation-Based Taylor extension (2.31). Since the boundary shape is a circle it is convenient to rewrite the boundary condition as $u(R,\theta) = g(\theta)$. Although we solve the homogeneous problem, the extension is for a more general inhomogeneous case of an equation based extension.

$$u\left(R+\delta r,\theta\right) = u(R,\theta) + \delta r u_r + \frac{\delta r^2}{2}u_{rr} + \frac{\delta r^3}{6}u_{rrr} + \frac{\delta r^4}{24}u_{rrrr}. \tag{2.31}$$

We use Helmholtz equation in polar coordinates

$$u_{rr} + \frac{1}{r}u_r + \frac{1}{r^2}u_{\theta\theta} + k^2(r,\theta)u = F(r,\theta) \tag{2.32}$$

and solve (2.32) for the second radial derivative

$$u_{rr} = F - \frac{1}{r}u_r - \frac{1}{r^2}u_{\theta\theta} - k^2 u.$$

We differentiate it twice, for the third derivative

$$u_{rrr} = F_r + \frac{1}{r^2}u_r - \frac{1}{r}u_{rr} + \frac{2}{r^3}u_{\theta\theta} - \frac{1}{r^2}u_{r\theta\theta} - k^2 u_r - 2kk_r u,$$

and the fourth derivative

$$\begin{aligned} u_{rrrr} &= F_{rr} + \left(\frac{2}{r^2}u_{rr} - \frac{1}{r}u_{rrr} - \frac{2}{r^3}u_r\right) + \left(-\frac{6}{r^4}u_{\theta\theta} + \frac{4}{r^3}u_{r\theta\theta} - \frac{1}{r^2}u_{rr\theta\theta}\right) \\ &- k^2 u_r r - 4kk_r u_r - 2k_r^2 u - 2kk_r r u \\ &= F_{rr} - 2\left(k_r^2 + kk_{rr}\right)u - 2\left(\frac{1}{r^3} + 2kk_r\right)u_r + \left(\frac{2}{r^2} - k^2\right)u_{rr} \\ &- \frac{1}{r}u_{rrr} - \frac{6}{r^4}u_{\theta\theta} + \frac{4}{r^3}u_{r\theta\theta} - \frac{1}{r^2}u_{\theta\theta rr}. \end{aligned}$$

The mixed derivative $u_{\theta\theta rr}$ is obtained using the angular derivative of the equation:

$$u_{\theta\theta rr} = F_{\theta\theta} - \frac{1}{r}u_{r\theta\theta} - \frac{1}{r^2}u_{\theta\theta\theta\theta} - k^2 u_{\theta\theta}.$$

Finally,we define

$$\mathcal{T}_{i,j}^R \boldsymbol{Tr} u = \mathcal{T}(u, u_r, F, |p_{i,j}| - R), \quad p_{i,j} \in \gamma,$$

where $\mathcal{T}$ denotes the Taylor extension (2.31).

2.3.2.2 Auxiliary Problem

Consider the following auxiliary problem

$$\begin{cases} \boldsymbol{L}_{p_{i,j}} v_{p_{i,j}} = f_{p_{i,j}} & p_{i,j} \in \mathbb{N} \setminus \partial\mathbb{N}, \\ \boldsymbol{l}_{p_{i,j}} v_{p_{i,j}} = 0 & p_{i,j} \in \partial\mathbb{N}, \end{cases} \tag{2.33}$$

where the boundary condition $\boldsymbol{l}_{p_{i,j}} v_{p_{i,j}} = 0$ in (2.33) can be arbitrary as long as it guarantees the existence and uniqueness of the solution for any right-hand side $f_{p_{i,j}}$, and well-posedness of the entire formulation. In practice, the AP is also chosen so that it admits an easy numerical solution. For example, one can use an absorbing-type boundary condition in (2.33):

$$\boldsymbol{l}_{p_{i,j}} v_{p_{i,j}} = \begin{cases} (v_x)_{p_{i,j}} = ikv_{p_{i,j}} & x_{i,j} \in \{-x_t, x_t\}, \\ v_{p_{i,j}} = 0 & y_{i,j} \in \{-y_t, y_t\}. \end{cases} \tag{2.34}$$

The AP (2.33) is used to compute the difference potential with the density $\boldsymbol{\xi}_\gamma$ defined on the grid boundary γ. For a given $\boldsymbol{\xi}_\gamma$, we first introduce the auxiliary function

$$w_{p_{i,j}} = \begin{cases} \boldsymbol{\xi}_\gamma|_{p_{i,j}} & p_{i,j} \in \gamma, \\ 0 & \text{elsewhere}, \end{cases} \tag{2.35}$$

so that $\boldsymbol{Tr} w_{p_{i,j}} = \boldsymbol{\xi}_\gamma$. Then we define the right-hand side for the AP as follows

$$f_{p_{i,j}} = \begin{cases} \boldsymbol{L}_{p_{i,j}} w_{p_{i,j}} & p_{i,j} \in \mathbb{M}, \\ 0 & \text{elsewhere}. \end{cases} \tag{2.36}$$

2.3.2.3 Reduction To The Boundary

Denote by $v_{p_{i,j}}$ the solution to the auxiliary problem (2.33) with the right-hand side given by (2.36). The difference potential with the density $\boldsymbol{\xi}_\gamma$ is defined for the grid

nodes $p_{i,j} \in \mathbb{N}^+$ according to the following formula:

$$\boldsymbol{P}_q \boldsymbol{\xi}_\gamma = w_{p_{i,j}} - v_{p_{i,j}}, \tag{2.37}$$

where $w_{p_{i,j}}$ is given by (2.35). The difference potential (2.37) converges to the continuous potential (2.16) with the design rate as the grid size decreases, see [48, 47] and also [42].

We next assume the Fourier expansions, i.e. $b_n(\theta) = e^{in\theta}$, see Section 2.3.1.2:

$$u(R,\theta) = \sum_{n=-M}^{M} \hat{u}[n] e^{in\theta} \tag{2.38a}$$

and

$$u_r(R,\theta) = \sum_{n=-M}^{M} \widehat{u_r}[n] e^{in\theta}. \tag{2.38b}$$

When we solve the Dirichlet problem the coefficients $\hat{u}[n]$ are known while $\widehat{u_r}[n]$ are unknowns. We next define two sets of the source term via ξ_γ:

$$\xi_\gamma^I(n) = \mathcal{T}_{i,j}^R(e^{in\theta}, 0) = \mathcal{T}(e^{in\theta}, 0, 0, \delta_\Gamma),\ n \in [-M, M]$$

and another for

$$\xi_\gamma^{II}(n) = \mathcal{T}_{i,j}^R(0, e^{in\theta}) = \mathcal{T}(0, e^{in\theta}, 0, \delta_\Gamma),\ n \in [-M, M],$$

where δ_Γ represents the shortest distance between $p_{i,j} \in \gamma$ and the analytical shape Γ, i.e. in this instance $\delta_\Gamma = |p_{i,j}| - R$.

We next introduce the discrete projection

$$\boldsymbol{P}_\gamma \boldsymbol{\xi}_\gamma = \boldsymbol{P}_q \boldsymbol{\xi}_\gamma \big|_\gamma$$

and the difference counterpart of BEP (2.9):

$$\boldsymbol{P}_\gamma \boldsymbol{\xi}_\gamma = \boldsymbol{\xi}_\gamma \tag{2.39}$$

or equivalently

$$(w_{p_{i,j}} - v_{p_{i,j}})|_\gamma = w_{p_{i,j}}|_\gamma.$$

We rewrite the BEP (2.39) as

$$P_\gamma \boldsymbol{\xi}_\gamma - \boldsymbol{\xi}_\gamma = 0,$$

and define

$$\boldsymbol{Q}_q \boldsymbol{\xi}_\gamma = (\boldsymbol{P}_q - I)\boldsymbol{\xi}_\gamma = (w_{p_{i,j}} - v_{p_{i,j}})|_\gamma - w_{p_{i,j}}|_\gamma = -v_{p_{i,j}}|_\gamma. \tag{2.40}$$

We next use (2.26) to recast (2.40) as

$$\boldsymbol{Q}_q \boldsymbol{\xi}_\gamma = \boldsymbol{Q}_q \xi_\gamma^I + \boldsymbol{Q}_q \xi_\gamma^{II},$$

where

$$\boldsymbol{Q}_q \xi_\gamma^m = \sum c_n^{m,q} \boldsymbol{Q}_q \xi_{\gamma,q}^m(n),$$

see (2.25). We next combine $Q_q\xi_\gamma^I(n)$ and $Q_q\xi_\gamma^{II}(n)$ in a matrix:

$$\boldsymbol{Q} = [\boldsymbol{Q}_I|\boldsymbol{Q}_{II}] = \left(\begin{array}{ccc|ccc} | & & | & | & & | \\ Q_q\xi_\gamma^I(-M) & \cdots & Q_q\xi_\gamma^I(M) & Q_q\xi_\gamma^{II}(-M) & \cdots & Q_q\xi_\gamma^{II}(M) \\ | & & | & | & & | \end{array}\right). \tag{2.41}$$

The size of the matrix $\boldsymbol{Q}$ is $|\gamma| \times 2(2M+1)$, where $|\gamma|$ denotes number of nodes of grid in γ, which also the size of $Q_q\xi_\gamma^m(n)$ and $\xi_\gamma^m(n)$. Thus, we are looking for a non-zero vector

$$\boldsymbol{c} = [\hat{u}[-M], \ldots, \hat{u}[M], \widehat{u_r}[-M], \ldots, \widehat{u_r}[M]]^T \tag{2.42}$$

that satisfies

$$\boldsymbol{Q}\boldsymbol{c} = 0. \tag{2.43}$$

2.3.2.4 The Solution

Equation (2.43) has multiple solutions since we did not yet use the boundary condition, which we do now. The problem (2.29) is a Dirichlet problem and therefore the $2M+1$ coefficients of (2.38a) are easy to calculate by Fourier transforming the data $g(\theta)$. One then denotes

$$\boldsymbol{c}^I = [\hat{u}[-M], \ldots, \hat{u}[M]]^T, \tag{2.44}$$

$$\boldsymbol{c}^{II} = [\widehat{u_r}[-M], \ldots, \widehat{u_r}[M]]^T. \tag{2.45}$$

and rewrite (2.43) as a system of equations with respect to $\boldsymbol{c}^{II}$

$$\boldsymbol{Q}_{II}\boldsymbol{c}^{II} = -\boldsymbol{Q}_{I}\boldsymbol{c}^{I}. \tag{2.46}$$

For a sufficiently fine grid, system (2.46) is overdetermined, and its solution is to be sought for in the sense of the least squares. However, as the solution to the original continuous problem exists, and system (2.46) equivalently represents its fourth order accurate finite difference approximation, the residual of its least squares solution is expected to vanish with the rate $O(h^4)$ as the grid is refined. In this sense, the overdetermined system (2.46) can be said to have an "almost classical" solution.

To obtain the solution to problem (2.29) one again solves the auxiliary problem (2.33). Thus, the approximation is given by $u = \boldsymbol{P}_q\,\xi_\gamma$ where

$$\xi_\gamma = \sum_n \hat{u}[n]\xi_\gamma^I(n) + \sum_n \widehat{u_r}[n]\xi_\gamma^{II}(n)$$

where now all the coefficients are known.

2.3.3 Cartesian Coordinates: Homogeneous Neumann Problem in a Circle

Consider the Neumann problem:

$$\begin{cases} \Delta u + k^2 u = 0 & x^2 + y^2 < R^2, \\ u_r(x,y) = g(x,y) & x^2 + y^2 = R^2. \end{cases} \tag{2.47}$$

The solution to the problem (2.47) is similar to the solution of (2.29). The main difference is that unlike in (2.29) where first $2M+1$ elements of $\boldsymbol{c}$ are known in Neumann problem the second $2M+1$ elements of $\boldsymbol{c}$ are known and the first $2M+1$ elements are unknown. Thus, to solve the Neumann problem one exchanges between the right hand side and left hand side of (2.46), i.e.

$$\boldsymbol{Q}_I \boldsymbol{c}^I = -\boldsymbol{Q}_{II} \boldsymbol{c}^{II} \tag{2.48}$$

and the rest of the procedure remains unchanged. Therefore, one computes unknown coefficients using (2.48) and approximates the solution to problem (2.47) by computing

$$\xi_\gamma = \sum_n \hat{u}[n] \xi_\gamma^I(n) + \sum_n \widehat{u_r}[n] \xi_\gamma^{II}(n)$$

and then solving an auxiliary problem (2.33) for $u = \boldsymbol{P}_q \xi_\gamma$.

2.3.4 Cartesian Coordinates: Homogeneous Robin Problem in a Circle

We next consider the Robin problem:

$$\begin{cases} \Delta u + k^2 u = 0 & x^2 + y^2 < R^2, \\ \alpha u(x,y) + \beta u_r(x,y) = g(x,y) & x^2 + y^2 = R^2, \end{cases} \tag{2.49}$$

where $\alpha^2 + \beta^2 \neq 0$. One uses the orthogonality of the basis in the expansions (2.38) to rewrite the boundary condition as $\alpha \hat{u}[n] + \beta \widehat{u_r}[n] = \hat{g}[n],\ \forall n \in [-M, M]$. Hence,

one solves the following system of equations

$$\alpha \boldsymbol{c}^I + \beta \boldsymbol{c}^{II} = \hat{g}, \tag{2.50}$$

$$\boldsymbol{Q}_I \boldsymbol{c}^I + \boldsymbol{Q}_{II} \boldsymbol{c}^{II} = 0. \tag{2.51}$$

One solves (2.50) to find $\boldsymbol{c}^{II}$

$$\boldsymbol{c}^{II} = \frac{1}{\beta}\hat{g} - \frac{\alpha}{\beta}\boldsymbol{c}^I \tag{2.52}$$

and then uses it in (2.51) to obtain

$$\boldsymbol{Q}_I \boldsymbol{c}^I + \boldsymbol{Q}_{II}(\frac{1}{\beta}\hat{g} - \frac{\alpha}{\beta}\boldsymbol{c}^I) = 0$$

and hence one solves

$$(\boldsymbol{Q}_I - \frac{\alpha}{\beta}\boldsymbol{Q}_{II})\boldsymbol{c}^I = -\frac{1}{\beta}\boldsymbol{Q}_{II}\hat{g} \tag{2.53}$$

to find $\boldsymbol{c}^I$ and substitute it in (2.52) to obtain $\boldsymbol{c}^{II}$.

Alternatively, one solves

$$(\boldsymbol{Q}_{II} - \frac{\beta}{\alpha}\boldsymbol{Q}_I)\boldsymbol{c}^{II} = -\frac{1}{\alpha}\boldsymbol{Q}_I\hat{g}$$

to compute $\boldsymbol{c}^{II}$, and then substitute it in $\boldsymbol{c}^I = \frac{1}{\alpha}\hat{g} - \frac{\beta}{\alpha}\boldsymbol{c}^{II}$.

Once the coefficients $\boldsymbol{c}^I, \boldsymbol{c}^{II}$ are known, one then computes

$$\xi_\gamma = \sum_n \hat{u}[n]\xi_\gamma^I(n) + \sum_n \widehat{u_r}[n]\xi_\gamma^{II}(n)$$

to approximate the solution to the problem (2.49) by solving an auxiliary problem

(2.33) for $u = \boldsymbol{P}_q \xi_\gamma$.

2.3.5 Cartesian Coordinates: Inhomogeneous Equation in an Ellipse

We next present the inhomogeneous Dirichlet problem (2.54) for an elliptical body to be solved on a Cartesian grid, see Figure 2.6.

$$\begin{cases} \Delta u + k^2 u = F(x,y) & \frac{x^2}{a^2} + \frac{y^2}{b^2} < 1, \\ u(x,y) = g(x,y) & \frac{x^2}{a^2} + \frac{y^2}{b^2} = 1, \end{cases} \tag{2.54}$$

where $a = d\cosh\eta_0, b = d\sinh\eta_0$ are the major and minor semiaxes of the ellipse respectively, $d = \sqrt{a^2 - b^2}$ is the focal distance and η_0 is the elliptical radial coordinate. One reexpresses (2.54) using

$$\eta(x,y) = \operatorname{Re}\left(\operatorname{arcosh}\frac{x+iy}{d}\right)$$

as

$$\begin{cases} \Delta u + k^2 u = F(x,y) & \eta(x,y) < \eta_0, \\ u(x,y) = g(x,y) & \eta(x,y) = \eta_0. \end{cases} \tag{2.55}$$

The finite-difference approximation to this problem is given by an auxiliary problem (2.33). The grid $\mathbb{N}$ is the Cartesian grid on $(-x_t, x_t) \times (-y_t, y_t)$, see Figure 2.6 and $p_{i,j} = (x_i, y_j) \in \mathbb{N}$ is the node of the grid. Instead of $|p_{i,j}|$ we define $\eta_{i,j} \equiv \eta(p_{i,j}) = \eta(x_i, y_j)$ and denote $\mathbb{M} = \{p_{i,j} : \eta_{i,j} < \eta_0\}$. The definition of γ remains unchanged.

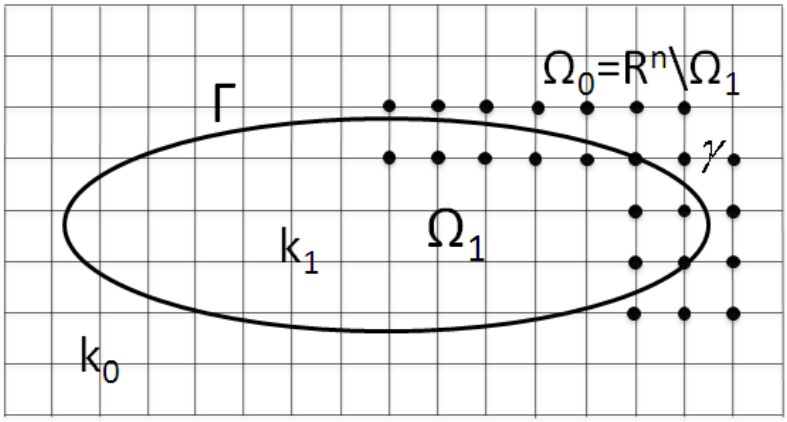

Figure 2.6: Example of discrete auxiliary problem: elliptical body in Cartesian coordinates.

Obviously, since the boundary is not aligned to the grid one needs to develop an Equation Based Taylor extension for the new curve. The general case is explained in [42]. Here we limit our discussion to the Helmholtz equation in elliptical coordinates

$$\frac{1}{h^2(\eta,\varphi)}(u_{\eta\eta}+u_{\varphi\varphi})+k^2(\eta,\varphi)u=F(\eta,\varphi), \tag{2.56}$$

where $h(\eta,\varphi)=d\sqrt{\sinh^2\eta+\sin^2\varphi}$ is the scale factor.

We first solve (2.56) for $u_{\eta\eta}$ to get

$$u_{\eta\eta}=h^2F-u_{\varphi\varphi}-h^2k^2u$$

then we differentiate it to get the third derivative

$$u_{\eta\eta\eta}=2hh_\eta F+h^2F_\eta-u_{\eta\varphi\varphi}-2\left(hh_\eta k^2+h^2kk_\eta\right)u-h^2k^2u_\eta$$

and the fourth derivative

$$\begin{aligned} u_{\eta\eta\eta\eta} &= 2\left(h_\eta^2 + hh_{\eta\eta}\right)F + 4hh_\eta F_\eta + h^2 F_{\eta\eta} - u_{\eta\eta\varphi\varphi} \\ &- 2\left(\left(h_\eta^2 + hh_{\eta\eta}\right)k^2 + 4hkh_\eta k_\eta + h^2 k k_{\eta\eta} + h^2 k_\eta^2\right)u \\ &- 4\left(hh_\eta k^2 + h^2 k k_\eta\right)u_\eta - h^2 k^2 u_{\eta\eta} \end{aligned}$$

and similarly

$$\begin{aligned} u_{\eta\eta\varphi\varphi} &= 2\left(h_\varphi^2 + hh_{\varphi\varphi}\right)F + 4hh_\varphi F_\varphi + h^2 F_{\varphi\varphi} - u_{\varphi\varphi\varphi\varphi} \\ &- 2\left(\left(h_\varphi^2 + hh_{\varphi\varphi}\right)k^2 + 4hkh_\varphi k_\varphi + h^2 k k_{\varphi\varphi} + h^2 k_\varphi^2\right)u \\ &- 4\left(hh_\varphi k^2 + h^2 k k_\varphi\right)u_\varphi - h^2 k^2 u_{\varphi\varphi} \end{aligned}$$

We next use these derivatives in

$$u\left(\eta + h, \varphi\right) = u\left(\eta, \varphi\right) + hu_\eta + \frac{h^2}{2}u_{\eta\eta} + \frac{h^3}{6}u_{\eta\eta\eta} + \frac{h^4}{24}u_{\eta\eta\eta\eta} \tag{2.57}$$

and define

$$\mathcal{T}_{i,j}^{\eta_0}\boldsymbol{Tr}u = \mathcal{T}(u, u_\eta, F, \eta_{i,j} - \eta_0), \quad p_{i,j} \in \gamma, \tag{2.58}$$

where $\mathcal{T}$ denotes Taylor extension (2.57).

We next assume the Fourier expansions

$$u(\eta_0, \varphi) = \sum_{n=-M}^{M} \hat{u}[n]e^{in\varphi} \tag{2.59a}$$

and

$$u_\eta(\eta_0,\varphi)=\sum_{n=-M}^{M}\widehat{u}_\eta[n]e^{in\varphi} \tag{2.59b}$$

and define the sets of $\xi_\gamma^m(n)$. In order to reduce the computational cost instead of two sets

$$\xi_\gamma^I(n)=\mathcal{T}(e^{inx},0,F,\delta_\Gamma),\ n\in[-M,M]$$

and

$$\xi_\gamma^{II}(n)=\mathcal{T}(0,e^{inx},F,\delta_\Gamma),\ n\in[-M,M],$$

where $\delta_\Gamma=\eta_{i,j}-\eta_0$ is the shortest distance from $p_{i,j}\in\gamma$ to Γ. One solves these two sets without the source term i.e.

$$\xi_\gamma^I(n)=\mathcal{T}(e^{inx},0,0,\delta_\Gamma),\ n\in[-M,M]$$

and

$$\xi_\gamma^{II}(n)=\mathcal{T}(0,e^{inx},0,\delta_\Gamma),\ n\in[-M,M]$$

and defines an additional AP for the source term F. This is done so we need to compute it's part of the extension only once

$$\xi_\gamma^F=\mathcal{T}(0,0,F,\delta_\Gamma),\ n\in[-M,M].$$

This adds another column to the matrix $\boldsymbol{Q}$ in equation (2.43), $Q_q\xi_\gamma^F=(\boldsymbol{P}_q-I)\xi_\gamma^F$. More precisely there is another change to (2.43), i.e. it's become inhomogeneous:

$$\boldsymbol{Q}\boldsymbol{c}=-GF|_\gamma, \tag{2.60}$$

where GF is the solution of AP (2.33) with

$$f_{p_{i,j}} = \begin{cases} \boldsymbol{B}\widetilde{\mathcal{T}}F_{p_{i,j}} & p_{i,j} \in \mathbb{M} \cup \gamma, \\ 0 & elsewhere, \end{cases} \tag{2.61}$$

where the operator $\boldsymbol{B}$ represents the right hand side stencil of the compact scheme, see Section 1.2.1, particularly the right hand side of (1.8). Note that $\boldsymbol{B}$ requires F to be defined for $p_{i,j}$ for which $\eta_{i,j} \geq \eta_0$ where F is not necessary known. Therefore, one extends the source term F to these nodes using regular (non equation based) Taylor extension which we denote $\widetilde{\mathcal{T}}$. See also [42].

Thus, the equation (2.46) becomes

$$\boldsymbol{Q}_{II}\widehat{u_\eta}[n] = -\boldsymbol{Q}_I\hat{u}[n] - Q_q\xi_\gamma^F - GF|_\gamma. \tag{2.62}$$

To obtain the solution to problem (2.55) one computes the coefficients from (2.62) and then solves the auxiliary problem $\boldsymbol{P}_q\,\xi_\gamma$ using

$$\xi_\gamma = \sum_n \hat{u}[n]\xi_\gamma^I(n) + \sum_n \widehat{u_\eta}[n]\xi_\gamma^{II}(n) + Q_q\xi_\gamma^F.$$

Finally $u = \boldsymbol{P}_q\,\xi_\gamma + GF$.

2.3.6 Polar Coordinates: Scattering about an Ellipse

Consider the scattering problem in polar coordinates about an elliptical body

$$\begin{cases} u^s_{rr} + \frac{1}{r}u^s_r + \frac{1}{r^2}u^s_{\theta\theta} + k^2 u^s = 0 & \eta(R,\theta) > \eta_0, \\ u^s(R,\theta) = g(\theta) & \eta(R,\theta) = \eta_0, \\ \lim\limits_{r\to\infty} r^{\frac{1}{2}}(u^s_r + iku^s) = 0. \end{cases} \tag{2.63}$$

where u^s denotes a scattering field, $g(\theta) = -u^{(\text{inc})}(\theta) = e^{-ik(x\cos\theta + y\sin\theta)}$ is an incident wave, η_0 is the elliptical radial coordinate and

$$\eta(r,\theta) = \text{Re}\left(\text{arcosh}\,\frac{re^{i\theta}}{d}\right),$$

and d is the semi-focal distance, see Figure 1.2.

Since on a computer one can't solve the problem in an infinite domain one truncates the infinite domain and defines an artificial boundary. It is convenient to choose the artificial boundary to be aligned to the the grid, therefore, the numerical domain becomes a ring, Figure 2.7. The Sommerfeld condition $\lim\limits_{r\to\infty} r^{\frac{1}{2}}(u^s_r + iku^s) = 0$ is changed to an Absorbing Boundary Condition (ABC) which uses the decomposition of the waves into incoming and outgoing and allows the propagation of only the outgoing waves. Such an approach resembles the idea of Sommerfeld condition of "no wave radiating from infinity" by "no wave is entering the computational domain" or more precisely no wave is reflecting from the artificial boundary. This is a commonly used approach [64, 29], and is valid since we are considering only regular bounded solutions, which eliminates the possible ambiguity in the definition of the

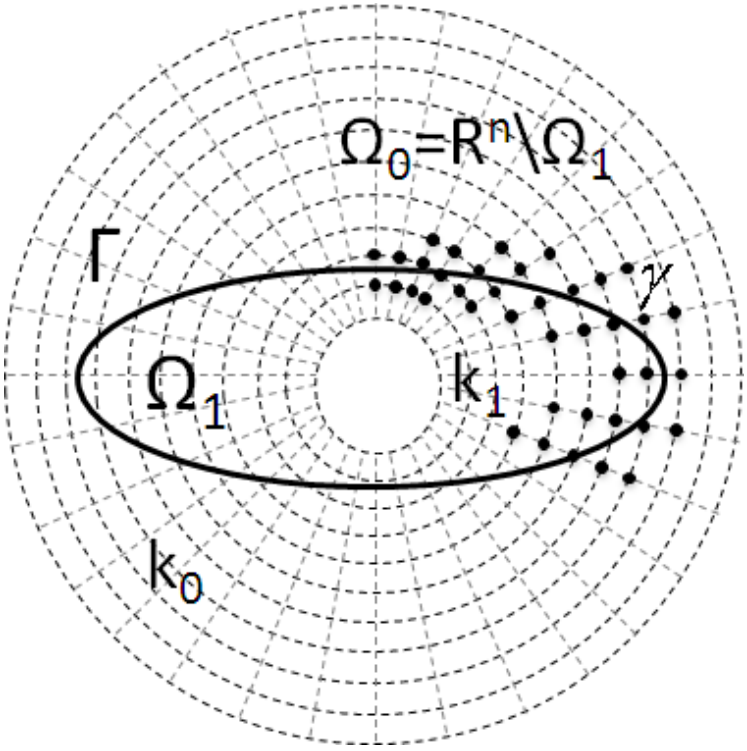

Figure 2.7: Example of discrete auxiliary problems: elliptical body in polar coordinates.

incoming and outgoing waves pointed out in [17].

Occasionally, for an elliptical or oval like scatterer one wishes that the outer artificial surface resemble the scatterer to prevent unnecessary interior nodes. One then uses an ABC in elliptical coordinates (see [44, 43, 41]). However, we set the artificial boundary on an outer circle of the grid. We Fourier transform the auxiliary problem (2.33) to get a linearly solved tridiagonal linear system [15], see algorithm described in [8]. Therefore, in this instance we neglect the problem of redundant nodes.

The AP (2.33), transformed to the Fourier space, has the advantage that the

ABC becomes an exact condition instead of an approximation of the Sommerfeld condition [8]. The boundary condition on the inner circle may be chosen arbitrarily since unlike the ABC it belongs to the AP but not to the original problem. One defines a homogeneous boundary condition on the inner circle. By this we accomplish the new definition of $l_{p_{i,j}}$ in (2.33).

One then uses an Equation Based Taylor extension $\mathcal{T}_{i,j}^{\eta_0}$ defined in (2.58) (see [42] for more general case) and assumes the Fourier expansion of the solution on an interface Γ as given in equations (2.59a) and (2.59b). Next, one solves the AP for

$$\xi_\gamma^I(n) = \mathcal{T}(e^{inx}, 0, 0, \delta_\Gamma),\ n \in [-M, M]$$

and

$$\xi_\gamma^{II}(n) = \mathcal{T}(0, e^{inx}, 0, \delta_\Gamma),\ n \in [-M, M],$$

where $\delta_\Gamma = \eta_{i,j} - \eta_0$ is the shortest distance from $p_{i,j} \in \gamma$ to Γ.

Finally, one defines the matrix $\boldsymbol{Q}$ and using (2.40), one solves

$$\boldsymbol{Q}_{II}\widehat{u_\eta^s}[n] = -\boldsymbol{Q}_I\widehat{u^s}[n], \tag{2.64}$$

where $\widehat{u^s} = -\widehat{u^{(\mathrm{inc})}}$ and computes

$$\xi_\gamma = \sum_n \widehat{u^s}[n]\xi_\gamma^I(n) + \sum_n \widehat{u_\eta^s}[n]\xi_\gamma^{II}(n)$$

to approximate the solution to problem (2.63) as $u^s = \boldsymbol{P}_q\,\xi_\gamma$ or the total field as $u = u^s + u^{(\mathrm{inc})} = \boldsymbol{P}_q\,\xi_\gamma + u^{(\mathrm{inc})}$.

2.3.7 Transmission–Reflection problem

Consider the problem (1.2) described also in Figure 1.1. For convenience we redefine it as

$$\begin{cases} \Delta u + k_0^2 u = 0 & \boldsymbol{x} \in \Omega_0, \\ \Delta u + k_1(\boldsymbol{x})^2 u = F(\boldsymbol{x}) & \boldsymbol{x} \in \Omega_1. \end{cases} \tag{2.65}$$

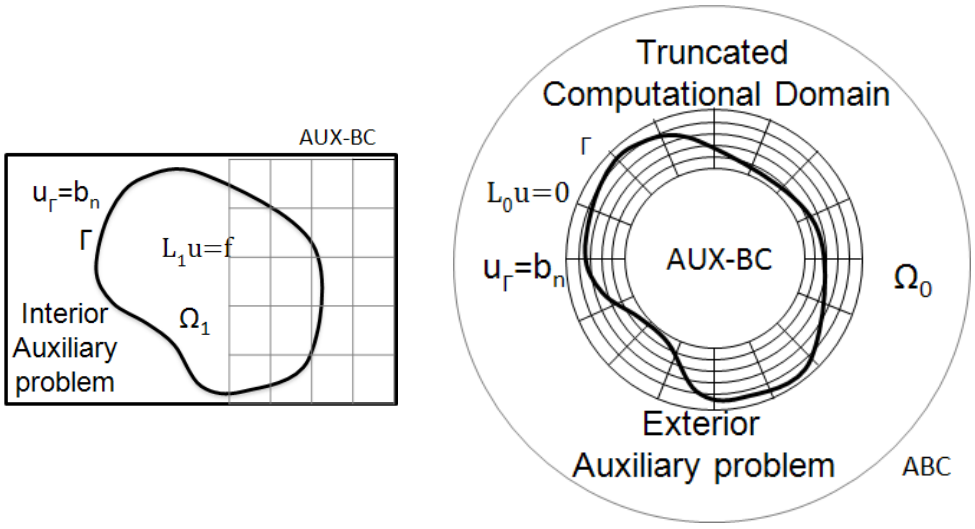

Figure 2.8: Interior and Exterior subproblems

In this instance we consider that Γ is an ellipse and therefore the auxiliary problems that solve system of BEPs (2.17) becomes the problems (2.54) and (2.63). When these problems are solved the information about the boundary function of these problems, g, are used at a very late stage. More precisely the matrices $\boldsymbol{Q}$ in both problems are computed without any knowledge about g and this fact is a key property.

Thus, one defines four sets of ξ_γ, two sets $\xi^I_{\gamma,0}(n)$, $\xi^{II}_{\gamma,0}(n)$ for the exterior and two

sets $\xi^I_{\gamma,1}(n)$, $\xi^{II}_{\gamma,1}(n)$ for the interior subproblem, i.e. assume an expansion (2.59a), (2.59b) and obtain a matrix $\boldsymbol{Q}$.

Let $\boldsymbol{Q}^1$ be the matrix $\boldsymbol{Q}$ of the interior subproblem (2.54) for which the BEP is given by

$$\boldsymbol{Q}^1\boldsymbol{c} = -Q_1\xi^F_\gamma - \boldsymbol{G}^1_F|_\gamma$$

and let $\boldsymbol{Q}^0$ be the matrix $\boldsymbol{Q}$ of the interior subproblem (2.63) with it's BEP

$$\boldsymbol{Q}^0\boldsymbol{c} = Q_0\xi^{(\mathrm{inc})}_\gamma.$$

When problems (2.54) and (2.63) are solved half of the vector of coefficients $\boldsymbol{c}$ are known from the boundary condition and the other half are solved. In this instance $\boldsymbol{c}$ is fully unknown, and instead one solves

$$\begin{pmatrix} \boldsymbol{Q}^1 \\ \boldsymbol{Q}^0 \end{pmatrix} \boldsymbol{c} = \begin{pmatrix} -Q_1\xi^F_\gamma - \boldsymbol{G}^1_F|_\gamma \\ Q_0\xi^{(\mathrm{inc})}_\gamma \end{pmatrix}, \tag{2.66}$$

which is again overdetermined for a fine enough grid and it's solution exists again as long as solution to original problem does. Hence (2.66) is understood in the least square sense.

To approximate the solution to problem (2.65) one computes

$$\xi^1_\gamma = \sum_n \hat{u}[n]\xi^I_\gamma(n) + \sum_n \widehat{u_\eta}[n]\xi^{II}_\gamma(n) + Q_1\xi^F_\gamma.$$

and

$$\tilde{\xi}_\gamma^0 = \sum_n \widehat{u^s}[n]\xi_\gamma^I(n) + \sum_n \widehat{u_\eta^s}[n]\xi_\gamma^{II}(n)$$

and solves

$$u = \begin{cases} \boldsymbol{P}_1\, \xi_\gamma^1 + G_F^1 & \boldsymbol{x} \in \Omega_1, \\ \boldsymbol{P}_0\, [\tilde{\xi}_\gamma^0 - \xi_\gamma^{(\mathrm{inc})}] + u^{(\mathrm{inc})} & \boldsymbol{x} \in \Omega_0. \end{cases}$$

2.4 Complexity

The key contribution to the overall complexity of the proposed algorithm is the repeated solution of the discrete AP (2.33). Each subproblem of the transmission reflection problem needs to be solved $(2M+1)$ times to find the coefficients and one more to obtain the solution when coefficients are known. Altogether, it needs to be solved $4(M+1)$ times. However, only the right-hand side of the AP changes from time to time, whereas the two operators remain the same.

In the case of constant coefficients, each of the $4(M+1)$ equations requires a FFT solve which has a log-linear complexity with respect to $|\mathbb{N}|$, the dimension of the problem, i.e. the number of nodes of the grid $\mathbb{N}$. In the case of variable coefficients, the overall complexity will be that of a single sparse LU decomposition of a matrix of dimension $|\mathbb{N}| \times |\mathbb{N}|$ plus $4(M+1)$ backward substitutions. This is, of course, significantly faster than solving the overall system many times.

In the case of variable coefficients, one can use an iterative solver, for example see [65]. In 3D, a straightforward Gaussian elimination (LU decomposition) is not feasible. For constant coefficients, a Fourier based solver that does not require

storing the matrix and has a log-linear complexity will provide the most efficient approach to solution, if, of course, the AP can be formulated so that it will admit the solution by FFT. Otherwise, an iterative solve will become a necessity in 3D for either variable or constant coefficients. For example, using the iterative scheme Risolv of [61], one needs to find the optimal parameters of the algorithm only once independent of the RHS. Let N_{nz} be the number of non-zero entries in the system matrix that has the dimension $|\mathbb{N}|\times|\mathbb{N}|$, N_{K} be the dimension of the Krylov subspace, and N_{A} be the number of times we apply the Arnoldi algorithm. Then the total amount of work for the first solve, i.e., for one RHS, is approximately $N_{\mathrm{A}}\times N_{\mathrm{K}}\times N_{\mathrm{nz}}+ N_{\mathrm{A}}\times\frac{1}{2}N_{\mathrm{K}}^2\times|\mathbb{N}|$. For each subsequent solve the total work is approximately $N_{\mathrm{A}}\times N_{\mathrm{K}}\times N_{\mathrm{nz}}$. Hence, it no longer depends on $N_{\mathrm{K}}^2|\mathbb{N}|$, which means that the dependence on the dimension $|\mathbb{N}|$ of the system matrix disappears, and the dependence on the dimension N_{K} of the Krylov subspace becomes linear rather than quadratic. Regarding the preconditioning of the Helmholtz equation, see, e.g. [21, 19, 18, 20].

Another contribution to the overall complexity is the QR decomposition. If the modified Gram-Schmidt algorithm is used, then the corresponding cost is about $2(2M+1)^2|\gamma|$ operations, where for the current two-dimensional setting $|\gamma|\sim\sqrt{|\mathbb{N}|}$. The cost of all other components of the algorithm, see Section 2.3.1, is negligible.

We re-emphasize that as the discretization grid is refined, only the quantities $|\mathbb{N}|$ and $|\gamma|$ increase, whereas M stays the same. This is the strategy we have adopted for all our numerical simulations, see Chapter 3. Of course, choosing M grid-independent represents the most conservative scenario. It allows us to make sure that the accuracy of the spectral representation at the boundary (in the basis of dimension M) will certainly exceed any accuracy that one may possibly obtain

on the grid. In fact, M does not always have to be chosen this way. For coarser grids it can be smaller, which will yield additional savings, see [10, Section 4.5].

Chapter 3

Results

3.1 Interior problems on a Cartesian grid

3.1.1 Schemes of various accuracy

We first solve the interior Dirichlet problem for the constant coefficient homogeneous Helmholtz equation:

$$\begin{aligned} \Delta u + k^2 u &= 0 \quad \text{on} \quad \Omega, \\ u\big|_{\Gamma} &= \phi, \end{aligned} \tag{3.1}$$

on the domain Ω which is a disk of radius $R = 3$ centered at the origin. The auxiliary problem (2.33) is formulated on a larger square $\widetilde{\Omega} = (-\pi, \pi) \times (-\pi, \pi)$ and consists of solving the inhomogeneous Helmholtz equation

$$\Delta v + k^2 v = g$$

subject to the zero Dirichlet boundary condition $v\big|_{\partial\widetilde{\Omega}} = 0$. To avoid resonances and guarantee uniqueness of the solution to the AP, we require that $k^2 \neq l^2 + m^2$, where l and m are any two integers. The AP is solved by a sparse LU decomposition.

We take the test solution of problem (3.1) in the form of a plane wave:

$$u(x, y) = e^{i(k_x x + k_y y)}, \quad \text{where} \quad k_x^2 + k_y^2 = k^2, \tag{3.2}$$

so that the boundary data in (3.1) become

$$\phi(\theta) = e^{iR(k_x \cos\theta + k_y \sin\theta)}, \tag{3.3}$$

where θ is the polar angle. The specific values that we choose are: $k_x = \frac{4}{5}k$ and $k_y = \frac{3}{5}k$ and k to be chosen later. We note that in further discussion we use the notation of k rather than non-dimensional kD where D is a radius R or the major elliptical semi-axis a since the size shape is fixed.

To discretize the Helmholtz equation, we use a uniform, in both directions, Cartesian grid with size h on the square $\widetilde{\Omega}$ (the domain of the AP). In doing so, the circular boundary Γ of the domain Ω, i.e., the domain of the original problem (3.1), does not conform to the grid. The Helmholtz equation is discretized by means of the following three schemes:

1. The standard central difference second order accurate scheme on the five-node stencil;

2. The fourth order accurate compact scheme of Section 1.2.1, which uses the nine-node stencil shown in Figure 2.2 [the equation in (3.1) is homogeneous,

and no stencil is needed for the right-hand side]. For the case of $k = \text{const}$, the scheme simplifies compared to formula (1.8);

3. The sixth order accurate compact scheme of [56], which uses the same nine-node stencil.

The goals of the computations are to demonstrate the design order of the grid convergence of the numerical solution to the exact solution for a non-conforming boundary. We also determine what is the minimum number of Taylor derivatives needed to maintain the required order of accuracy of the overall scheme; see discussion before formula (2.31) or [42]. An additional goal is to show how the pollution effect [35, 5, 2] manifests itself.

The grid convergence is studied by solving on a sequence of grids of increasing dimension: $2^d \times 2^d$, from 16×16 to the maximum of 1024×1024. So for a given d the grid size is $h = \frac{2\pi}{2^d} = \pi 2^{1-d}$, and it is halved every time the grid dimension is increased.

We have solved problem (3.1) for five different values of the wavenumber k: 1, 3, 6.7, 12.8, and 25.6. For the highest k that we have considered, the test solution (3.2) already exhibits a fair amount of oscillations on the domain Ω — about 25 full wavelengths along the radius, as shown in Figure 3.1. The results of computations for all k's are presented in Table 3.1 through Table 3.5.

Altogether, Tables 3.1 – 3.5 show that for every scheme we have tested, the proposed methodology guarantees the design rate of grid convergence for a non-conforming boundary and a Cartesian grid.

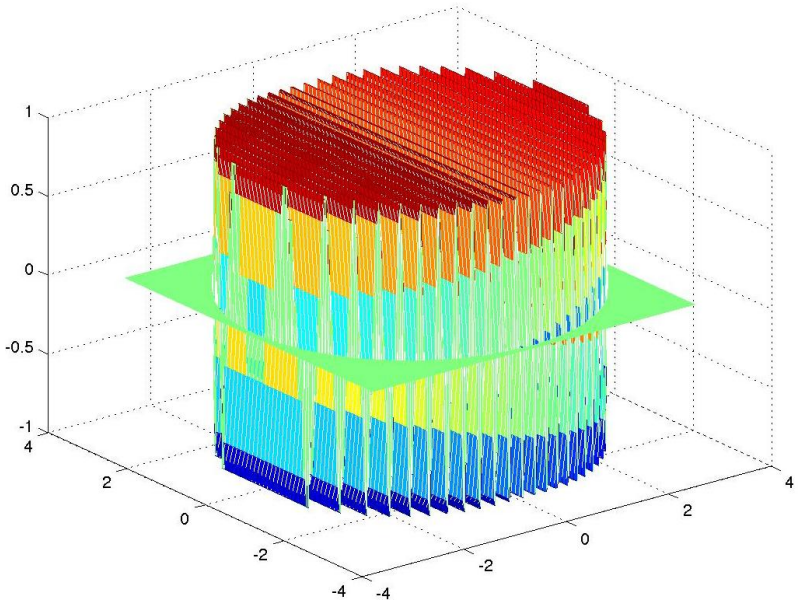

(a) Real Part

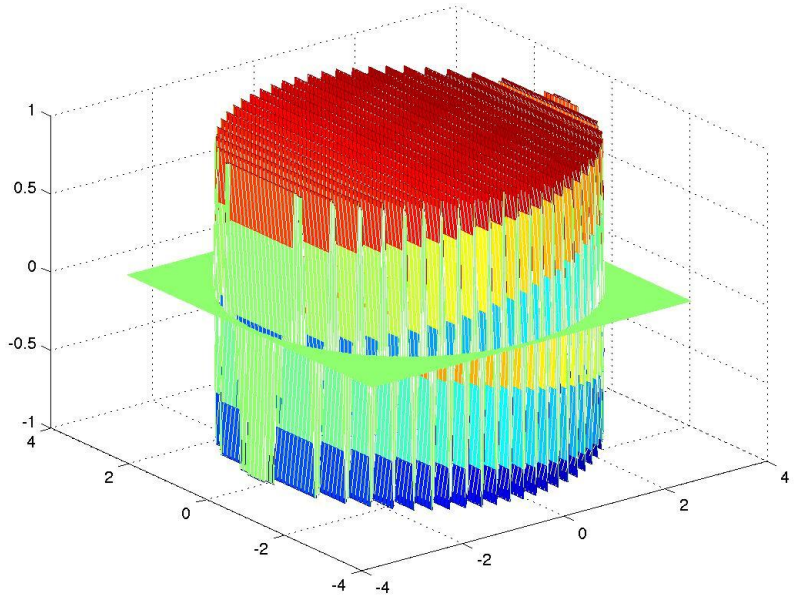

(b) Imaginary Part

Figure 3.1: Real and Imaginary part of the test solution (3.2) for $k = 25.6$.

Grid	Scheme					
	2nd order ctr. difference		4th order compact		6th order compact	
	$\|u - u_{num}\|_\infty$	rate	$\|\|u - u_{num}\|\|_\infty$	rate	$\|\|u - u_{num}\|\|_\infty$	rate
16×16	3.474855e-2	—	4.590536e-4	—	3.626766e-6	—
32×32	5.346252e-3	2.7004	5.163260e-6	6.4742	8.250530e-9	8.7800
64×64	1.238241e-3	2.1102	1.704410e-7	4.9209	6.486869e-11	6.9908
128×128	3.001289e-4	2.0446	9.090205e-9	4.2288	1.112940e-12	5.8651
256×256	7.389904e-5	2.0220	3.272063e-10	4.7960	2.343009e-12	-1.0740
512×512	1.835138e-5	2.0097	2.457055e-11	3.7352	7.287204e-12	-1.6370
1024×1024	4.571995e-6	2.0050	3.070920e-11	-0.3217	2.411052e-11	-1.7262

Table 3.1: Grid convergence for the wavenumber $k = 1$ and the dimension of the basis (2.38) $M = 17$. Note that the apparent breakdown of convergence of higher order schemes on finer grids is due to the loss of significant digits, as the absolute levels of the error become very small and approach machine zero.

Grid	Scheme					
	2nd order ctr. difference		4th order compact		6th order compact	
	$\|u - u_{num}\|_\infty$	rate	$\|\|u - u_{num}\|\|_\infty$	rate	$\|\|u - u_{num}\|\|_\infty$	rate
16×16	2.157031	—	1.093211	—	6.252035e-2	—
32×32	2.212195e-1	3.2855	1.491703e-3	9.5174	1.905533e-5	11.6799
64×64	6.296501e-2	1.8129	4.695925e-5	4.9894	2.743013e-7	6.1183
128×128	1.621645e-2	1.9571	2.736886e-6	4.1008	3.956555e-9	6.1154
256×256	4.049416e-3	2.0017	1.612331e-7	4.0853	5.830238e-11	6.0845
512×512	1.008930e-3	2.0049	9.823236e-9	4.0368	1.288003e-12	5.5003
1024×1024	2.515190e-4	2.0041	6.235303e-10	3.9777	7.870095e-12	-2.6112

Table 3.2: Grid convergence for the wavenumber $k = 3$ and the dimension of the basis (2.38) $M = 28$.

The dimension M of the basis (2.38) is chosen by Fourier transforming the boundary data (3.3) of problem (3.1) and truncating the series at the machine precision level (`double precision`). The resulting values of M for every k are provided in the captions to Tables 3.1 – 3.5. We see that M increases as k increases. This is not surprising, as the solution becomes more oscillatory;[1] for example, our highest $k = 25.6$ corresponds to over 75 full wavelengths along the circumference

[1] Convergence of the Fourier series remains exponential due to the smoothness, but the constants become larger.

Grid	Scheme					
	2nd order ctr. difference		4th order compact		6th order compact	
	$\|u - u_{num}\|_\infty$	rate	$\|\|u - u_{num}\|\|_\infty$	rate	$\|\|u - u_{num}\|\|_\infty$	rate
16×16	8.228113	—	7.976387	—	1.459757e+1	—
32×32	4.299483	0.9364	1.001469e-1	6.3155	1.071898e-2	10.4113
64×64	1.933134	1.1532	4.111705e-3	4.6062	1.345917e-4	6.3154
128×128	3.065574e-2	2.6567	2.420283e-4	4.0865	1.845635e-6	6.1883
256×256	7.028536e-3	2.1249	1.488596e-5	4.0232	2.757929e-8	6.0644
512×512	1.861682e-3	1.9166	9.101549e-7	4.0317	4.192718e-10	6.0396
1024×1024	4.726287e-4	1.9778	5.640010e-8	4.0123	1.170244e-11	5.1630

Table 3.3: Grid convergence for the wavenumber $k = 6.7$ and the dimension of the basis (2.38) $M = 43$.

Grid	Scheme					
	2nd order ctr. difference		4th order compact		6th order compact	
	$\|u - u_{num}\|_\infty$	rate	$\|\|u - u_{num}\|\|_\infty$	rate	$\|\|u - u_{num}\|\|_\infty$	rate
16×16	3.135403e+1	—	7.284196e+1	—	9.174488e+1	—
32×32	2.693366e+1	0.2192	4.960223	3.8763	1.344958e+1	2.7701
64×64	8.177246	0.2192	1.233802	2.0073	8.032610e-2	7.3875
128×128	1.095035e+1	-0.4213	3.200884e-2	5.2685	1.039313e-3	6.2722
256×256	2.603452	2.0725	2.048553e-3	3.9658	1.395774e-5	6.2184
512×512	6.781712e-1	1.9407	1.277844e-4	4.0028	2.125559e-7	6.0371
1024×1024	1.448771e-1	2.2268	7.718401e-6	4.0493	3.172309e-9	6.0662

Table 3.4: Grid convergence for the wavenumber $k = 12.8$ and the dimension of the basis (2.38) $M = 66$.

$R = 3$. On the other hand, we also see in Tables 3.1 through 3.5 that the accuracy actually achieved on the grid is often orders of magnitude less than the machine precision. This indicates that the chosen M may be superfluous, and the same accuracy of the solution can be obtained using a smaller basis (2.38) at a lower computational cost. For example, the fourth and sixth order computations presented in Table 3.5 ($k = 25.6$) were repeated for various values of M with similar results. From Tables 3.6 and 3.7 one learns that for the finest grids the higher accuracy reached with the large value of M degrades when the value of M decreased more

then 20 percent. This result is not surprising since Fourier series were cut at 10^{-2} and 10^{-3} for $M = 90$ and $M = 85$ respectively.

Grid	Scheme					
	2nd order ctr. difference		4th order compact		6th order compact	
	$\|u - u_{num}\|_\infty$	rate	$\|\|u - u_{num}\|\|_\infty$	rate	$\|\|u - u_{num}\|\|_\infty$	rate
16×16	1.144291e+2	—	2.065713e+3	—	1.175546e+4	—
32×32	4.851901e+1	1.2378	8.885777e+1	4.5390	4.453015e+1	8.0443
64×64	1.280298e+1	1.9221	2.818431	4.9785	1.219721e+1	1.8682
128×128	1.901798e+1	-0.5709	4.128656e-1	2.7711	1.039313e-3	5.5781
256×256	1.448009e+1	0.3933	1.737760e-1	1.2484	1.973019e-3	7.0158
512×512	4.563927	1.6657	4.317500e-3	5.3309	2.883989e-5	6.0962
1024×1024	3.892365	0.2296	2.603055e-4	4.0519	4.398634e-7	6.0349

Table 3.5: Grid convergence for the wavenumber $k = 25.6$ and the dimension of the basis (2.38) $M = 111$.

Grid	M			
	111	100	90	85
	$\|\|u - u_{num}\|\|_\infty$	$\|\|u - u_{num}\|\|_\infty$	$\|\|u - u_{num}\|\|_\infty$	$\|\|u - u_{num}\|\|_\infty$
16×16	2.065713e+3	2.253702e+3	2.222923e+3	2.222930e+3
32×32	8.885777e+1	6.484520e+1	6.827580e+1	5.631450e+1
64×64	2.818431	2.813891	2.503964	2.192968e+0
128×128	4.128656e-1	4.070042e-1	4.048406e-1	4.057072e-1
256×256	1.737760e-1	1.735016e-1	1.733309e-1	1.734153e-1
512×512	4.317500e-3	4.317889e-3	4.317991e-3	1.220778e-2
1024×1024	2.603055e-4	2.603074e-4	5.893227e-4	1.066776e-2

Table 3.6: Behavior of the schemes for various dimensions of the basis (2.38) M – 4th order compact scheme. The wavenumber is $k = 25.6$.

Grid	M			
	111	100	90	85
	$\|\|u - u_{num}\|\|_\infty$	$\|\|u - u_{num}\|\|_\infty$	$\|\|u - u_{num}\|\|_\infty$	$\|\|u - u_{num}\|\|_\infty$
16×16	1.175546e+4	1.352850e+4	1.276175e+4	1.237621e+4
32×32	4.453015e+1	4.953919e+1	4.407588e+1	4.927018e+1
64×64	1.219721e+1	7.862976	7.118779	6.783102
128×128	1.039313e-3	2.549135e-1	2.530015e-1	2.529428e-1
256×256	1.973019e-3	1.973351e-3	1.971636e-3	1.491697e-2
512×512	2.883989e-5	2.884148e-5	6.756577e-4	1.194734e-2
1024×1024	4.398634e-7	4.882227e-7	5.914269e-4	1.065307e-2

Table 3.7: Behavior of the schemes for various dimensions of the basis (2.38) M – 6th order compact scheme. The wavenumber is $k = 25.6$.

Grid	Scheme					
	2nd order ctr. difference		4th order compact		6th order compact	
	$\|u - \mathfrak{u}_{\text{num}}\|_\infty$	rate	$\|\|u - \mathfrak{u}_{\text{num}}\|\|_\infty$	rate	$\|\|u - \mathfrak{u}_{\text{num}}\|\|_\infty$	rate
16×16	3.752407	—	2.907471e-1	—	7.342967e-2	—
32×32	2.290364e-1	4.0342	1.010567e-2	4.8465	1.432143e-4	9.0020
64×64	6.503502e-2	1.8163	8.516129e-4	3.5688	3.976092e-6	5.1707
128×128	1.990979e-2	1.7077	7.105160e-5	3.5833	9.373316e-8	5.4066
256×256	5.743664e-3	1.7934	4.898880e-6	3.8583	1.693751e-9	5.7903
512×512	2.130201e-3	1.4310	3.736573e-7	3.7127	3.099734e-11	5.7719
1024×1024	4.835611e-4	2.1392	2.310974e-8	4.0151	7.720891e-12	2.0053

Table 3.8: The deterioration in grid convergence for the wavenumber $k=3$ and the dimension of the basis (2.38) $M=28$ when $n-1$ degree Taylor extension used.

Previously, in Section 2.3.1.2 we claimed that in order to obtain n^{th} order approximation to the original problem one needs Equation Based Taylor extension of n^{th} degree. Thus, we note that all the computations presented in Tables 3.1 – 3.5 and in Tables 3.6, 3.7 were conducted using a n^{th} degree Equation Based Taylor extension. Theoretically, the degree of Taylor extension were predicted to be $n+2$, see [47]. To see whether or not our current (lower) choice of Taylor's order can be improved further, we have conducted similar computations, but for an even smaller, $n-1$, degree of Taylor extension. In Table 3.8, we present the results for $k=3$. The data show a certain deterioration of the convergence rate (cf. Table 3.2), which indicates that the number of terms in the equation-based extension formulae should not be taken any lower than the order of accuracy n of the scheme (i.e. n^{th} degree Taylor extension).

3.1.2 Variable wavenumber Helmholtz equation with fourth order accuracy

We now use the fourth order accurate compact scheme (1.8) to solve the inhomogeneous Helmholtz equation (1.1) with a variable wavenumber inside the circles and ellipses, subject to Dirichlet or Neumann boundary conditions. The goal of the computations is to demonstrate the capability of the proposed method to address variable coefficients and various types of the boundary conditions, and again, to show the design order of grid convergence for non-conforming boundaries (the discretization grid is always Cartesian). The domain Ω_1 is either a disk of radius $R = 1$ centered at the origin, or the interior of the ellipse with the major semi-axis $a = 1$ and minor semi-axis $b = 1/2$, see formula (1.5).

The Helmholtz equation (1.1) that we solve on the domain Ω_1 has a variable wavenumber k. For the case of the disk we choose

$$k = k_0 e^{-10(r-r_0)^6 r^6 \cos\theta}, \tag{3.4}$$

and for the case of the ellipse we take

$$k = k_0 e^{-10(r-r_0)^6 r^6}, \tag{3.5}$$

where r is the polar radius and θ is the polar angle and the parameter $r_0 = 1.6$. The profiles of k are schematically shown in Figure 3.2.

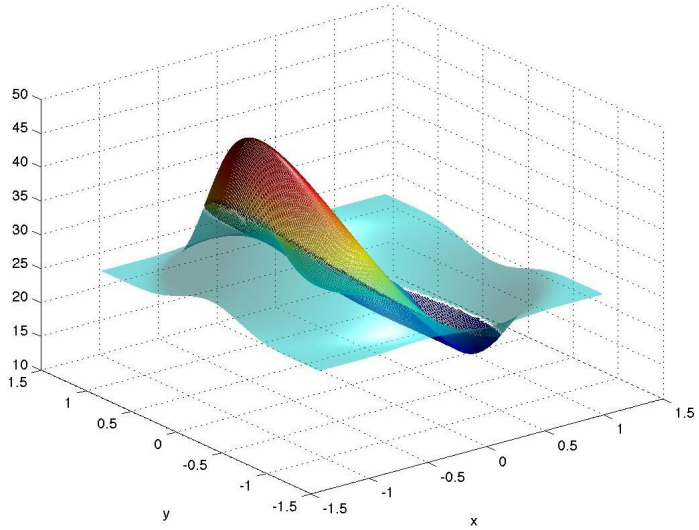

(a) Ω_1 is a circle, formula (3.4)

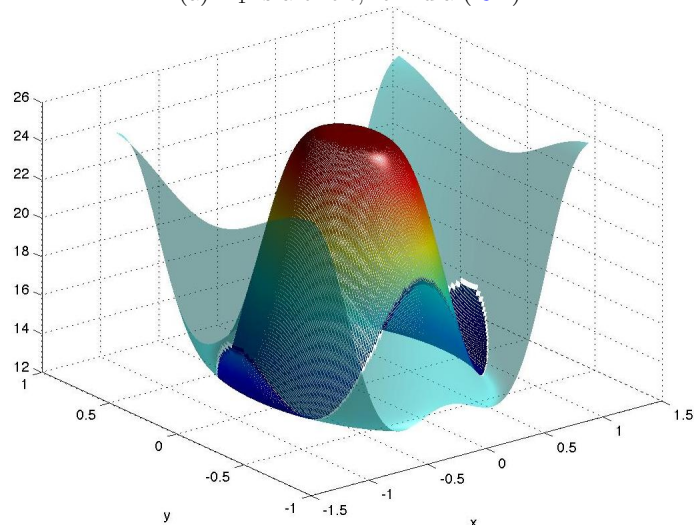

(b) Ω_1 is an ellipse, formula (3.5)

Figure 3.2: Profiles of the variable wavenumber k on Ω_0 for $k_0 = 25$; the part inside Ω_1 is emphasized.

In either case, circle or ellipse, the exact solution is chosen in the form:

$$u = e^{ikx}. \tag{3.6}$$

Since k is variable, see formulae (3.4) and (3.5), this solution is not a plane wave, as shown in Figure 3.3 and 3.4. The corresponding right-hand side $f(x, y)$ in formula (1.1) is obtained by backward engineering, i.e., by substituting u given by (3.6) into the left-hand side of the Helmholtz equation.

The boundary condition at $\Gamma = \partial\Omega_1$ for the Helmholtz equation (1.1) can be of either Dirichlet or Neumann type. The required boundary data are also obtained by backward engineering, i.e., by taking the trace of either the solution u itself or its normal derivative $\frac{\partial u}{\partial n}$ at the boundary Γ.

When Ω_1 is a disk of radius $R = 1$, the AP (see 2.33) is formulated on the square

$$\Omega_0 = \{(x, y) \mid -1.2 \leqslant x,\, y \leqslant 1.2\}$$

with the following boundary conditions: $v = 0$ at $y = \pm 1.2$,and

$$\frac{dv}{dx} + iv = 0 \text{ at } x = 1.2 \quad \text{and} \quad \frac{dv}{dx} - iv = 0 \text{ at } x = -1.2. \tag{3.7}$$

The pair of complex boundary conditions (3.7) guarantees that regardless of k there will be no resonances in the solution of the AP on the square Ω_0.

In the case of the ellipse, the AP is formulated on the rectangle

$$\Omega_0 = \{(x, y) \mid -1.2 \leqslant x \leqslant 1.2,\ -0.7 \leqslant y \leqslant 0.7\}$$

with the boundary conditions:

$$v = 0 \text{ at } y = \pm 0.7,$$

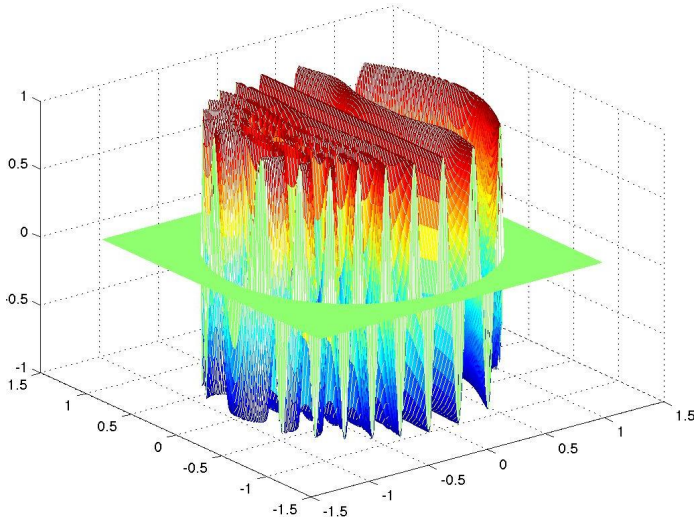

(a) Real part

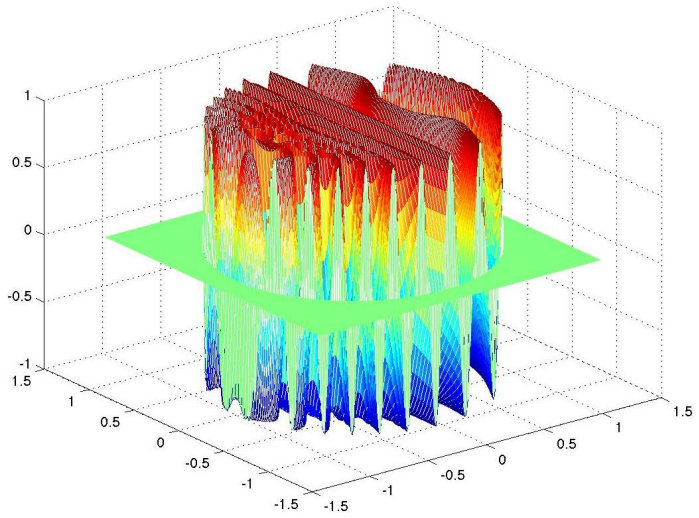

(b) Imaginary part

Figure 3.3: Real and Imaginary part of the test solution (3.6) in circle for $k_0 = 25$.

and the same complex boundary conditions (3.7) at $x = \pm 1.2$.

Similar to Section 3.1.1, the AP is discretized on a sequence of uniform, in each direction, Cartesian grids of dimension $2^d \times 2^d$, with a maximum of 2048×2048.

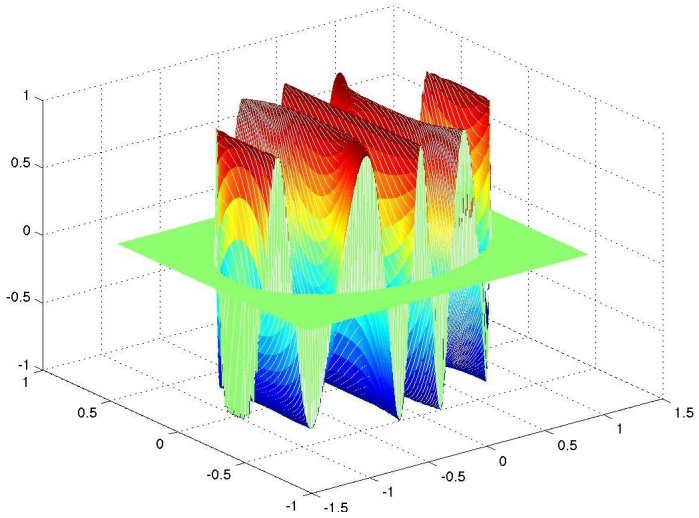

(a) Real Part

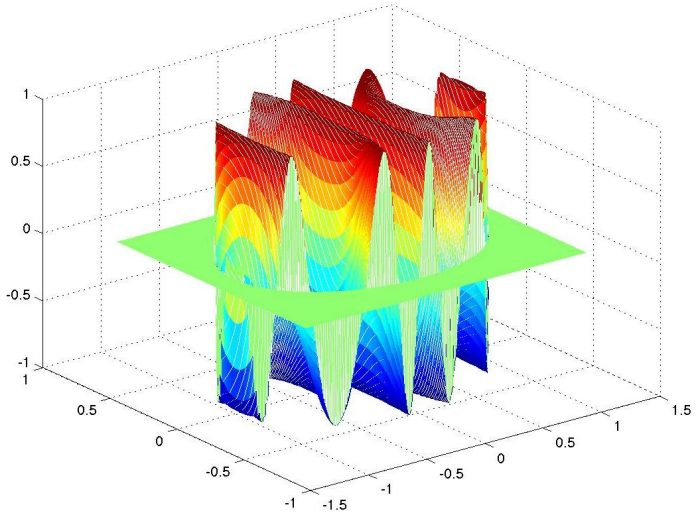

(b) Imaginary Part

Figure 3.4: Real and Imaginary part of the test solution (3.6) in ellipse for $k_0 = 25$.

For a given d, the grid size in the case of a square is $h = \frac{2.4}{2^d}$, and the grid sizes in the case of a rectangle are $h_x = \frac{2.4}{2^d}$ and $h_y = \frac{1.4}{2^d}$. The grid sizes are halved every time d is incremented by 1, which is convenient for studying the convergence. As in

Section 3.1.1, the AP is also solved by the sparse LU decomposition.

Numerical results for solving the Dirichlet problem for the variable coefficient Helmholtz equation (1.1) are presented in Table 3.9 in the case of a circle and in Table 3.10 in the case of an ellipse of an aspect ratio $AR = 2$ for the range of k's that we have investigated, k_0= 5, 15, and 25. In Table 3.11 we fix the wavenumber to be k_0= 10 and vary the aspect ratio of an ellipse for the values $AR = 2$, 4 and 8. Ellipses with even higher AR are presented in later sections. We stress that the data in the tables fully corroborate the design fourth order rate of grid convergence for the compact Cartesian scheme (1.8) when the non-conforming boundaries are handled by the method of difference potentials.

Similar numerical results for the Neumann problem are presented in Table 3.12 for the circle, in Table 3.13 for the ellipse, and in Table 3.14 for ellipses with different aspect ratios. As with the Dirichlet problem, the data in the tables fully corroborate the design fourth order rate of grid convergence of the proposed methodology.

Grid	Circle					
	$k_0 = 5$, $M = 42$		$k_0 = 15$, $M = 54$		$k_0 = 25$, $M = 67$	
	$\|\|u - \mathfrak{u}_{\text{num}}\|\|_\infty$	rate	$\|\|u - \mathfrak{u}_{\text{num}}\|\|_\infty$	rate	$\|\|u - \mathfrak{u}_{\text{num}}\|\|_\infty$	rate
16×16	3.038830	—	1.517016e+1	—	1.571341e+2	—
32×32	2.231693e-2	7.0892	3.324707	5.5119	1.304138e+1	3.5908
64×64	1.405180e-3	3.9893	1.032080e-1	5.0096	2.744285	2.2486
128×128	7.302520e-5	4.2662	5.746378e-3	4.1668	5.751020e-2	5.5765
256×256	4.465171e-6	4.0316	3.454849e-4	4.0560	3.678247e-3	3.9667
512×512	2.701632e-7	4.0468	2.125100e-5	4.0230	2.265488e-4	4.0211
1024×1024	1.680068e-8	4.0072	1.321587e-6	4.0072	1.405292e-5	4.0109
2048×2048	1.040726e-9	4.0129	8.239623e-8	4.0035	8.745530e-7	4.0062

Table 3.9: Grid convergence of the solution to the Dirichlet problem for the circle $R = 1$. Variable coefficient Helmholtz equation (1.1) and a fourth order compact scheme (1.8).

Grid	Ellipse					
	$k_0 = 5,\ M = 42$		$k_0 = 15,\ M = 54$		$k_0 = 25,\ M = 67$	
	$\|\|u - \mathfrak{u}_{\text{num}}\|\|_\infty$	rate	$\|\|u - \mathfrak{u}_{\text{num}}\|\|_\infty$	rate	$\|\|u - \mathfrak{u}_{\text{num}}\|\|_\infty$	rate
16×16	8.283939	—	3.950658e+1	—	5.206655e+1	—
32×32	1.978583e-2	8.7097	6.015599e-1	6.0372	3.388063e+1	0.6199
64×64	3.104902e-4	5.9938	7.001777e-3	6.4248	8.662025e-2	8.6115
128×128	1.659692e-5	4.2256	7.492233e-4	3.2243	5.811711e-3	3.8977
256×256	5.597237e-7	4.8901	2.551093e-5	4.8762	3.104959e-4	4.2263
512×512	2.094249e-8	4.7402	1.551669e-6	4.0392	1.881038e-5	4.0450
1024×1024	6.565249e-10	4.9954	9.538440e-8	4.0239	1.160326e-6	4.0189
2048×2048	2.761463e-11	4.5713	5.897927e-9	4.0155	7.200706e-8	4.0102

Table 3.10: Grid convergence of the solution to the Dirichlet problem for the ellipse $a=1$, $b=\frac{1}{2}$. Variable coefficient Helmholtz equation (1.1) and a fourth order compact scheme (1.8).

Grid	$M = 54,\ AR = 2$		$M = 72,\ AR = 4$		$M = 98,\ AR = 8$	
	$\|\|\mathfrak{u}^h - \mathfrak{u}^{2h}\|\|_\infty$	rate	$\|\|\mathfrak{u}^h - \mathfrak{u}^{2h}\|\|_\infty$	rate	$\|\|\mathfrak{u}^h - \mathfrak{u}^{2h}\|\|_\infty$	rate
16×16	3.707995e+1	—	6.563552 e+2	—	3.514365e+2	—
32×32	1.678518e-1	7.7873	3.475799 e+2	0.9171	4.113777e+4	-6.8711
64×64	1.771571e-3	6.5660	2.900153 e+3	-3.0607	1.338930e+1	1.5852
128×128	1.915687e-4	3.2091	2.715441 e-4	23.3484	1.148908e+2	-3.1011
256×256	5.270431e-6	5.1838	1.038533 e-5	4.7086	2.092065e-3	15.7450
512×512	2.157025e-7	4.6108	8.242304 e-7	3.6554	1.650560e-6	10.3078
1024×1024	1.315849e-8	4.0350	2.520539 e-8	5.0312	7.926636e-8	4.3801
2048×2048	7.490176e-10	4.1349	6.660874 e-10	5.2419	6.770679e-9	3.5493

Table 3.11: Grid convergence of the solution to the Dirichlet problem for the wavenumber $k=10$ and the ellipses $a=1$, $b \in \{\frac{1}{2}, \frac{1}{4}, \frac{1}{8}\}$. Variable coefficient Helmholtz equation (1.1) and a fourth order compact scheme (1.8).

Grid	Ellipse					
	$k_0 = 5,\ M = 42$		$k_0 = 15,\ M = 54$		$k_0 = 25,\ M = 67$	
	$\|\|u - \mathfrak{u}_{\text{num}}\|\|_\infty$	rate	$\|\|u - \mathfrak{u}_{\text{num}}\|\|_\infty$	rate	$\|\|u - \mathfrak{u}_{\text{num}}\|\|_\infty$	rate
16×16	4.267776e+1	—	1.772119e+2	—	3.649132e+2	—
32×32	9.712126e-2	8.7795	2.316084	6.2576	3.309569e+1	3.4628
64×64	7.548180e-3	3.6856	6.203786e-2	5.2224	1.573478e-2	7.7165
128×128	4.486249e-4	4.0725	4.713176e-3	3.7184	1.589413e-3	3.3074
256×256	2.486193e-5	4.1735	2.419222e-4	4.2841	6.383346e-4	4.6380
512×512	1.372890e-6	4.1787	1.635393e-5	3.8868	4.329843e-5	3.8819
1024×1024	9.028545e-8	3.9266	9.750050e-7	4.0681	2.425497e-6	4.1580
2048×2048	5.198146e-9	4.1184	6.308512e-8	3.9500	1.584606e-8	3.9361

Table 3.13: Grid convergence of the solution to the Neumann problem for the ellipse $a=1$, $b=\frac{1}{2}$. Variable coefficient Helmholtz equation (1.1) and a fourth order compact scheme (1.8).

Grid	Circle					
	$k_0 = 5,\ M = 42$		$k_0 = 15,\ M = 54$		$k_0 = 25,\ M = 67$	
	$\|\|u - \mathfrak{u}_{\text{num}}\|\|_\infty$	rate	$\|\|u - \mathfrak{u}_{\text{num}}\|\|_\infty$	rate	$\|\|u - \mathfrak{u}_{\text{num}}\|\|_\infty$	rate
16×16	1.188942	—	8.839874e+1	—	1.713283e+2	—
32×32	1.801846e-2	6.0441	6.391570e+1	5.5119	7.346974e+1	1.2215
64×64	1.245872e-3	3.8542	3.179250e-1	5.0096	2.938586	4.6440
128×128	5.731111e-5	4.4422	3.336937e-2	4.1668	4.978325e-2	5.8833
256×256	4.343596e-6	3.7219	2.037841e-3	4.0560	2.970674e-3	4.0668
512×512	2.118921e-7	4.3575	1.218354e-4	4.0230	1.810039e-4	4.0367
1024×1024	1.467516e-8	3.8519	7.567901e-6	4.0072	1.144116e-5	3.9837
2048×2048	8.996365e-10	4.0279	4.647261e-7	4.0035	7.144455e-7	4.0013

Table 3.12: Grid convergence of the solution to the Neumann problem for the circle $R=1$. Variable coefficient Helmholtz equation (1.1) and a fourth order compact scheme (1.8).

Grid	$M = 54,\ AR = 2$		$M = 72,\ AR = 4$		$M = 98,\ AR = 8$	
	$\|\|\mathfrak{u}^h - \mathfrak{u}^{2h}\|\|_\infty$	rate	$\|\|\mathfrak{u}^h - \mathfrak{u}^{2h}\|\|_\infty$	rate	$\|\|\mathfrak{u}^h - \mathfrak{u}^{2h}\|\|_\infty$	rate
16×16	1.118772e+2	—	5.034143e+3	—	2.361988e+4	—
32×32	4.950664e-1	7.8201	1.350765e+4	-1.4240	2.316460e+5	-3.2938
64×64	9.400937e-3	5.7187	6.645722e+1	7.6671	1.798778e+1	13.6526
128×128	7.042638e-4	3.7386	2.195422e-3	14.8856	5.980095e+1	-1.7332
256×256	3.226175e-5	4.4482	1.562795e-4	3.8123	3.296630e-2	10.8250
512×512	2.080956e-6	3.9545	1.028099e-5	3.9261	4.720918e-5	9.4477
1024×1024	1.202756e-7	4.1128	5.577696e-7	4.2042	3.309864e-6	3.8342
2048×2048	7.788341e-9	3.9489	3.868259e-8	3.8499	2.209241e-7	3.9051

Table 3.14: Grid convergence of the solution to the Neumann problem for the wavenumber $k=10$ and the ellipses $a=1$, $b \in \{\frac{1}{2}, \frac{1}{4}, \frac{1}{8}\}$. Variable coefficient Helmholtz equation (1.1) and a fourth order compact scheme (1.8).

3.2 Exterior scattering problems

We next consider the scattering of an incoming plane wave with a given frequency (wavelength) and given angle of incidence off an elliptical body with a given aspect ratio. In our simulations, we take the major semi-axis of the ellipse to be $a = 1.8$, while its minor semi-axis varies between $b = 0.9$ and $b = 0.18$, which yields aspect

ratios between 2 and 10. The wavenumber in the Helmholtz equation (1.2a) varies between $k_0 = 1$ and $k_0 = 25$, which yields the variation of the wavelength between $\lambda_0 = 2\pi$ and $\lambda_0 = 2\pi/25$, i.e., between roughly twice the size $2a$ of the ellipse and about 8% of this size. We consider several values of the angle of incidence between 0° and 50° with respect to the direction of the major axis. We also consider both Dirichlet and Neumann boundary conditions at the contour Γ, i.e., at the perimeter of the ellipse. In the context of acoustics, the former corresponds to sound-soft scattering, whereas the latter corresponds to sound-hard scattering. The exterior AP is solved on the domain Ω_1 shaped as an annulus, $\Omega_1 = \{R_0 \leqslant r \leqslant R_1\}$, see Figure 2.4, with R_0 that may vary between 0.1 (for larger aspect ratios) and 0.3 (for smaller aspect ratios), and $R_1 = 2$. This AP is discretized on a uniform, in each direction, polar grid that may have between 64×64 and 4096×4096 cells. The quantity M that represents the dimension of the basis on Γ, see formula (2.38), is grid-independent and chosen so as to guarantee that the given boundary data (Dirichlet or Neumann) are approximated by the corresponding finite Fourier series up to the machine precision. The problem is solved using the simplified methodology of Section 2.3.6. In doing so, the discrete exterior AP is integrated by means of the separation of variables combined with a FFT. The exact nonlocal ABC at the outer circle $r = R_1$ is conveniently set in the Fourier space, see [8].

As the overall set of results for all wavenumbers, incidence angles, aspect ratios, etc., is rather large, we have chosen to show only a representative sample. In Figures 3.5 and 3.6, we show the schematic geometry for two ellipses — of aspect ratio 2 and of aspect ratio 10 (cf. Figure 2.4).

To assess the grid convergence, we do not evaluate the exact solution using its

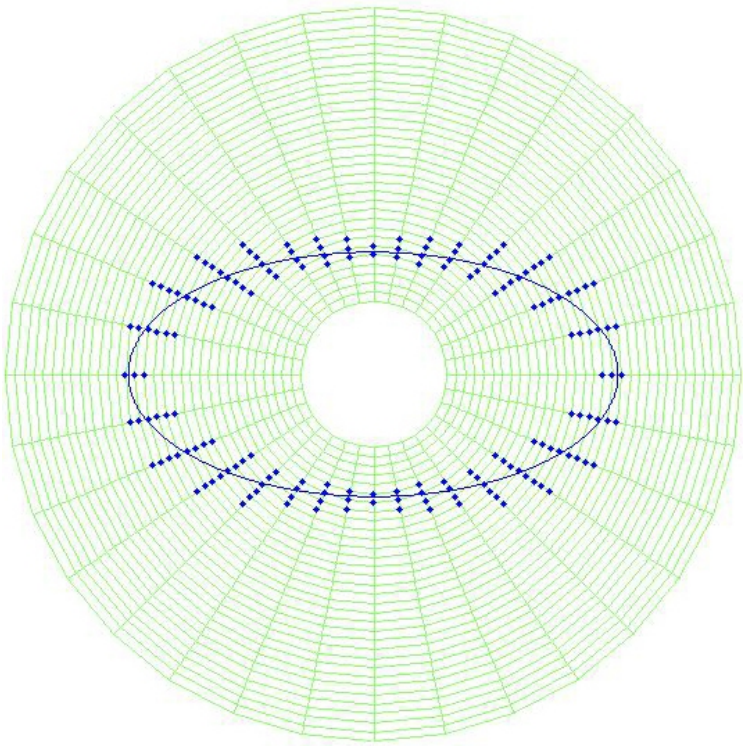

Figure 3.5: Schematic of the polar grid for the exterior AP, the elliptic scatterer of aspect ratio 2, and the grid boundary γ.

expansion with respect to Mathieu functions [6], because this may entail numerical difficulties of its own. We rather evaluate the infinity norm of the difference between the numerical solutions obtained on two consecutive grids, $\mathfrak{u}^h$ and $\mathfrak{u}^{2h}$.

Tables 3.15 through 3.22 demonstrate the design fourth order rate of the grid convergence for the case of a Dirichlet boundary condition on Γ. We note that the convergence on coarser grids looks somewhat more "erratic" for slenderer ellipses. This is likely accounted for by insufficient grid resolution in the areas of high curvature, i.e., near the tips of the major axis. Nonetheless, on finer grids the convergence rate approaches its correct asymptotic value of 4. Similar results are obtained for

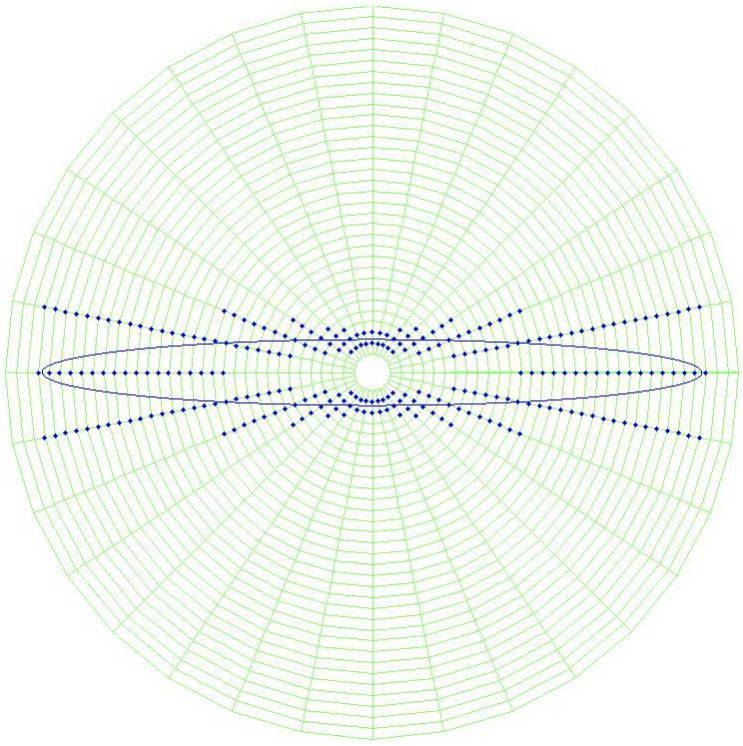

Figure 3.6: Schematic of the polar grid for the exterior AP, the elliptic scatterer of aspect ratio 10, and the grid boundary γ.

the Neumann boundary condition on Γ, see Tables 3.24 and 3.25, as well as for a variety of other Dirichlet and Neumann cases that are not presented in these tables.

Grid	$k_0 = 1$, $M = 12$		$k_0 = 10$, $M = 37$		$k_0 = 25$, $M = 69$	
	$\|\|u^h - u^{2h}\|\|_\infty$	rate	$\|\|u^h - u^{2h}\|\|_\infty$	rate	$\|\|u^h - u^{2h}\|\|_\infty$	rate
64×64	2.737716ee-3	—	6.104800	—	3.945149e+1	—
128×128	3.658040ee-4	2.9038	6.761083e-2	6.4965	1.020563e+2	-1.3712
256×256	2.075372ee-5	4.1396	3.888347e-3	4.1200	3.843873e-1	8.0526
512×512	1.134933ee-6	4.1927	2.382304e-4	4.0287	2.189631e-2	4.1338
1024×1024	6.890566ee-8	4.0418	1.481515e-5	4.0072	1.329834e-3	4.0414
2048×2048	4.235718ee-9	4.0239	9.247807e-7	4.0018	8.251120e-5	4.0105
4096×4096	2.637849ee-10	4.0052	5.778413e-8	4.0004	5.147419e-6	4.0027

Table 3.15: Sound-soft scattering of a plane wave with incidence angle 0° about an ellipse with aspect ratio 2.

Grid	$k_0 = 1$, $M = 12$		$k_0 = 10$, $M = 37$		$k_0 = 25$, $M = 69$	
	$\|\|u^h - u^{2h}\|\|_\infty$	rate	$\|\|u^h - u^{2h}\|\|_\infty$	rate	$\|\|u^h - u^{2h}\|\|_\infty$	rate
64×64	2.924441e-3	—	1.399531	—	1.588919e+1	—
128×128	3.686772e-4	2.9877	9.024242e-2	3.9550	2.571935e+1	-0.6948
256×256	2.092322e-5	4.1392	5.042251e-3	4.1617	4.528627e-1	5.8276
512×512	1.140182e-6	4.1978	3.077507e-4	4.0342	2.614107e-2	4.1147
1024×1024	7.045679e-8	4.0164	1.912254e-5	4.0084	1.576210e-3	4.0518
2048×2048	4.352290e-9	4.0169	1.193405e-6	4.0021	9.766250e-5	4.0125
4096×4096	2.708936e-10	4.0060	7.456103e-8	4.0005	6.090803e-6	4.0031

Table 3.16: Sound-soft scattering of a plane wave with incidence angle 35° about an ellipse with aspect ratio 2.

Grid	$k_0 = 1$, $M = 12$		$k_0 = 10$, $M = 37$		$k_0 = 25$, $M = 69$	
	$\|\|u^h - u^{2h}\|\|_\infty$	rate	$\|\|u^h - u^{2h}\|\|_\infty$	rate	$\|\|u^h - u^{2h}\|\|_\infty$	rate
64×64	3.647013e-2	—	6.942957	—	6.094755e+5	—
128×128	3.229204e-3	3.4975	1.556797e-1	5.4789	8.271102	16.1691
256×256	5.948035e-4	2.4407	5.275428e-3	4.8831	4.000126e-1	4.3700
512×512	2.733103e-5	4.4438	2.869505e-4	4.2004	2.340879e-2	4.0949
1024×1024	1.429272e-6	4.2572	1.782570e-5	4.0088	1.410523e-3	4.0527
2048×2048	8.252679e-8	4.1143	1.112633e-6	4.0019	8.738691e-5	4.0127
4096×4096	5.198425e-9	3.9887	6.951841e-8	4.0004	5.449762e-6	4.0032

Table 3.17: Sound-soft scattering of a plane wave with incidence angle 35° about an ellipse with aspect ratio 3.

Grid	$k_0 = 1$, $M = 12$		$k_0 = 10$, $M = 37$		$k_0 = 25$, $M = 69$	
	$\|\|u^h - u^{2h}\|\|_\infty$	rate	$\|\|u^h - u^{2h}\|\|_\infty$	rate	$\|\|u^h - u^{2h}\|\|_\infty$	rate
64×64	2.261699e-2	—	5.730228	—	1.742757e+3	—
128×128	3.149537e-3	2.8442	9.782407e-2	5.8723	9.548658	7.5119
256×256	6.271734e-4	2.3282	4.605138e-3	4.4089	2.276872	2.0682
512×512	2.917059e-5	4.4263	2.738948e-4	4.0716	2.445093e-2	6.5410
1024×1024	1.537777e-6	4.2456	1.701433e-5	4.0088	1.483170e-3	4.0431
2048×2048	8.870759e-8	4.1156	1.061794e-6	4.0022	9.201076e-5	4.0107
4096×4096	5.523241e-9	4.0055	6.633567e-8	4.0006	5.739903e-6	4.0027

Table 3.18: Sound-soft scattering of a plane wave with incidence angle 15° about an ellipse with aspect ratio 3.

Grid	$k_0 = 1$, $M = 13$		$k_0 = 10$, $M = 39$		$k_0 = 25$, $M = 73$	
	$\|\|u^h - u^{2h}\|\|_\infty$	rate	$\|\|u^h - u^{2h}\|\|_\infty$	rate	$\|\|u^h - u^{2h}\|\|_\infty$	rate
64×64	7.024091e+1	—	1.800415e+3	—	1.189542e+7	—
128×128	1.117795e+1	2.6517	1.080259e+1	7.3808	2.905446e+3	11.9994
256×256	8.069814e-3	10.4358	5.008329e-2	7.7528	6.346536e-1	12.1605
512×512	1.523137e-3	2.4055	5.161442e-3	3.2785	2.456628e-2	4.6912
1024×1024	7.604331e-5	4.3241	4.003719e-4	3.6884	1.471074e-3	4.0617
2048×2048	3.763327e-6	4.3367	1.942630e-5	4.3653	9.124847e-5	4.0109
4096×4096	2.072289e-7	4.1827	1.066348e-6	4.1873	5.691707e-6	4.0029

Table 3.19: Sound-soft scattering of a plane wave with incidence angle 15° about an ellipse with aspect ratio 5.

Grid	$k_0 = 1$, $M = 13$		$k_0 = 10$, $M = 39$		$k_0 = 25$, $M = 73$	
	$\|\|u^h - u^{2h}\|\|_\infty$	rate	$\|\|u^h - u^{2h}\|\|_\infty$	rate	$\|\|u^h - u^{2h}\|\|_\infty$	rate
64×64	7.754767e+1	—	1.618151e+3	—	2.224965e+4	—
128×128	1.489596e+1	2.3802	4.674100	8.4354	2.185893e+1	9.9913
256×256	1.111821e-2	10.3878	1.362536e-1	5.1003	7.391991e-1	4.8861
512×512	1.435914e-3	2.9529	5.846135e-3	4.5427	5.567719e-2	3.7308
1024×1024	6.645732e-5	4.4334	4.166078e-4	3.8107	1.532545e-3	5.1831
2048×2048	3.288638e-6	4.3369	2.038867e-5	4.3529	9.506068e-5	4.0109
4096×4096	1.804245e-7	4.1880	1.145084e-6	4.1542	5.933124e-6	4.0020

Table 3.20: Sound-soft scattering of a plane wave with incidence angle 50° about an ellipse with aspect ratio 5.

Grid	$k_0 = 1$, $M = 11$		$k_0 = 10$, $M = 32$		$k_0 = 25$, $M = 56$	
	$\|\|u^h - u^{2h}\|\|_\infty$	rate	$\|\|u^h - u^{2h}\|\|_\infty$	rate	$\|\|u^h - u^{2h}\|\|_\infty$	rate
64×64	2.247929e+2	—	4.633311e+3	—	1.553633e+5	—
128×128	5.212738e+2	-1.2134	4.70154e+2	3.3008	1.547453e+5	0.0057
256×256	8.031341e+2	-0.6236	4.419326e+2	0.0893	8.284062e+3	7.5453
512×512	1.195681e-2	16.0355	4.052018e-1	10.0910	9.340049e-1	9.7927
1024×1024	4.655482e-3	1.3608	2.785232e-2	3.8628	8.518332e-2	3.4548
2048×2048	5.918121e-4	2.9757	1.895585e-3	3.8771	2.569198e-3	5.0512
4096×4096	2.142775e-5	4.7876	8.621134e-5	4.4586	1.937799e-4	3.7288

Table 3.21: Sound-soft scattering of a plane wave with incidence angle 50° about an ellipse with aspect ratio 10.

Grid	$k_0 = 1$, $M = 13$		$k_0 = 10$, $M = 39$		$k_0 = 25$, $M = 73$	
	$\|\|u^h - u^{2h}\|\|_\infty$	rate	$\|\|u^h - u^{2h}\|\|_\infty$	rate	$\|\|u^h - u^{2h}\|\|_\infty$	rate
64×64	2.448706e+2	—	2.323499 e+4	—	2.151660e+7	—
128×128	4.433401e+2	-0.8564	1.156875e+4	1.0061	3.572665e+6	2.5904
256×256	6.193218e+2	-0.4823	2.889933e+2	5.3231	1.535344e+4	7.8623
512×512	1.050433e-2	15.8474	1.251498e-1	11.1732	4.447023e-1	15.0754
1024×1024	5.264725e-3	0.9966	1.706648e-2	2.8744	3.105638e-2	3.8399
2048×2048	6.643254e-4	2.9864	1.993312e-3	3.0979	1.968995e-3	3.9794
4096×4096	2.408868e-5	4.7855	1.040010e-4	4.2605	2.088858e-4	3.2367

Table 3.22: Sound-soft scattering of a plane wave with incidence angle 50° about an ellipse with aspect ratio 10.

Grid	$k_0 = 1$, $M = 13$		$k_0 = 10$, $M = 35$		$k_0 = 25$, $M = 61$	
	$\|\|u^h - u^{2h}\|\|_\infty$	rate	$\|\|u^h - u^{2h}\|\|_\infty$	rate	$\|\|u^h - u^{2h}\|\|_\infty$	rate
64×64	1.181451e-2	—	1.316527 e+1	—	1.879091e+2	—
128×128	3.146854e-4	5.2305	5.405421e-1	4.6062	7.405706e+1	1.3433
256×256	1.566558e-5	4.3282	4.087686e-3	7.0470	3.811382e-1	7.6022
512×512	1.011771e-6	3.9526	2.520713e-4	4.0194	2.007000e-2	4.2472
1024×1024	6.381159e-8	3.9869	1.567661e-5	4.0071	1.242483e-3	4.0137
2048×2048	4.023256e-9	3.9874	9.784086e-7	4.0020	7.724207e-5	4.0077
4096×4096	2.545110e-10	3.9826	6.104984e-8	4.0024	4.834473e-6	3.9980

Table 3.23: Sound-hard scattering of a plane wave with incidence angle 50° about an ellipse with aspect ratio 2.

Grid	$k_0 = 1$, $M = 14$		$k_0 = 10$, $M = 43$		$k_0 = 25$, $M = 79$	
	$\|\|u^h - u^{2h}\|\|_\infty$	rate	$\|\|u^h - u^{2h}\|\|_\infty$	rate	$\|\|u^h - u^{2h}\|\|_\infty$	rate
64×64	5.859690e-2	—	4.558268	—	1.053224e+2	—
128×128	9.846534e-3	2.5731	1.448027e-1	4.9763	4.461393e+1	1.2392
256×256	1.884702e-4	5.7072	8.659281e-3	4.0637	5.844125e-1	6.2544
512×512	9.615561e-6	4.2928	2.363689e-4	5.1951	2.368270e-2	4.6251
1024×1024	4.412894e-7	4.4456	1.470104e-5	4.0071	1.454638e-3	4.0251
2048×2048	2.845780e-8	3.9548	9.188393e-7	4.0000	9.027833e-5	4.0101
4096×4096	1.589844e-9	4.1619	5.934903e-8	3.9525	5.631228e-6	4.0029

Table 3.24: Sound-hard scattering of a plane wave with incidence angle 0° about an ellipse with aspect ratio 3.

Grid	$k_0 = 1$, $M = 13$		$k_0 = 10$, $M = 35$		$k_0 = 25$, $M = 61$	
	$\|\|\mathrm{u}^h - \mathrm{u}^{2h}\|\|_\infty$	rate	$\|\|\mathrm{u}^h - \mathrm{u}^{2h}\|\|_\infty$	rate	$\|\|\mathrm{u}^h - \mathrm{u}^{2h}\|\|_\infty$	rate
64×64	3.381436	—	5.287685	—	8.812860e+4	—
128×128	1.076195	1.6517	1.602327	1.7225	6.882858e+1	10.3224
256×256	1.593996e-1	2.7552	5.157602e-1	1.6354	2.620046	4.7153
512×512	1.921666e-3	6.3741	9.974005e-3	5.6924	3.826752e-2	6.0973
1024×1024	3.456720e-5	5.7968	2.426475e-4	5.3612	1.628882e-3	4.5542
2048×2048	3.522082e-6	3.2949	1.769029e-5	3.7778	1.062220e-4	3.9387
4096×4096	1.822888e-7	4.2721	9.543673e-7	4.2123	6.264534e-6	4.0837

Table 3.25: Sound-hard scattering of a plane wave with incidence angle 50° about an ellipse with aspect ratio 5.

We also emphasize that the scheme converges with the same design rate for all angles of incidence, all wavenumbers, and all aspect ratios. The actual values of the error may, of course, depend on the specific parameters involved. For example, from Tables 3.16 through 3.25 one can see that as the wavenumber k_0 increases while all other parameters remain the same (the aspect ratio, the grid, etc.), the error also increases (maximum norm evaluated across the domain). On the other hand, the angle of incidence does not affect the convergence rate and does not noticeably affect the actual error either. In Figures 3.7, 3.8 and 3.9 we show the dependence of the error on the angle of incidence for both sound-soft (Dirichlet boundary condition) and sound-hard (Neumann boundary condition) scattering about an ellipse of aspect ratio 3. We see that for both $k_0 = 3$,$k_0 = 15$ and $k_0 = 30$ the error changes by less than a factor of 2 over the entire 90° range.

For the same setting as before, we also conducted a series of computations that corroborate the pollution effect. As mentioned in Section 1.2, to maintain the same level of error for different values of the wavenumber k, the quantity $h^n k^{n+1}$ must remain constant, where h is the grid size and n is the order of accuracy. This means, in particular, that if the grid size h is halved, then the same level of error

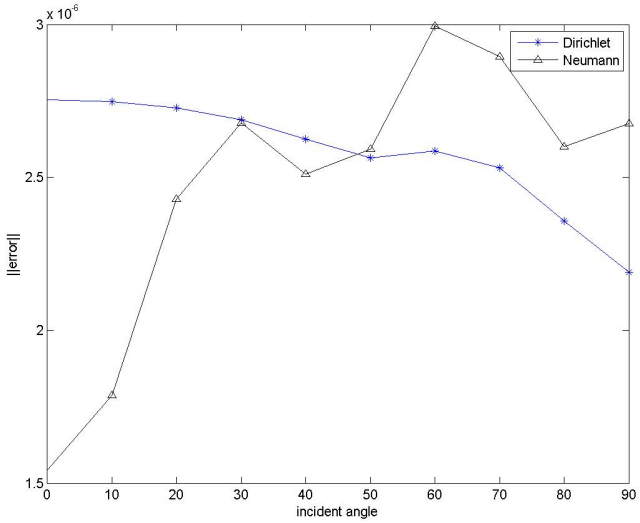

Figure 3.7: Error vs. the angle of incidence for sound-soft (Dirichlet BC) and sound-hard (Neumann BC) scattering about an ellipse with aspect ratio 3 for the wavenumber $k_0 = 3$ and the dimension of the basis (2.38) $M = 21$ computed on the polar grid of dimension 1024×1024.

shall be expected if the wavenumber k increases by a factor of $2^{\frac{n}{n+1}}$. Specifically, the wavenumber k should increase by a factor of $2^{\frac{2}{3}} \approx 1.5874$ for the central difference second order scheme, by a factor of $2^{\frac{4}{5}} \approx 1.7411$ for the fourth order compact scheme (1.8), and by a factor of $2^{\frac{5}{6}} \approx 1.7818$ for the sixth order compact scheme of [56]. We see that this factor is always less than two, which means that the "points-per-wavelength" quantity does not stay constant but rather increases as k grows. However, the higher the accuracy n of the scheme the slower the error increases. In Table 3.26, we summarize the computational data for all three schemes. Specifically, we fix the value of $k = 4$ for the grid of dimension 256×256, and then vary h and change k according to the power law $2^{\frac{n}{n+1}}$ that corresponds to each scheme.

We next perform complexity profiling of the algorithm. We stress that our methodology is naturally very effective for problems with several impinging waves

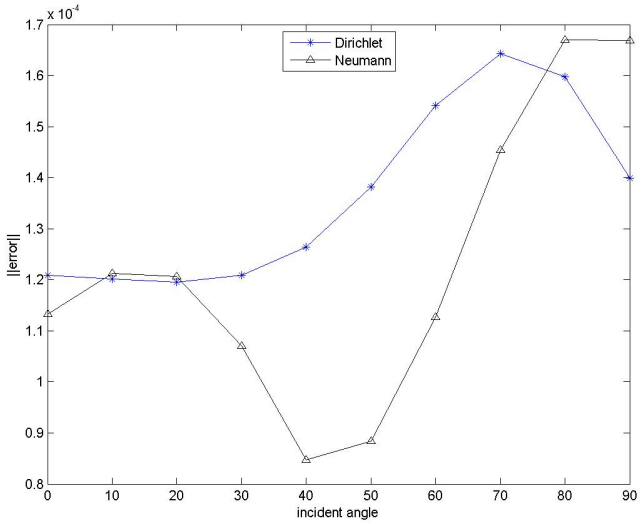

Figure 3.8: Error vs. the angle of incidence for sound-soft (Dirichlet BC) and sound-hard (Neumann BC) scattering about an ellipse with aspect ratio 3 for the wavenumber $k_0 = 15$ and the dimension of the basis (2.38) $M = 52$ computed on the polar grid of dimension 1024×1024.

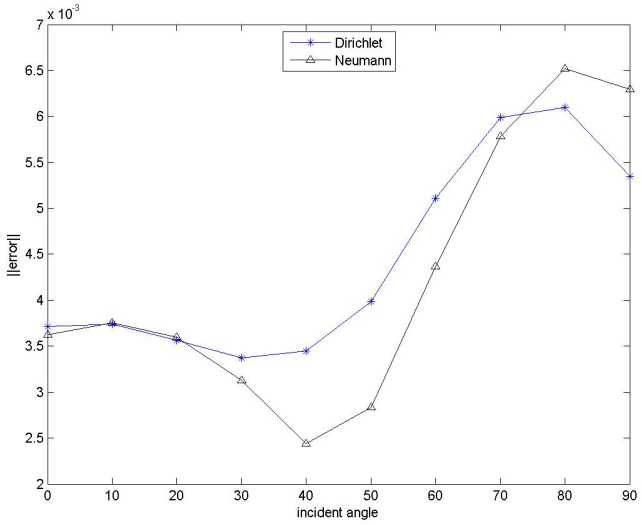

(a) $k_0 = 30$, $M = 86$

Figure 3.9: Error vs. the angle of incidence for sound-soft (Dirichlet BC) and sound-hard (Neumann BC) scattering about an ellipse with aspect ratio 3 for the wavenumber $k_0 = 30$ and the dimension of the basis (2.38) $M = 86$ computed on the polar grid of dimension 1024×1024.

Grid	k	M	Problem	
			Diriclet	Neumann
			$\|\|u^h - u^{2h}\|\|_\infty$	$\|\|u^h - u^{2h}\|\|_\infty$
64×64	1.3195	14	5.088513e-3	1.107942e-3
128×128	2.2974	18	4.707891e-4	1.385318e-4
256×256	4.0000	24	5.628050e-5	1.061957e-5
512×512	6.9644	32	4.670625e-5	4.257857e-5
1024×1024	12.125	46	4.203750e-5	3.942691e-5
2048×2048	21.112	66	3.922412e-5	3.755659e-5
4096×4096	36.758	100	3.764344e-5	3.643574e-5

Table 3.26: Behavior of the schemes for various k — manifestation of the pollution effect.

(see discussion in one dimensional example in Chapter 2 and also Algorithm 11). This is useful in many practical problems, therefore information about complexity in solving a scattering problem with multiple incident angles is presented.

Our implementation was written in MATLAB, and the linear systems obtained from our scheme are solved via MATLAB's built-in direct sparse solver. The computations were performed on a 2.93 GHz Quad-Core Intel Xeon with 32 Gb of RAM running on Mac OS X.

In Table 3.27 we present sound-soft scattering of a plane wave about an ellipse with an aspect ratio of 2 for the wavenumber $k_0 = 20$. The dimension of the basis (2.38) is $M = 43$. We first solve for an incidence angle of 0° and then use the obtained information to solve the same problem with an impinging wave at a different incident angle of 5°. Column 4 shows that the computational complexity of the method is somewhat better than linear as the grid is refined. This behavior is caused by the direct solver used which was developed in [8]. Column 7 shows the linear behavior of the computational complexity of the calculation of the second impinging wave. The matrices $\boldsymbol{Q}$ (2.64) computed for the first impinging wave don't need to be

recalculated, and therefore the reduced time at this stage is due to the calculation of the coefficients and obtaining the final solution by solving another auxiliary problem one more time using the solver from [8], see Section 2.3.6. Column 8 shows the time saved when a second problem is solved relative to the first one. Similar savings apply for any number of different incident waves. A sound-hard scattering with the same setting is presented in Table 3.28. We find a similar linear behavior and a similar saving of time for the second problem.

Grid	1 wave $\theta_{(\text{inc})} = 0°$			2 wave $\theta_{(\text{inc})} = 5°$			Saving
	$\|\|u^h - u^{2h}\|\|_\infty$	Time(s)	Scaling	$\|\|u^h - u^{2h}\|\|_\infty$	Time(s)	Scaling	
64×64	1.354291e+1	6.2004e-1	—	1.110603e+1	8.7971e-2	—	7.05
128×128	1.234442e-1	1.4990	2.4176	1.317353e-1	1.9846e-1	2.2560	7.55
256×256	6.971178e-3	4.7169	3.1466	7.434611e-3	4.0498e-1	2.0405	11.65
512×512	4.245374e-4	1.7626e+1	3.7368	4.521149e-4	1.1563	2.8553	15.24
1024×1024	2.635393e-5	6.6883e+1	3.7944	2.805860e-5	3.9594	3.4240	16.89
2048×2048	1.644256e-6	2.6894e+2	4.0211	1.750468e-6	1.6856e+1	4.2571	15.96
4096×4096	1.027215e-7	1.4513e+3	5.3963	1.093551e-7	8.7533e+1	5.1929	16.58

Table 3.27: CPU times for sound-soft scattering of a plane wave with incidence angles 0° and 5° about an ellipse with aspect ratio 2 for wavenumber $k_0 = 20$. The dimension of the basis $M = 43$.

Grid	1 wave $\theta_{(\text{inc})} = 0°$			2 wave $\theta_{(\text{inc})} = 5°$			Saving
	$\|\|u^h - u^{2h}\|\|_\infty$	Time(s)	Scaling	$\|\|u^h - u^{2h}\|\|_\infty$	Time(s)	Scaling	
64×64	6.366639	6.1528e-1	—	5.899738	1.3213e-1	—	4.66
128×128	5.268134 e-1	1.4878	2.4180	1.096330	2.0253e-1	1.5328	7.35
256×256	7.056579e-3	4.7161	3.1700	7.205329e-3	4.0841e-1	2.0166	11.55
512×512	4.305407e-4	1.7395e+1	3.6884	4.414049e-4	1.1562	2.8309	15.05
1024×1024	2.680923e-5	6.6856e+1	3.8434	2.748845e-5	3.9751	3.4381	16.82
2048×2048	1.673873e-6	2.6953e+2	4.0315	1.715142e-6	1.6876e+1	4.2455	15.97
4096×4096	1.046800e-7	1.4521e+3	5.3875	1.071411e-7	8.7569e+1	5.1888	16.58

Table 3.28: CPU times for hard-soft scattering of a plane wave with incidence angles 0° and 5° about an ellipse with aspect ratio 2 for wavenumber $k_0 = 20$. The dimension of the basis $M = 43$.

3.3 Transmission–Reflection problems

3.3.1 Piecewise constant coefficients

The numerical simulation of the simultaneous transmission and scattering of waves off a given shape (an ellipse) is done using a computational framework similar to that of Section 3.2, except that instead of setting a boundary condition on Γ we assume that the medium inside the ellipse is characterized by a constant wavenumber k_1 (typically, $k_1 > k_0$). At the interface Γ the overall solution and its first normal derivative are continuous.

The exterior AP and its discretization remain the same as in Section 3.2, while the interior AP is formulated on the rectangle $[-a-0.2, a+0.2] \times [-b-0.2, b+0.2]$, where a and b are the major and minor semi-axes of the ellipse, respectively. We keep $a = 1.8$ and vary b between 0.9 and 0.15, which yields aspect ratios between 2 and 12. The boundary conditions for the interior AP are zero Dirichlet at the two horizontal sides of the rectangle, and local Sommerfeld-type conditions (complex) at its two vertical sides (see (2.34)). The latter guarantees the unique solvability of the interior AP (no resonances), see [9, Section 4.2] or [42, Section 5.2]. The interior AP is discretized by the compact scheme [9] with fourth order accuracy on a uniform, in each coordinate direction, Cartesian grid. It is then solved by a sparse direct linear solver built into MATLAB. To simplify the monitoring and analysis of the grid convergence, the grid dimensions for the interior and exterior AP are always kept the same, i.e., those two grids are refined synchronously. As in Section 3.2, the convergence is assessed by evaluating the maximum volume norm of the difference between the numerical solutions obtained on two consecutive grids. In this section

though, it is done independently for the exterior and interior parts of the overall solution.

Grid	Exterior					
	$k_0 = 1, k_1 = 3, M = 18$		$k_0 = 5, k_1 = 15, M = 43$		$k_0 = 10, k_0 = 30, M = 70$	
	$\|\|u^h - u^{2h}\|\|_\infty$	rate	$\|\|u^h - u^{2h}\|\|_\infty$	rate	$\|\|u^h - u^{2h}\|\|_\infty$	rate
64×64	4.595301e-3	—	3.193901	—	6.548224e+2	—
128×128	1.680380e-4	4.7733	3.294341e-1	3.2773	1.939342	8.3994
256×256	9.570738e-6	4.1340	1.892338e-3	7.4437	1.929997e-1	3.3289
512×512	4.988526e-7	4.2619	1.133776e-4	4.0610	6.944723e-3	4.7965
1024×1024	2.966397e-8	4.0718	6.982484e-6	4.0213	4.325129e-4	4.0051
2048×2048	1.713626e-9	4.1136	4.349789e-7	4.0047	2.695934e-5	4.0039
	Interior					
	$\|\|u^h - u^{2h}\|\|_\infty$	rate	$\|\|u^h - u^{2h}\|\|_\infty$	rate	$\|\|u^h - u^{2h}\|\|_\infty$	rate
64×64	1.580527e-2	—	8.622188	—	7.361263e+2	—
128×128	1.371018e-4	6.8490	4.000175e-1	4.4299	4.175908	7.4617
256×256	8.490845e-6	4.0132	2.746052e-3	7.1866	2.013473e-1	4.3743
512×512	4.202829e-7	4.3365	1.663763e-4	4.0448	8.816271e-3	4.5134
1024×1024	2.442490e-8	4.1049	1.028977e-5	4.0152	5.509656e-4	4.0001
2048×2048	1.366547e-9	4.1597	6.430838e-7	4.0001	3.435270e-5	4.0035

Table 3.29: Transmission and scattering of a plane wave with incidence angle 40° about an ellipse with aspect ratio 2.

The data Tables 3.29, 3.30 and 3.31 demonstrate the grid convergence for two particular sets of parameters involved. The convergence for other cases that we have tried with piecewise constant k looks similar. In addition to showing the convergence data in Tables 3.29, 3.30 and 3.31, we also plot an absolute value and real and imaginary parts of the solutions that we have computed, see Figures 3.10 through 3.15.

Grid	Exterior					
	$k_0 = 1, k_1 = 3, M = 18$		$k_0 = 5, k_1 = 15, M = 43$		$k_0 = 10, k_0 = 30, M = 70$	
	$\|\|u^h - u^{2h}\|\|_\infty$	rate	$\|\|u^h - u^{2h}\|\|_\infty$	rate	$\|\|u^h - u^{2h}\|\|_\infty$	rate
64×64	3.397953e-2	—	1.928982	—	1.564833e+4	—
128×128	5.257675e-4	6.0141	1.222531	0.6580	2.540071	12.5889
256×256	2.968034e-5	4.1468	1.256795e-2	6.6040	2.505713	0.0196
512×512	1.621693e-6	4.1939	7.215245e-4	4.1226	5.294069e-2	5.5647
1024×1024	8.319173e-8	4.2849	4.686281e-5	3.9445	3.040675e-3	4.1219
2048×2048	5.185747e-9	4.0038	2.980399e-6	3.9749	1.824703e-4	4.0587
	Interior					
	$\|\|u^h - u^{2h}\|\|_\infty$	rate	$\|\|u^h - u^{2h}\|\|_\infty$	rate	$\|\|u^h - u^{2h}\|\|_\infty$	rate
64×64	5.915841e-2	—	4.502945	—	2.997456e+4	—
128×128	4.727249e-4	6.9674	1.476710	1.6085	1.454990e+1	11.0085
256×256	9.910096e-6	5.5760	7.240317e-2	4.3502	3.219025	2.1763
512×512	8.298524e-7	3.5780	7.604703e-4	6.5730	5.533717e-2	5.8622
1024×1024	3.405935e-8	4.6067	5.105078e-5	3.8969	3.352915e-3	4.0448
2048×2048	2.025545e-9	4.0717	3.330358e-6	3.9382	2.093157e-4	4.0017

Table 3.30: Transmission and scattering of a plane wave with incidence angle 40° about an ellipse with aspect ratio 3.

Grid	Exterior					
	$k_0 = 1, k_1 = 3, M = 17$		$k_0 = 5, k_1 = 15, M = 42$		$k_0 = 10, k_0 = 30, M = 68$	
	$\|\|u^h - u^{2h}\|\|_\infty$	rate	$\|\|u^h - u^{2h}\|\|_\infty$	rate	$\|\|u^h - u^{2h}\|\|_\infty$	rate
128×128	3.339419	—	1.011317e+2	—	8.966609e+2	—
256×256	2.525248e-3	10.3690	4.429088	4.5131	1.265494e+1	6.1468
512×512	3.016655e-4	3.0654	3.727909e-2	6.8925	5.603543e-1	4.4972
1024×1024	7.296313e-5	2.0477	4.070004e-3	3.1953	6.315946e-3	6.4712
2048×2048	9.046537e-6	3.0117	3.237602e-4	3.6520	3.668013e-4	4.1059
	Interior					
	$\|\|u^h - u^{2h}\|\|_\infty$	rate	$\|\|u^h - u^{2h}\|\|_\infty$	rate	$\|\|u^h - u^{2h}\|\|_\infty$	rate
128×128	2.895946	—	7.446942e+2	—	4.085428e+4	—
256×256	2.649119e-3	10.0943	4.907694	7.2455	1.662587e+2	7.9409
512×512	2.590272e-4	3.3543	4.386424e-2	6.8059	1.008079	7.3657
1024×1024	5.793892e-5	2.1605	3.933254e-3	3.4792	8.501939e-3	6.8896
2048×2048	6.983459e-6	3.0525	3.009321e-4	3.7082	3.740583e-4	4.5065

Table 3.31: Transmission and scattering of a plane wave with incidence angle 40° about an ellipse with aspect ratio 12.

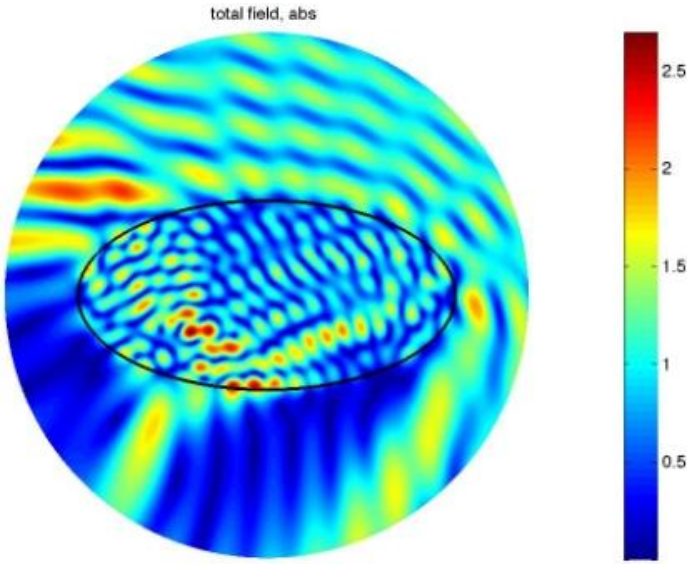

(a) Aspect ratio 2

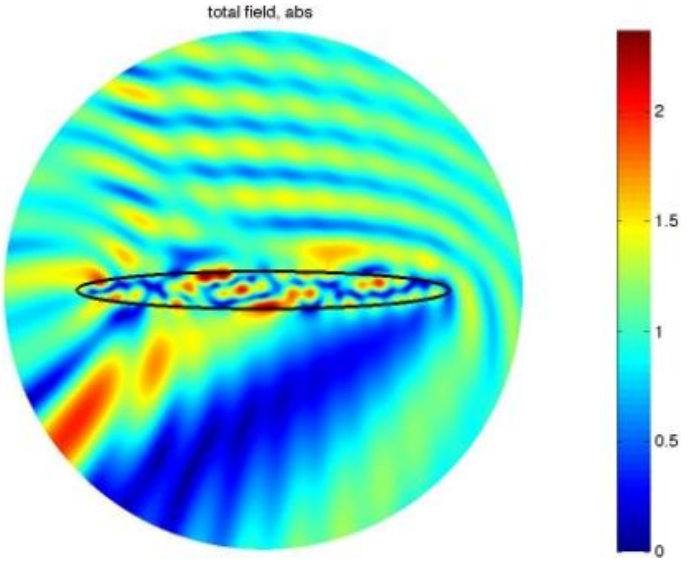

(b) Aspect ratio 10

Figure 3.10: Transmission and scattering of a plane wave with incidence angle 40° about an ellipse with $k_1 = 20$ (inside) and $k_0 = 10$ (outside). Absolute value of the total field is shown. The grid dimension is 1024×1024 for both the interior AP (Cartesian) and exterior AP (polar).

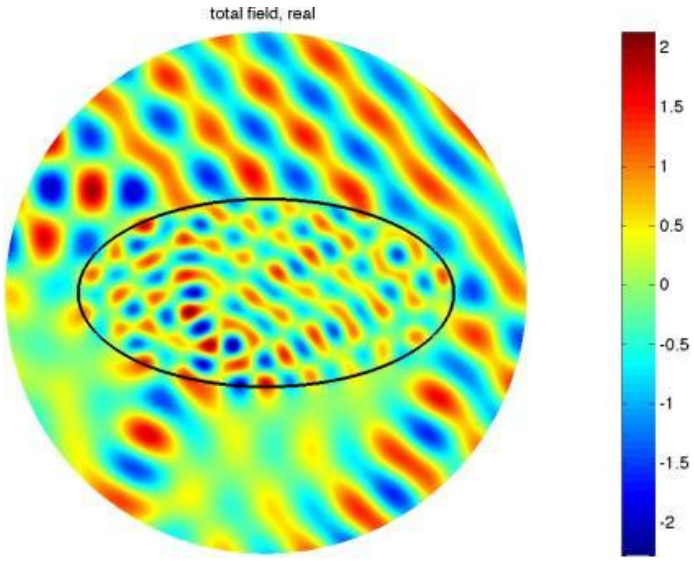

(a) Aspect ratio 2

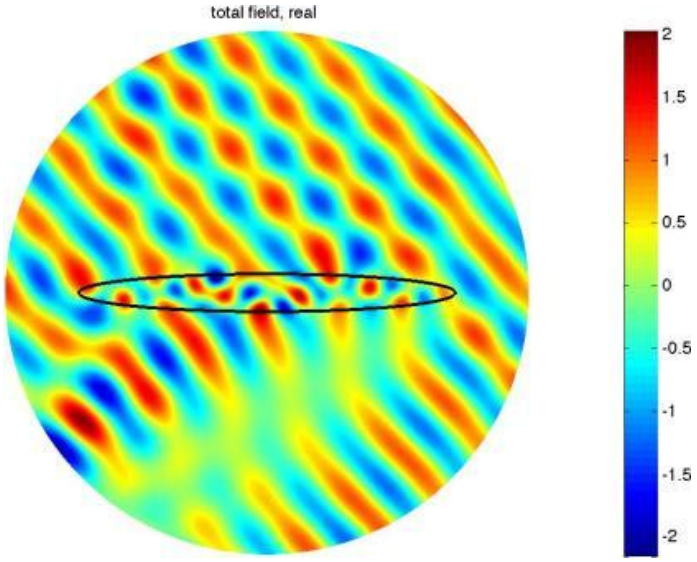

(b) Aspect ratio 10

Figure 3.11: Transmission and scattering of a plane wave with incidence angle 40° about an ellipse with $k_1 = 20$ (inside) and $k_0 = 10$ (outside). Absolute value of the total field is shown. The grid dimension is 1024×1024 for both the interior AP (Cartesian) and exterior AP (polar).

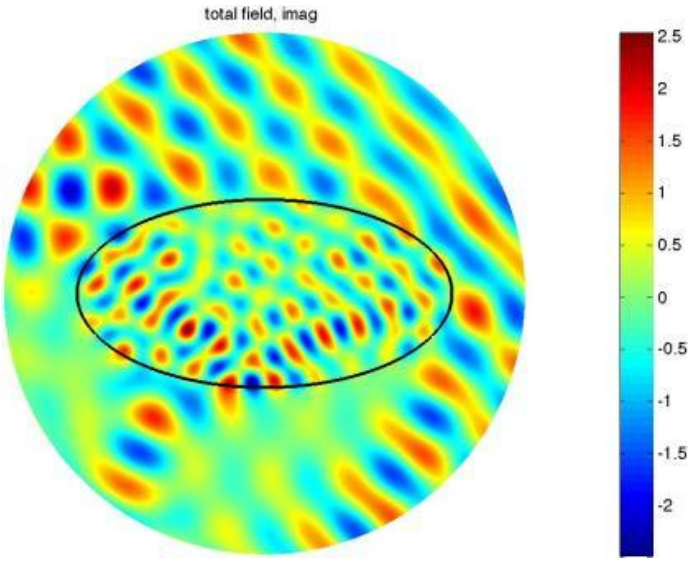

(a) Aspect ratio 2

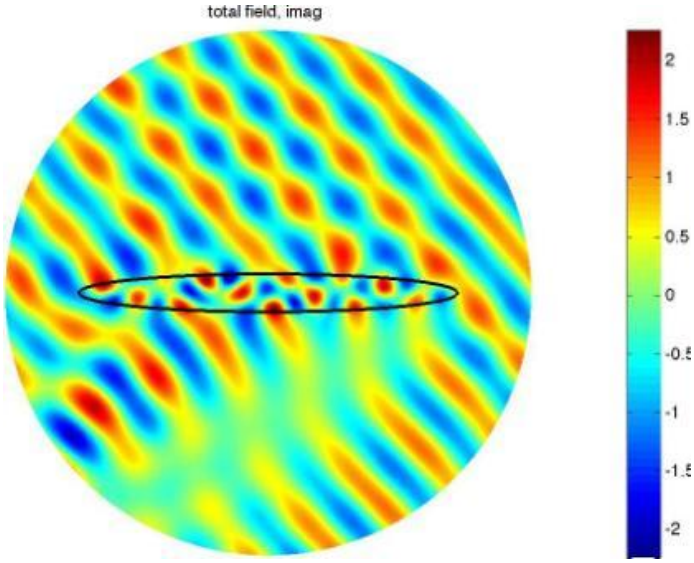

(b) Aspect ratio 10

Figure 3.12: Transmission and scattering of a plane wave with incidence angle 40° about an ellipse with $k_1 = 20$ (inside) and $k_0 = 10$ (outside). Absolute value of the total field is shown. The grid dimension is 1024×1024 for both the interior AP (Cartesian) and exterior AP (polar).

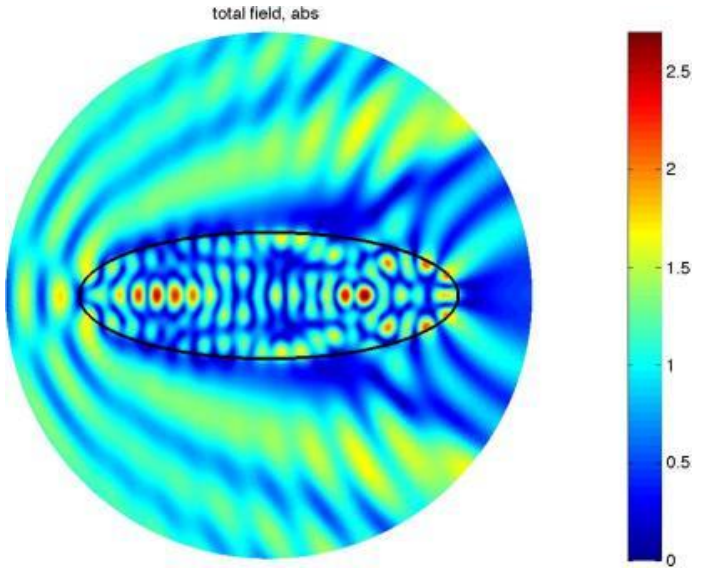

(a) Aspect ratio 3

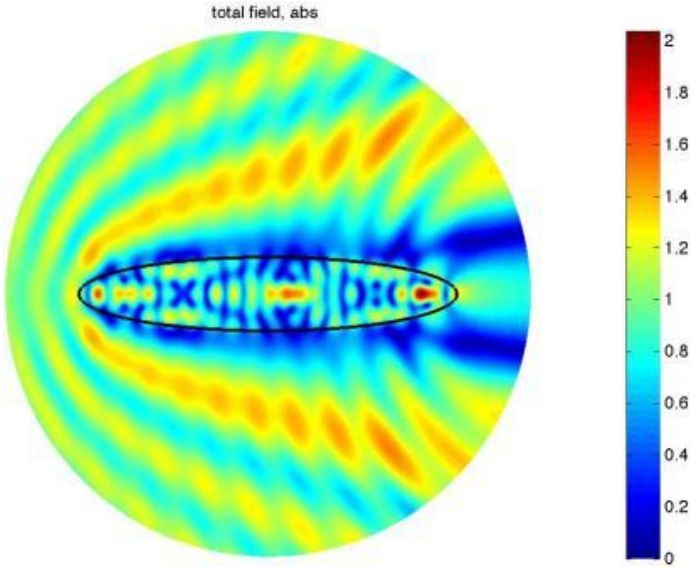

(b) Aspect ratio 5

Figure 3.13: Transmission and scattering of a plane wave with incidence angle 180° about an ellipse with $k_1 = 20$ (inside) and $k_0 = 10$ (outside). Absolute value of the total field is shown. The grid dimension is 513×513 for both the interior AP (Cartesian) and exterior AP (polar).

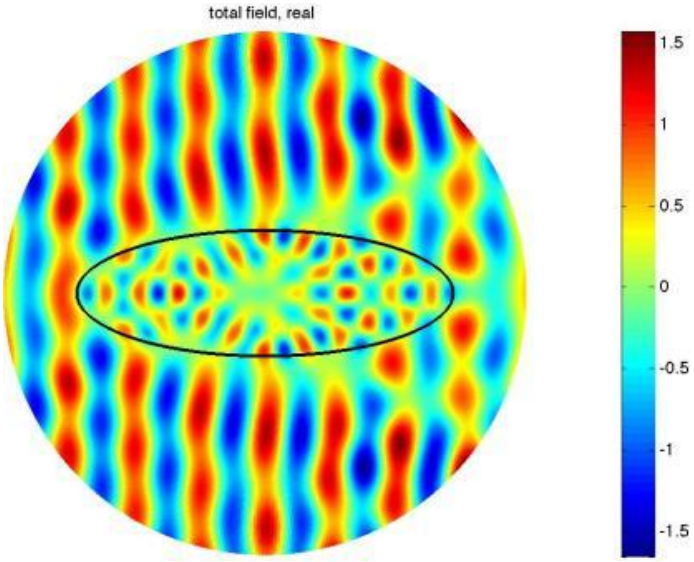

(a) Aspect ratio 3

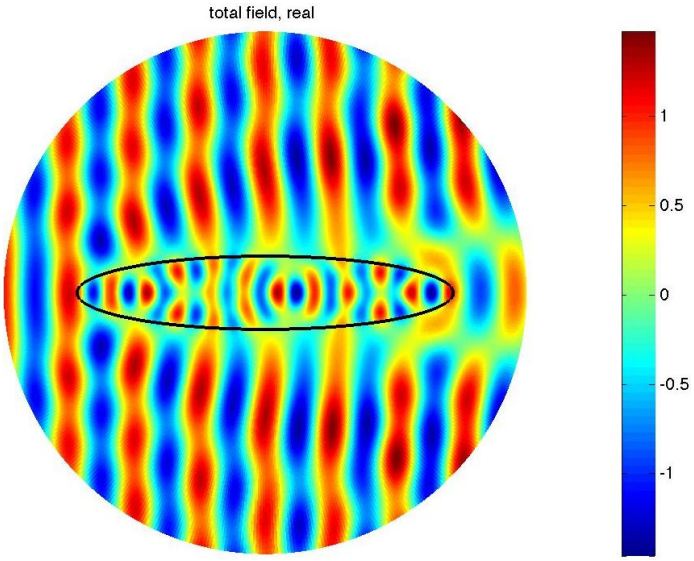

(b) Aspect ratio 5

Figure 3.14: Transmission and scattering of a plane wave with incidence angle 180° about an ellipse with $k_1 = 20$ (inside) and $k_0 = 10$ (outside). Absolute value of the total field is shown. The grid dimension is 513×513 for both the interior AP (Cartesian) and exterior AP (polar).

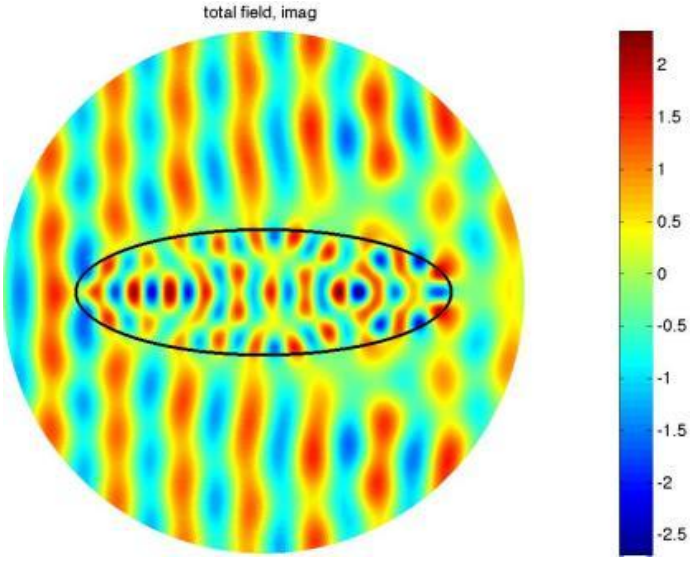

(a) Aspect ratio 3

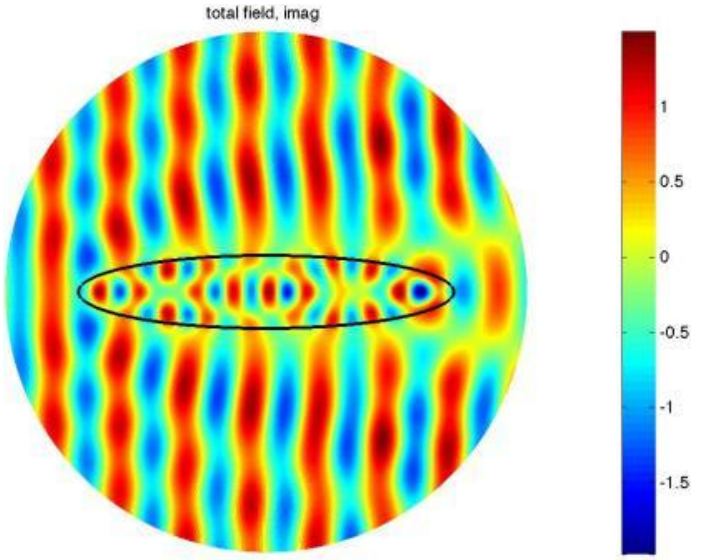

(b) Aspect ratio 5

Figure 3.15: Transmission and scattering of a plane wave with incidence angle 180° about an ellipse with $k_1 = 20$ (inside) and $k_0 = 10$ (outside). Absolute value of the total field is shown. The grid dimension is 513×513 for both the interior AP (Cartesian) and exterior AP (polar).

3.3.2 Piecewise smooth coefficients

In this section, we keep the computational setting the same as in Section 3.3.1, except that we allow for a smooth variation of the wavenumber inside the ellipse:

$$k = \begin{cases} k_1 e^{-10(r-r_0)^6 r^6}, & \text{if } r \leqslant r_0, \\ k_1, & \text{if } r > r_0, \end{cases} \tag{3.8}$$

where $r = \sqrt{x^2+y^2}$ and $r_0 = 1.6$. The variable coefficient Helmholtz equation is approximated with fourth order accuracy by the compact scheme of [9]. In Table 3.32, we show the results for the ellipse with aspect ratio 2: $a = 1.8$ and $b = 0.9$. In Table 3.33, we show the results for the ellipse with aspect ratio 3: $a = 1.8$ and $b = 0.6$. In Table 3.34, we show the results for the ellipse with aspect ratio 5: $a = 1.8$ and $b = 0.36$. These results corroborate the design fourth order convergence rate of the algorithm in the case of variable coefficients.

Grid	Exterior					
	$k_0 = 1, k_1 = 3, M = 50$		$k_0 = 5, k_1 = 15, M = 50$		$k_0 = 10, k_0 = 30, M = 69$	
	$\|\|\mathrm{u}^h - \mathrm{u}^{2h}\|\|_\infty$	rate	$\|\|\mathrm{u}^h - \mathrm{u}^{2h}\|\|_\infty$	rate	$\|\|\mathrm{u}^h - \mathrm{u}^{2h}\|\|_\infty$	rate
128×128	1.196903e-1	—	2.740357	—	9.679627	—
256×256	8.888395e-4	7.0732	1.071586e-1	4.6765	8.093132e-1	3.5802
512×512	5.054118e-5	4.1364	1.339804e-3	6.3216	8.933817e-3	6.5013
1024×1024	9.918967e-7	5.6711	4.031620e-5	5.0545	5.392737e-4	4.0502
2048×2048	7.239554e-8	3.7762	2.729896e-6	3.8844	4.167435e-5	3.6938
	Interior					
	$\|\|\mathrm{u}^h - \mathrm{u}^{2h}\|\|_\infty$	rate	$\|\|\mathrm{u}^h - \mathrm{u}^{2h}\|\|_\infty$	rate	$\|\|\mathrm{u}^h - \mathrm{u}^{2h}\|\|_\infty$	rate
128×128	2.169952e-1	—	5.413927	—	2.473694e+1	—
256×256	1.267208e-3	7.4199	1.422706e-1	5.2500	1.466237	4.0765
512×512	4.573756e-5	4.7921	1.506757e-3	6.5610	5.642709e-2	4.6996
1024×1024	6.765407e-7	6.0791	2.968551e-5	5.6655	4.756129e-4	6.8905
2048×2048	5.114153e-8	3.7256	2.285437e-6	3.6992	2.445819e-5	4.2814

Table 3.32: Transmission and scattering of a plane wave with incidence angle 40° about an inhomogeneous ellipse with aspect ratio 2 and interior wavenumber given by formula (3.8).

Grid	Exterior					
	$k_0 = 1, k_1 = 3, M = 44$		$k_0 = 5, k_1 = 15, M = 43$		$k_0 = 10, k_0 = 30, M = 70$	
	$\|\|u^h - u^{2h}\|\|_\infty$	rate	$\|\|u^h - u^{2h}\|\|_\infty$	rate	$\|\|u^h - u^{2h}\|\|_\infty$	rate
128×128	1.342633e-3	—	3.189426e-1	—	2.273503	—
256×256	4.704559e-5	4.8349	2.112324e-3	7.2383	1.428778	0.6701
512×512	1.972406e-6	4.5760	1.037815e-4	4.3472	8.515279e-3	7.3905
1024×1024	1.128138e-7	4.1279	6.701632e-6	3.9529	4.664540e-4	4.1902
2048×2048	6.620319e-9	4.0909	5.703865e-7	3.5545	2.867676e-5	4.0238
	Interior					
	$\|\|u^h - u^{2h}\|\|_\infty$	rate	$\|\|u^h - u^{2h}\|\|_\infty$	rate	$\|\|u^h - u^{2h}\|\|_\infty$	rate
128×128	3.067343e-3	—	1.043931	—	9.253122	—
256×256	6.693782e-5	5.5180	3.225823e-2	5.0162	2.960923	1.6439
512×512	1.396376e-6	5.5831	1.002967e-4	8.3292	4.859728e-2	5.9290
1024×1024	8.178574e-8	4.0937	6.580268e-6	3.9300	4.749737e-4	6.6769
2048×2048	5.333208e-9	3.9388	4.146442e-7	3.9882	2.935093e-5	4.0164

Table 3.33: Transmission and scattering of a plane wave with incidence angle 40° about an inhomogeneous ellipse with aspect ratio 3 and interior wavenumber given by formula (3.8).

Grid	Exterior					
	$k_0 = 1, k_1 = 3, M = 50$		$k_0 = 5, k_1 = 15, M = 50$		$k_0 = 10, k_0 = 30, M = 69$	
	$\|\|u^h - u^{2h}\|\|_\infty$	rate	$\|\|u^h - u^{2h}\|\|_\infty$	rate	$\|\|u^h - u^{2h}\|\|_\infty$	rate
128×128	1.196903e-1	—	2.740357	—	9.679627	—
256×256	8.888395e-4	7.0732	1.071586e-1	4.6765	8.093132e-1	3.5802
512×512	5.054118e-5	4.1364	1.339804e-3	6.3216	8.933817e-3	6.5013
1024×1024	9.918967e-7	5.6711	4.031620e-5	5.0545	5.392737e-4	4.0502
2048×2048	7.239554e-8	3.7762	2.729896e-6	3.8844	4.167435e-5	3.6938
	Interior					
	$\|\|u^h - u^{2h}\|\|_\infty$	rate	$\|\|u^h - u^{2h}\|\|_\infty$	rate	$\|\|u^h - u^{2h}\|\|_\infty$	rate
128×128	2.169952e-1	—	5.413927	—	2.473694e+1	—
256×256	1.267208e-3	7.4199	1.422706e-1	5.2500	1.466237	4.0765
512×512	4.573756e-5	4.7921	1.506757e-3	6.5610	5.642709e-2	4.6996
1024×1024	6.765407e-7	6.0791	2.968551e-5	5.6655	4.756129e-4	6.8905
2048×2048	5.114153e-8	3.7256	2.285437e-6	3.6992	2.445819e-5	4.2814

Table 3.34: Transmission and scattering of a plane wave with incidence angle 40° about an inhomogeneous ellipse with aspect ratio 5 and interior wavenumber given by formula (3.8).

Chapter 4

Discussion and Conclusion

4.1 Discussion

We have described a combined implementation of the method of difference potentials along with the compact high order accurate finite difference schemes for the numerical solution of wave propagation problems in the frequency domain. The governing Helmholtz equation is approximated on a regular structured grid, which is efficient and entails a low computational complexity. At the same time, the method guarantees no loss of accuracy for curvilinear non-conforming boundaries, and can also handle variable coefficients that describe a non-homogeneous medium. As such, the resulting method provides a viable alternative to both BEM and high order FEM.

The performance of the method and, in particular, its design high order accuracy, has been corroborated numerically by solving a variety of 2D interior, exterior,

and reflection/transmission Helmholtz problems, including those with variable coefficients, on Cartesian and Polar grids for non-conforming boundaries/interfaces shaped as circles and ellipses.

Among other advantages of the proposed methodology is its capability to accurately reconstruct the solution and/or its normal derivative directly at the boundary. This is done without interpolating and/or using one-sided differences, such as in conventional FD, and with no additional developments needed as in FEM, see, e.g., [11]. Additional advantages of the method are the absence of any singular integrals or similar constructs, the minimum number of unknowns that characterize the discrete solution — just one per grid node, and the same number of boundary conditions needed for the scheme as that needed for the underlying differential equation.

For exterior problems we constructed auxiliary problems (see Section 2.3.2.2) with the appropriate artificial boundary conditions (ABCs), see [64]. For the constant coefficient 2D Helmholtz equation (typical for the far field), the APs were formulated using polar coordinates, which enables a natural and efficient implementation of the exact non-local ABCs in Fourier space. The proposed methodology is extended for the combined reflection/transmission problems. The latter formulation involves a joint solution of the interior and exterior Calderon's BEPs constructed at the interface between the interior and exterior sub-regions.

Thus far, we have computed solutions only for circular and elliptical boundaries. The case of general smooth boundaries was analyzed theoretically in [42, Appendix A], and the corresponding Taylor-based extension operators have been developed.

4.2 Conclusions and future research

We have simulated a broad range of constant and variable coefficient 2D test cases for non-conforming boundaries/interfaces on regular structured grids. Our computations convincingly corroborate the design high order accuracy of the proposed method.

A study is needed to explore alternative strategies for choosing M – the dimension of the basis used for representing the solution at the boundary Γ as in (2.38) or (2.59). In addition to that, the possibility of using other bases has to be examined. The ideas of reduced order modeling [26] (or, similarly, principal component analysis or proper orthogonal decomposition) has to be investigated to further reduce the dimension of the basis on Γ. Other bases may be more convenient to use like in the case of piece-wise parametrization [10].

Actual computations of the scattering and transmission/scattering solutions for arbitrarily shaped domains (other than circles or ellipses) will need to be performed. The corresponding general construct of the equation based extension has been developed in [42, Appendix A].

The domains of a more general shape (beyond circles and ellipses) have to be developed. Arbitrary smooth boundaries will require a more general construction of the extension operators (see Appendix in [42]).

Yet another direction for future work will be to allow for multiple sub-regions, for example, multiple scatterers immersed into the same background medium. The simplest case will amount to considering a piece-wise constant function $k^2(x, y)$ in

the Helmholtz equation (1.1), while more elaborate settings may also include the variation of material characteristics.

The proposed methodology needs to be extended to 3D wave propagation which requires that the coordinates associated with a curve be replaced with surface-oriented coordinates, see [32].

Finally, the extension of the proposed methodology to time-dependent problems (e.g., the wave, i.e., d'Alembert, equation instead of the Helmholtz equation) requires additional theoretical developments.

Note, that even though the current implementation and discussion focuses on wave propagation problems, the method of difference potentials is capable of addressing a considerably broader range of formulations, including problems in heat transfer, elasticity, fluid dynamics, and other areas, see for example [52].

Bibliography

[1] S. Abarbanel and A. Ditkowski. Asymptotically stable fourth-order accurate schemes for the diffusion equation on complex shapes. *J. Comput. Phys.*, 133(2):279–288, 1997.

[2] I. M. Babuska and S.A. Sauter. Is the pollution effect of the FEM avoidable for the Helmholtz equation considering high wave numbers? *SIAM Journal on Numerical Analysis*, 34(6):2392–2423, 1997.

[3] G. Baruch, G. Fibich, and S. Tsynkov. High-order numerical method for the nonlinear Helmholtz equation with material discontinuities in one space dimension. *J. Comput. Phys.*, 227:820–850, 2007.

[4] G. Baruch, G. Fibich, S. Tsynkov, and E. Turkel. Fourth order scheme for wave-like equations in frequency space with discontinuities in the coefficients. *Communications in Computational Physics*, 5(2–4):442–455, 2009.

[5] A. Bayliss, C. I. Goldstein, and E. Turkel. On accuracy conditions for the numerical computation of waves. *J. Comput. Phys.*, 59(3):396–404, 1985.

[6] J. J. Bowman, T. B. A. Senior, and P. L. E. Uslenghi, editors. *Electromag-*

netic and Acoustic Scattering by Simple Shapes. A Summa Book. Hemisphere Publishing Corp., New York, 1987. Revised reprint of the 1969 edition.

[7] S. C. Brenner and L. Ridgway Scott. *The Mathematical Theory of Finite Element Methods*, volume 15 of *Texts in Applied Mathematics*. Springer-Verlag, New York, second edition, 2002.

[8] S. Britt, S. Tsynkov, and E. Turkel. A compact fourth order scheme for the Helmholtz equation in polar coordinates. *J. Sci. Comput.*, 45(1-3):26–47, 2010.

[9] S. Britt, S. Tsynkov, and E. Turkel. Numerical simulation of time-harmonic waves in inhomogeneous media using compact high order schemes. *Commun. Comput. Phys.*, 9(3):520–541, March 2011.

[10] S. Britt, S. Tsynkov, and E. Turkel. A high order numerical method for the Helmholtz equation with non-standard boundary conditions. *SIAM Journal on Scientific Computing*, 2012. [Submitted for publication].

[11] G. F. Carey, S.-S. Chow, and M. K. Seager. Approximate boundary-flux calculations. *Comput. Methods Appl. Mech. Engrg.*, 50(2):107–120, 1985.

[12] H. Cheng, L. Greengard, and V. Rokhlin. A fast adaptive multipole algorithm in three dimensions. *J. Comput. Phys.*, 155(2):468–498, 1999.

[13] P. G. Ciarlet. *The Finite Element Method for Elliptic Problems*, volume 40 of *Classics in Applied Mathematics*. Society for Industrial and Applied Mathematics (SIAM), Philadelphia, PA, 2002. Reprint of the 1978 original [North-Holland, Amsterdam; MR0520174 (58 #25001)].

[14] L. Collatz. *The Numerical Treatment of Differential Equations.* New York: Springer, 1966.

[15] S. Conte and C. de Boor. *Elementary Numerical Analysis: An Algorithmic Approach.* McGraw-Hill, New York, third edition, 1980.

[16] R. K. Crockett, P. Colella, and D. T. Graves. A Cartesian grid embedded boundary method for solving the Poisson and heat equations with discontinuous coefficients in three dimensions. *J. Comput. Phys.*, 230(7):2451–2469, 2011.

[17] A. Ditkowski and M. Sever. On the intersection of sets of incoming and outgoing waves. *Quart. Appl. Math.*, 66(1):1–26, 2008.

[18] Y. A. Erlangga. Advances in iterative methods and preconditioners for the Helmholtz equation. *Arch. Comput. Methods Eng.*, 15(1):37–66, 2008.

[19] Y. A. Erlangga, C. W. Oosterlee, and C. Vuik. A novel multigrid based preconditioner for heterogeneous Helmholtz problems. *SIAM J. Sci. Comput.*, 27(4):1471–1492 (electronic), 2006.

[20] Y. A. Erlangga and E. Turkel. Iterative schemes for high order compact discretizations to the exterior Helmholtz equation. *Mathematical Modeling and Numerical Analysis (ESAIM: M2AN)*, 2011. [To appear].

[21] Y. A. Erlangga, C. Vuik, and C. W. Oosterlee. On a class of preconditioners for solving the Helmholtz equation. *Appl. Numer. Math.*, 50(3-4):409–425, 2004.

[22] C. Farhat, I. Harari, and L.P. Franca. The discontinuous enrichment method. *Computer Meth. in Appl. Mech. & Eng.*, 190:6455–6479, 2001.

[23] C. Farhat, R. Tezaur, and J. Toivanen. A domain decomposition method for discontinuous Galerkin discretizations of Helmholtz problems with plane waves and Lagrange multipliers. *International Journal for Numerical Methods in Engineering*, 78:1513–1531, 2009.

[24] W. Fong and E. Darve. The black-box fast multipole method. *J. Comput. Phys.*, 228(23):8712–8725, 2009.

[25] L. Greengard and V. Rokhlin. A fast algorithm for particle simulations. *J. Comput. Phys.*, 73(2):325–348, 1987.

[26] M. Gunzburger and J. Peterson. Reduced-order modeling of complex systems with multiple system parameters. In *Large-scale scientific computing*, volume 3743 of *Lecture Notes in Comput. Sci.*, pages 15–27. Springer, Berlin, 2006.

[27] B. Gustafsson. The convergence rate for difference approximations to general mixed initial-boundary value problems. *SIAM Journal on Numerical Analysis*, 18(2):179–190, 1981.

[28] Bertil Gustafsson. The convergence rate for difference approximations to mixed initial boundary value problems. *Mathematics of Computation*, 29(130):396–406, 1975.

[29] T. Hagstrom. Radiation boundary conditions for the numerical simulation of waves. In A. Iserlis, editor, *Acta Numerica*, volume 8, pages 47–106, Cambridge, 1999. Cambridge University Press.

[30] William D. Henshaw. A high-order accurate parallel solver for Maxwell's equa-

tions on overlapping grids. *SIAM J. Sci. Comput.*, 28(5):1730–1765 (electronic), 2006.

[31] J. S. Hesthaven and T. Warburton. *Nodal discontinuous Galerkin methods*, volume 54 of *Texts in Applied Mathematics*. Springer, New York, 2008. Algorithms, analysis, and applications.

[32] E. H. Hirschel and W. Kordulla. *Shear Flow in Surface-Oriented Coordinates*, volume 4 of *Notes on Numerical Fluid Mechanics*. Friedr. Vieweg & Sohn Verlagsgesellschaft mbH, Braunschweig/Wiesbaden, 1981-1986.

[33] R. Hixon and E. Turkel. Compact implicit MacCormack-type schemes with high accuracy. *J. Comput. Phys.*, 158(1):51–70, 2000.

[34] R. Holland. Pitfalls of staircase meshing. *IEEE Trans. Electromagnetic Compatibility*, 35:434–439, 1993.

[35] F. Ihlenburg. *Finite Element Analysis of Acoustic Scattering*, volume 132 of *Applied Mathematical Sciences*. Springer, 1998.

[36] H. Johansen and P. Colella. A Cartesian grid embedded boundary method for Poisson's equation on irregular domains. *J. Comput. Phys.*, 147(1):60–85, 1998.

[37] R. J. LeVeque and Z. Li. The immersed interface method for elliptic equations with discontinuous coefficients and singular sources. *SIAM J. Numer. Anal.*, 31(4):1019–1044, 1994.

[38] Z. Li and K. Ito. *The Immersed Interface Method*, volume 33 of *Frontiers in Applied Mathematics*. Society for Industrial and Applied Mathematics (SIAM),

Philadelphia, PA, 2006. Numerical solutions of PDEs involving interfaces and irregular domains.

[39] J. Lončarić, V. S. Ryaben'kii, and S. V. Tsynkov. Active shielding and control of noise. *SIAM J. Applied Math.*, 62(2):563–596, 2001.

[40] P. G. Martinsson. *Fast multiscale methods for lattice equations.* PhD thesis, Texas Institute for Computational and Applied Mathematics, The University of Texas at Austin, Austin, TX, USA, 2002.

[41] M. Medvinsky. Comparison of local absorbing radiation conditions for scattering about elliptical body. Master's thesis, Tel Aviv University, 2007.

[42] M. Medvinsky, S. Tsynkov, and E. Turkel. The method of difference potentials for the Helmholtz equation using compact high order schemes. *J. Sci. Comput.*, 53(1):150–193, 2012.

[43] M. Medvinsky and E. Turkel. On surface radiation conditions for an ellipse. *Journal of Computational and Applied Mathematics*, 234(6):1647–1655, 2010.

[44] M. Medvinsky, E. Turkel, and U. Hetmaniuk. Local absorbing boundary conditions for elliptical shaped bodies. *J. Comput. Phys.*, 227:8254–8267, 2008.

[45] C. S. Peskin. The immersed boundary method. *Acta Numer.*, 11:479–517, 2002.

[46] D. Pissoort, E. Michielssen, and A. Grbic. An electromagnetic crystal Green function multiple scattering technique for arbitrary polarizations, lattices, and defects. *J. of Lightwave Technology*, 25(2):571–583, 2007.

[47] A. A. Reznik. Approximation of surface potentials of elliptic operators by difference potentials. *Dokl. Akad. Nauk SSSR*, 263(6):1318–1321, 1982.

[48] A. A. Reznik. *Approximation of the surface potentials of elliptic operators by difference potentials and solution of boundary-value problems.* PhD thesis, Moscow Institute for Physics and Technology, Moscow, USSR, 1983. [in Russian].

[49] R. D. Richtmyer. *Difference methods for initial-value problems.* Interscience tracts in pure and applied mathematics. Tract 4. Interscience Publishers, Inc., New. York, 1957.

[50] V. S. Ryaben'kii. Boundary equations with projections. *Russian Math. Surveys*, 40(2):147–183, 1985.

[51] V. S. Ryaben'kii. Boundary equations with projections. *Russian Math. Surveys*, 40(2):147–183, 1985.

[52] V. S. Ryaben'kii. *Method of Difference Potentials and Its Applications*, volume 30 of *Springer Series in Computational Mathematics.* Springer-Verlag, Berlin, 2002.

[53] V. S. Ryaben'kii. *Method of Difference Potentials and Its Applications*, volume 30 of *Springer Series in Computational Mathematics.* Springer-Verlag, Berlin, 2002.

[54] V. S. Ryaben'kii and A. F. Filippov. *On Stability of Difference Equations.* Gosudarstv. Izdat. Tehn.-Teor. Lit., Moscow, 1956. [Russian].

[55] I. Singer and E. Turkel. High-order finite difference methods for the Helmholtz equation. *Comput. Methods Appl. Mech. Engrg.*, 163(1-4):343–358, 1998.

[56] I. Singer and E. Turkel. Sixth-order accurate finite difference schemes for the Helmholtz equation. *J. Comput. Acoust.*, 14(3):339–351, 2006.

[57] I. A. Stegun and M. Abramowitz. *Handbook of Mathematical Functions: With Formulas, Graphs, and Mathematical Tables*. National Bureau of Standards, 1968.

[58] G. Strang and G. J. Fix. *An Analysis of the Finite Element Method*. Prentice Hall, Englewood Cliffs, NJ, 1973.

[59] M. Svärd and J. Nordström. On the order of accuracy for difference approximations of initial-boundary value problems. *Journal of Computational Physics*, 218(1):333–352, 2006.

[60] K. Taira and T. Colonius. The immersed boundary method: a projection approach. *Journal of Computational Physics*, 225(2):2118–2137, 2007.

[61] H. Tal-Ezer and E. Turkel. The iterative solver Risolv with application to the exterior Helmholtz problem. *SIAM J. Sci. Comput.*, 32(1):463–475, 2010.

[62] Y.H. Tseng and J.H. Ferziger. A ghost-cell immersed boundary method for flow in complex geometry. *Journal of Computational Physics*, 192(2):593–623, 2003.

[63] I. Tsukerman. A class of difference schemes with flexible local approximation. *J. Comput. Phys.*, 211(2):659–699, 2006.

[64] S. V. Tsynkov. Numerical solution of problems on unbounded domains. A review. *Appl. Numer. Math.*, 27(4):465–532, 1998.

[65] E. Turkel, D. Gordon, R. Gordon, and S. Tsynkov. Compact 2d and 3d sixth order schemes for the helmholtz equation with variable wave number. *Journal of Computational Physics*, 2012.

[66] E. Turkel and A. Yefet. On the construction of a high order difference scheme for complex domains in a Cartesian grid. *Appl. Numer. Math.*, 33(1-4):113–124, 2000.

[67] J. C. G. Vega and S. C. Cerda. Theory and numerical analysis of the Mathieu functions. *Tecnologico de Monterrey, Mexico report and the references given in this paper*, 2003.

[68] S. Xu. A boundary condition capturing immersed interface method for 3D rigid objects in a flow. *J. Comput. Phys.*, 230(19):7176–7190, 2011.

[69] A. Yefet and E. Turkel. Fourth order compact implicit method for the Maxwell equations with discontinuous coefficients. *Appl. Numer. Math.*, 33(1-4):125–134, 2000.

[70] L. Ying, G. Biros, and D. Zorin. A kernel-independent adaptive fast multipole algorithm in two and three dimensions. *J. Comput. Phys.*, 196(2):591–626, 2004.

[71] C. Zhang and R. J. LeVeque. The immersed interface method for acoustic wave equations with discontinuous coefficients. *Wave Motion*, 25(3):237–263, 1997.

[72] X. Zhong. A new high-order immersed interface method for solving elliptic equations with imbedded interface of discontinuity. *J. Comput. Phys.*, 225(1):1066–1099, 2007.

[73] Y. C. Zhou and G. W. Wei. On the fictitious-domain and interpolation formulations of the matched interface and boundary (MIB) method. *J. Comput. Phys.*, 219(1):228–246, 2006.

[74] Y. C. Zhou, S. Zhao, M. Feig, and G. W. Wei. High order matched interface and boundary method for elliptic equations with discontinuous coefficients and singular sources. *J. Comput. Phys.*, 213(1):1–30, 2006.

תקציר

אנו חוקרים התפשטות גלים על פני אזורים גדולים של טווח חלק, אך לא בהכרח קבוע, המופרד לתת תחומים על ידי ממשקים בעלי צורה שרירותית. אנו משתמשים בשיטת הפרד ומשול המבוססת על חלוקת הגל לגלים נכנסים ויוצאים. הפתרון לבעיה מורכב מסט של פתרונות פרטיים לבעיית עזר. בעיית עזר מוגדרת באופן בלתי תלוי לכל תת תחום. הבחירה של בעיית עזר היא גמישה יחסית: ניתן לנסחה בצורה המאפשרת פתרון נומרי קל וחסכוני. השיטה החדשה שלנו משתמשת רק ברשתות נומריות פשוטות ומובנות, כגון רשתות קרטזיות ופולריות, ללא קשר לצורתם של גבולות התחום של הבעיה או צורת הממשקים. באזורים חלקים, היא משתמשת בסכמת הפרשים סופיים קומפקטית מסדר דיוק גבוהה אשר אינם דורשים תנאיי שפה נוספים מלבד אלו הנדרשים למשוואה הדיפרנציאלית עצמה. ממשקים אשר אינם יושבים על הרשת הנומרית מטופלים על ידי אופרטור של קלדרון ושיטת הפוטנציאלים ההפרשיים [74].

לאופרטור של קלדרון ולשיטת הפוטנציאלים ההפרשיים מספר יתרונות חשובים: הוא מטפל בקלות בגבולות וממשקים עקומים, מקדמים משתנים ותנאי שפה כלליים ואילו המורכבות היא זה של סכימת ההפרשים הסופיים, על רשת מובנית רגילה. היתרון העיקרי הוא שהמתודולוגיה הזו מספקת דיוק וסדר גבוה ומתגברת על הקשיים הכרוכים בגישות מסורתיות יותר.

לילדיי

ברצוני להביע את תודתי והערכתי העמוקה לפרופסור אלי טורקל על הסבלנות, המעורבות המתמדת והתמיכה הרבה במהלך מחקר זה ובמהלך שבע שנות היכרות ושיתוף פעולה.

כמו כן, אני אסיר תודה לפרופסור סמיון צנקוב על הדרכה, ייעוץ וידידות, במיוחד עבור התמחות בלתי נשכחת באוניברסיטת צפון קרוליינה. ללא העזרה והעידוד שלו עבודה זו לעולם לא הייתה נעשת.

כמובן, אני מודה למשפחתי על הסבלנות והאהבה. להוריי התומכים, אישתי המתחשבת והילדים המקסימים. בלעדיהם מחקר זה לעולם לא יכול היה להתקיים (פשוטו כמשמעו).

ברצוני להביע את תודתי לכל בני המשפחה והחברים שהיו "שם" בשבילי בתקופה ארוכה זו, אך שמם לא מופיע לעיל.

עבודה זו נעשתה בהדרכת המנחים

פרופסור אלי טורקל, אוניברסיטת תל־אביב

ופרופסור סמיון צנקוב, אוניברסיטת צפון קרוליינה

אוניברסיטת תל־אביב

הפקולטה למדעים מדויקים על שם ריימונד ובברלי סאקלר

ביה"ס למדעי המתמטיקה

החוג למתמטיקה שימושית

שיטות נומריות מסדר גבוה עבור גלים

תוך שימוש ברשתות רגילות וממשקים חורגים

חבור לשם קבלת תואר "דוקטור לפילוסופיה"

על ידי

מדבינסקי מיכאל

הוגש לסנט של אוניברסיטת תל־אביב

6 באוקטובר 2013